Orientational order on axisymmetric interfaces in solid-stabilized emulsions

Jason Klebes

School of Mathematics, University of Leeds

School of Physics and Astronomy, University of Edinburgh

Submitted in accordance with the requirements for the degree of

Doctor of Philosophy

August, 2022

Intellectual Property Statement

The candidate confirms that the work submitted is his own, except where work which has formed part of jointly authored publications has been included. The contribution of the candidate and the other authors to this work has been explicitly indicated below. The candidate confirms that appropriate credit has been given within the thesis where reference has been made to the work of others.

Parts of Chapters 2, 3, and 4 have appeared in publication as follows:

J. Klebes, P. S. Clegg, and R. M. L. Evans, Phys Rev E **105**, 064802 (2022).

The contributions of the candidate consists of choice of topic; calculations and interpretation; design, implementation, and execution of the simulation protocol; analysis and presentation of results; manuscript writing; and final editing. The co-authors are the supervisors, whose contributions are initial construction of the theoretical framework (RMLE); critical discussion of the results (RMLE & PC); and editing (RMLE & PC).

This copy has been supplied on the understanding that it is copyright material and that no quotation from the thesis may be published without proper acknowledgement.

The right of Jason Klebes to be identified as Author of this work has been asserted by him in accordance with the Copyright, Designs and Patents Act 1988.

© 2023 The University of Leeds and Jason Klebes.

Acknowledgements

First and foremost my thanks goes to my supervisors, Mike Evans, whose guidance was invaluable and whose trust kept me going through the difficult bits, and Paul Clegg, always helpful and encouraging. I thank Daniel Read and Patrick Warren for further discussion and supervision.

Credit goes to everyone who made SOFI work, and thanks especially to my Cohort 4 friends, who made it fun. Also to my PhD student colleagues, at various times, at Leeds School of Mathematics and in the JCMB. And to Andy and Charlotte, and Edinburgh friends around Stork's Beak, for weekly swordfights and late nights.

Ich danke meiner Familie, meinen Eltern, und meinen Geschwistern. Mein besonderer Dank gilt meinen Großeltern Bernhard und Roswitha Klebes, für ihre jahrelange Unterstützung und ihr andauerndes Interesse am Erfolg meines Studiums.

Lastly but most importantly my gratitude goes to my husband James. I am lucky to have you.

Abstract

In emulsions, immiscible oil and water phases are commonly separated by an interface hosting a layer of surfactant molecules, which decreases surface tension and stabilizes the system. Alternatively, in solid-stabilized or Pickering emulsions, nano- or microparticles are embedded in the interface, decreasing interfacial area. Solid-stabilized emulsions are extremely stable and allow for complex non-spherical droplet shapes.

Spherical particles embedded in an interface constitute a two-dimensional monolayer in which locally hexagonal packings can be expected. This hexatic arrangement is one type of orientational order, another is nematic order in the alignment of a layer of rod-like interfacial particles. Orientational order interacts with surface shape; hexatic or nematic packing is disrupted by Gaussian curvature. Conversely, droplet shape may adapt to accommodate orientational order. For surfactant-stabilized emulsion systems, the effects of hexatic order on droplet shape have been experimentally and theoretically investigated. I here extend the investigation to solid-stabilized emulsions.

On the example of a modulated cylindrical surface shape, I examine the theory of orientational order analytically and using a lattice-based stochastic simulation. With a generic Landau-Ginzburg model, I find that modulations in the amount of order co-occur with well-known defect phenomena. I distinguish type I and type II systems, with zero or up to $4n$ defects respectively. I deduce that there is a discrete spectrum of modulated tubule shapes.

Experiments motivate the adaptation of the generic model to the specific interfacial material of rod-like colloidal nanoparticles. I apply and adapt results from the density functional theory literature to obtain material parameters of a two-dimensional hard-rod gas. The material-specific model reveals that, in the case studied, interfacial mechanics are dominated by surface tension and orientational order conforms to the resulting surface curvature via the defect state.

Contents

List of Figures

List of Tables

CHAPTER 1

Introduction

Abstract

An overview of the solid-stabilized emulsion and related compounds is presented. Motivating observations are introduced: Hexatic order occurs in particle monolayers. However, surface curvature and topology can introduce defects or destroy order. Where interfaces are sufficiently soft, there can be complex shape-order interactions. The overarching question is to adapt the continuum description of order on soft interfaces from molecule-stabilized interfaces to solid-stabilized emulsions. Several peculiarities of solid-stabilized emulsion materials must be taken into account: non-spherical shapes, possibly differentiated phase and domain behavior, and constraints other than surface tension. The underlying approach used in this thesis - focus on a particular mesoscale and equilibrium statistical physics - is discussed with respect to the appropriateness for solid-stabilized interfaces. Finally the development of the model in this thesis is summarized.

1.1 Systems and applications

1.1.1 Solid-stabilized emulsions

An emulsion is a suspension of microscopic oil droplets in water (or vice versa). Everyday experience indicates that this is not an equilibrium configuration of the system, as a mixture of oil and water soon phase separates into distinct oil and water phases. This is due to the energetic cost of maintaining large amount of interfacial area, where water and oil are in contact at the surface of each droplet. Emulsion-based products are usually made stable on the scale of months or years by adding a surfactant. In the case of molecular surfactants, the surfactant molecules position themselves at the interfaces and decrease surface tension.

In contrast, in a Pickering emulsion, or solid-stabilized emulsion, the surfactants are nano- or microparticles (Figure 1.1.a). Because the insertion of particles reduces the area in which oil and water are in contact, this is a very effective way to stabilize an emulsion. Pickering emulsions are of interest to numerous industries, such as food, cosmetics, paint and coatings. Because particle-stabilized emulsions depend on the mechanical action of the particles, a wide range of materials can be chosen. Formulations can be created using common, low-cost, or biocompatible materials such as clay, silica, or starch in place of specialized chemical surfactants [1, 2].

Surface tension is an energy cost per unit area of interface. In conventional (surfactant-stabilized emulsions), surface tension is lowered by a layer of surfactant molecules. The basic mechanism behind the stability of solid-stabilized emulsions is that a particle of radius r embedded in the interface (Figure 1.2) occupies an area of $A = \pi(r(1 - \cos\theta))^2$ [3, 4]. Instead of oil-water interface, there is instead particle-oil and particle-water interface. The energy is lowered by $\Delta E = \gamma\pi(r(1 \pm \cos\theta))^2$ relative to the particle being suspended in the oil $(+)$ or water $(-)$ phases. The same energy is required to detach the particle. For microscale particles, the energy difference is of order $10^7 k_B T$ [5]; for a $50nm$ nanoparticle it is of order $10^4 k_B T$. Especially in the case of nanoparticles, this is clearly larger than the mean energy of a thermal fluctuation, which at room temperature have energy on the order of $k_b T$. Because of the vanishing prob-

(a) Pickering emulsion   (b) bijel.
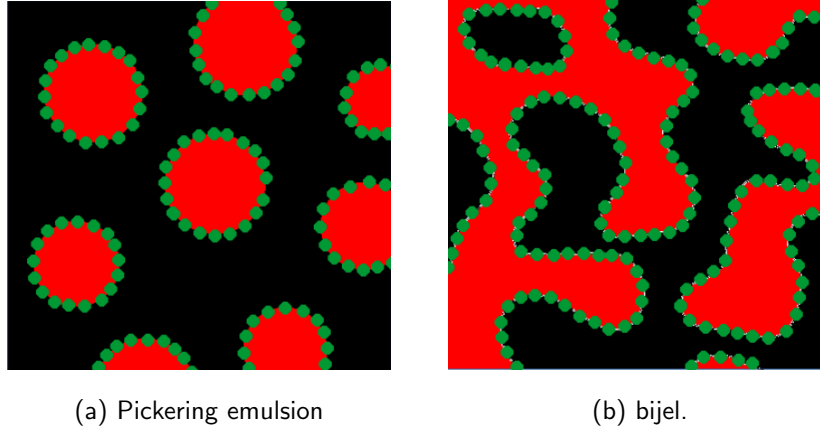
Figure 1.1: Sketch of particle-stabilized (Pickering) emulsion and a bijel. In both cases the oil and water (red and black) are phase-separated and the microparticles (green) are embedded in the interfaces. The emulsion has spherical oil-water interfaces, while the bijel has a complex curved interface.

ability of being dislodged by a thermal fluctuation, the particle is, in contrast to surfactant molecules, said to be irreversibly absorbed.

The interface as a whole retains some surface tension due to 'bare' interfacial area between the absorbed particles. Even with the addition of surfactants, the interface has small but nonzero surface tension. Freely suspended emulsion droplets are usually spherical, as spheres are the equilibrium shape of a fluid droplet with positive surface tension. However, their morphology also depends on formation history. Due to the fixed number of adsorbed particles and jamming within the particle layer, non-spherical droplet shapes can result. Fluid dynamic effects such as viscosity in the surrounding fluids can further inhibit global rearragements and add subtleties to the sequence of formation dynamics. With specialized mixing protocols, it is possible to manufacture emulsions with long-lived elongated, irregular, or even branched and interconnected droplets [6, 7]. Non-spherical shapes, including tori, have also been created in individual macroscopic fluid droplets [8].

In general, there are a range of morphologies and stabilization mechanism in solid-stabilized emulsions. Particles may form monolayers, multiple layers, sparse aggragegates, or even a stabilizing gel-like network in the fluid matrix

3
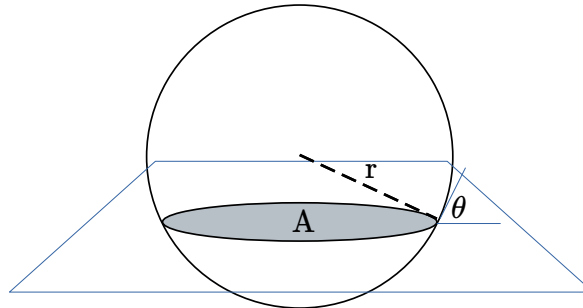
Figure 1.2: An individual particle in an interface.

[4]. However, I will focus exclusively on the idealized special case of droplets covered by dense particle monolayers. This type of solid-stabilized emulsion occurs, for example, in our simple experimental model Pickering emulsion in Chapter 5.

In an interfacial monolayer, there is a complex array of interactions between particles, depending on the particle material, roughness, chemical functionalization; interparticle interactions are potentially mediated by interfacial geometry as well as by both fluid phases. For example, electrostatic repulsion mediated by the oil phase causes widely spaced arrays of particles, while short-range attraction causes aggregated networks [9]. We here focus on hard-sphere or hard-rod particles, which form closely packed monolayers.

1.1.2 Bijel

Oil and water can form an oil-in-water (o/w) emulsion or a water-in-oil (w/o) 'inverse' emulsion. Which type of emulsion is formed depends on factors such as fluid volume fractions, surfactant molecule hydrophobic-lipophilic balance or surfactant particle wetting properties, and dynamical factors of the mixing process such as fluid viscosities and shear rates. In addition, there exists a third option, where both fluids constitute the 'outside', continuous phase. When stabilized by particles, such a material is called a bijel, or bicontinuous interfacially jammed emulsion gel. Solid-stabilized emulsion and bijel compositions

are shown schematically in Figure 1.1-b.

The possibility of a particle-stabilized bijel was first discovered computationally in 2005 by Stratford *et al.* [10]. Perfectly bicontinuous bijels can be created experimentally when two fluids demix, as temperature is lowered, via the spinodal decomposition. The bicontinuous spinodal structure is 'frozen in' as a jammed layer of nanoparticles occupies the interfaces and prevents further coarsening.This experimental procedure was established in 2008 by Herzig *et al.* [11]. Emerging applications of bijels take advantage of the large amount of interfacial area accessible to a fluid or gas, for example in desalination across the interface [12] or in hydrogen gas storage in a derived porous solid[13].

Like the emulsion, the bijel is a metastable state of the fluid-fluid-particle system. Its existence and morphology are history-dependent, encoding the kinetics during the formation process [10], while the lowest energy state is two macroscopically phase separated fluids phases. The bijel is in some sense doubly metastable: the bijel will decay into an emulsion and finally to phase-separated fluids. Stability against the first stage of bijel decomposition is investigated here.

In bijels as well as in elongated emulsions droplets, necks connect different droplets or regions of fluid. The long-term stability of these structures against pinching off to droplets determines permanence of the material against aging and is one proposed indicator of bijel stability [10]. To model such a neck, we will examine an axisymmetric sinusoidally perturbed cylinder shape. The breakup of cylinders of complex fluids into droplets is also relevant to the emulsion formation process as well as, more generally, being of interest in a range of technological contexts such as inkjet printing [14].

1.2 Ordered soft interfaces

1.2.1 Orientational order

In three dimensions, a hard-sphere fluid crystallizes at low tempertures to a solid phase with long-range translational order [15]. In contrast, in two dimensions, true long-range order is not possible (Mermin-Wager theorem) [16]. In addition, KTHNY (Kosterlitz, Thouless, Halperin, Nelson, and Young) theory

posits a two-step melting process between two-dimensional crystalline and isotropic phases; there is an intermediate, orientationally ordered phase known as the hexatic phase [17]. Despite dislocations, which disrupt translational order in particle positions, the orientation of the pattern remains correlated at quasi-long-range (algebraic decay) [16].

Microscale spherical colloidal particles have a long history as 'model atoms', for example to experimentally verify hard-sphere crystallization in three dimensions [18]. Similarly, in two dimensions, a carefully controlled monolayer of colloidal spheres can reproduce the predicted hexatic phase [19–21]. While less ideal, the same phenomenon of hexatic orientational order is observed in monolayers of colloidal particles at liquid-liquid interfaces [22]. Apparent local hexatic order of particles on spherical emulsion droplets is frequently seen in images in the course of other experiments [23–26]

Hexatic order, with locally hexagonal ($n = 6$) discrete rotational symmetry, is just one example of orientational or 'n-atic' order. Other possible orientationally ordered phases (Figure 1.3) are the rare square-tiled tetratic phase ($n = 4$) [28] as well as the nematic phase ($n = 2$) common in liquid crystals and other rod-like particles with two indistinguishable ends. Polar or otherwise directed elongated particles form vector or 1-atic order. Lastly, while locally triangular tilings ($n = 3$) are also possible, they are dual to and synonymous with locally hexagonal tilings [27].

1.2.2   Order on curved surfaces

In two dimensions, patterns with the discrete rotational symmetry groups listed above tile a Euclidean plane. On the other hand, on surfaces with nonzero Gaussian curvature, it is easy to imagine that the same regular patterns become locally distorted. In addition to local curvature, the global topology of a surface sets contraints on the extent to which orientational order is possible. It is not possible, for example, to cover the entire surface of a sphere with a defect-free vector field or with a perfect square or hexagonal tiling. This principle is formally encoded in the Poincare-Hopf theorem. There must be at least $n\chi$ defects [29] in an n-atic field on a surface of topological genus g and Euler characteristic $\chi = 2 - 2g$. For example, there are 12 defects (sites with five rather than six

(a) Vector order ($n = 1$).

(b) Nematic order ($n = 2$).

(c) Tetratic order ($n = 4$).

(d) Hexatic order ($n = 6$).
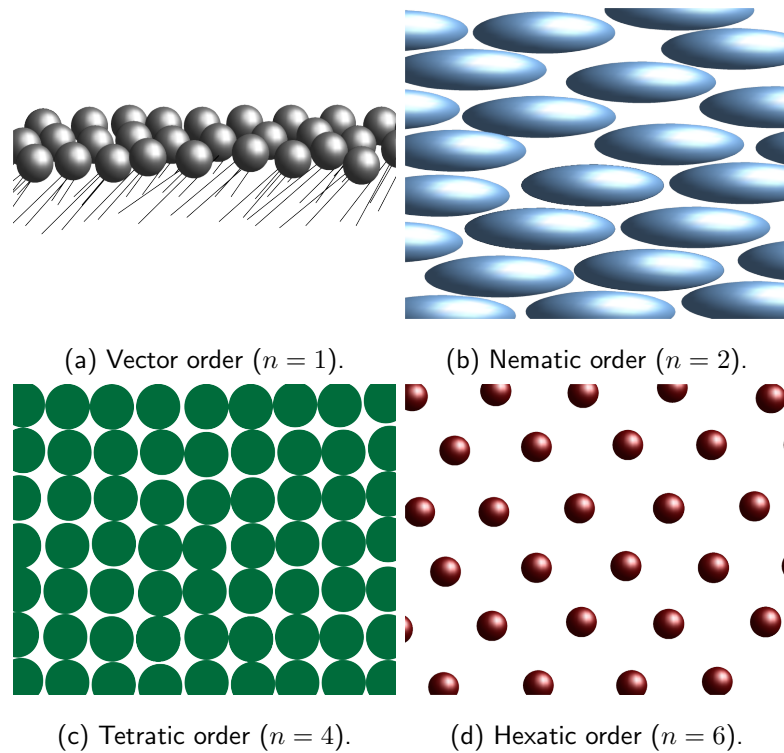
Figure 1.3: Examples of different types of orientational order. (a) Vector ($n = 1$) order could exist in a tilted layer of surfactant molecules or in oriented polar molecules or particles. (b) Nematic ($n = 2$) order exists in the orientations of elongated molecules or particles. (c) The rare tetratic ($n = 4$) phase can exist in the orientations of square particles or in the positions with particles arranged in a square lattice, for example due to quadrupole interaction. (d) Hexatic ($n = 6$) order most commonly exists in the positions of sphere or point particles.

neighbors) in hexatic order on a sphere; two defects (source or sinks) in a vector field on a sphere (genus $g = 0$); and four defects in a nematic material on a sphere. The relation between Gausssian curvature and n-atic tilings has been studied extensively with the point of view of discrete particles and/or discrete defects.

Locally, we can picture that a vector field or hexagonal tiling is distorted away from a perfectly parallel configuration by surface curvature. Gaussian curvature, an intrinsic quality of the surface, induces distortions in a vector or other n-atic field. On the other hand mean curvature, related to the embedding of a two-dimensional surface in three-dimensional space, has no effect on orientational order. For example, orientational order is equally compatible with a cylinder and a plane.

1.2.3   Effect of order on interface shape

Where orientational order, as the flat-space equilibrium phase of the interfacial material, and Gaussian curvature of the otherwise preferred droplet shape are incompatible, several outcomes may result. The interfacial material may remain ordered, but adapt to surface shape and topology via small distortions and isolated defect cores. Alternatively, if distortions and defects are energetically too costly, orientational order may be destroyed everywhere, with the material adopting an isotropic phase. Lastly and most significantly, the shape of soft interfaces may deform to minimize curvature-induced distortion to the interfacial material. Thus spherical droplets may adopt polyhedral shapes, offering flat facets compatible with orientational order and concentrating the topological unavoidable net Gaussian curvature at vertices [27, 30–33]. One can speculate that interfaces may be driven to change topological genus and adopt alternative phases, for example a lamellar phase consisting of flat planar interfaces. The possibility of order-induced shape and phase changes in emulsion droplets has obvious significance for emulsion formulation and stability. Furthermore, the possibliity of engineering nano- or microscale droplets with predictble polyhedral or defect-bearing shapes opens up avenues for novel nanomaterials [33].

The facetting of topological spherical droplets into icosahedra due to hexatic order has been experimentally observed in certain designed surfactant-stabilized

emulsion systems, see review by Marin *et al.* [33] for example. In solid-stabilized emulsions with relatively large particles, apparent facetting seen in other experiments with relatively large particles [8] hints that similar phenomena are possible.

1.3 Methods and model

1.3.1 Equilibrium energy

Throughout this thesis I take an equilibrium statistical physics approach, examining the energy of various configurations of the system to predict the energy-minimizing state that will be realized at low temperatures. The statistical approach has a history of application to interfaces and membranes, see, for example, [34–36]. Similar energetic considerations have been applied to solid-stabilized emulsion droplets by [37–39].

Huse and Leibler [36] divide the system's complete Hamiltonian into 'external' (E) and 'internal' (I) parts; the same terminology will be used here:

$$\mathcal{H} = \mathcal{H}_E + \mathcal{H}_I. \tag{1.1}$$

The external Hamiltonian contains terms unrelated to internal degrees of freedom in the arrangement of particles or molecules in the interface. As external Hamiltonian, I use the Helfrich Hamiltonian, a widely used theory of lipid bilayers.

The internal Hamiltonian collects terms relating to the configuration of orientational order on the surface. This includes terms in which the order parameter field interacts with surface shape and curvature. A general Landau-Ginzburg energy of orientational order is substituted for $\mathcal{H}_I$ in Chapters 2 to 4, while a distortion free energy of a nematic hard rod material is substituted in Chapter 6.

To complement the analytic approach, I formulate a Markov Chain Monte Carlo simulation to sample configurations of the orientationally ordered material on a curved surface.

1.3.2 Continuum field theory

In solid-stabilized emulsions, the interfacial material consists of individual nano- or microparticles. While in limiting cases the relative size of interfacial particles and number of interfacial particles on a droplet is such that a theory of the packing of discrete spherical particles would be more appropriate, a continuum field theoretical approach is used here, in line with the literature on molecular surfactant monolayers. The arrangement of the point particles is abstracted into an order parameter field, which quantifies order at each point on the manifold. A Hamiltonian derived from this order parameter field is added to the composite system's energy. By minimizing the full system's energy, the equilibrium or ensemble configuration of the order parameter field can then be predicted, either by varying the order parameter field on a fixed surface shape or by minimizing for order parameter field and the surface shape simultaneously.

1.3.3 Model surface

Throughout this thesis I examine a specific model surface, a sinusoidally modulated cylinder.

The theory of hexatic order was first explored on spheres [30, 31] and tori [40, 41]. Other model surfaces that have been studied include a catenoid surface [42], and the paraboloid of revolution [43] as well as variations on locally near-planar surfaces.

In view of modelling the morphology of a bijel, other potentially useful model surfaces are the triply periodic bicontinuous phases, including cubic and gyroid [44] variants. These structures are more regular variants of the amorphous bicontinuous morphology of a bijel. Study of these objects highlights the effect of regions with negative Gaussian curvature.

1.4 Research questions

The morphology of solid-stabilized emulsion droplets and of interesting related structures is not necessarily dominated by surface tension. As such, the morphology is not necessarily sphere-like. Solid-stabilized particle layers present new

opportunities, over surfactant-stabilized systems, in terms of exotic emulsion morphology and precisely engineered emulsion droplets, but present us with a modeling challenge. To investigate possible effects of interfacial orientational order on morphology, we need to adapt previous models of hexatic order in molecular monolayers.

The goals of this thesis include answering the following questions: What insights can be gained from applying the continuum theory of orientationally ordered soft interfacial materials to solid stabilized emulsions? What can we substitute or add to the model to account for differences? What is the effect on the system when orientational order and shape are in some way incompatible? What effect does orientational order in monolayers of larger spherical or rod-like nanoparticles have on the morphology and stability of emulsion droplets, in particular elongated droplets and channels?

1.5   Outline

In Chapters 2-4, I explore existing models for interfaces with molecule-scale surfactants in the setting of modulated axisymmetric vesicles. In Chapter 2, known formulae for the stability of axisymmetric membranes with global mechanical properties are re-derived and examined closely in light of the ergodic approach which will be used later. In Chapter 3, a continuum orientational order parameter field is added, following methods established for mono- and bilayers of molecule-scale surfactants, and consequences are predicted analytically. In Chapter 4, the Monte Carlo simulation method is established; results for the system described in Chapter 3 are confirmed and refined. In Chapter 5, we revisit solid-stabilized experimental systems. Experimental observations on colloidal monolayers and particle-stabilized emulsions are discussed, based on the literature and on two experiments. Finally in Chapter 6, the adaptation of the model and methods to represent interfacial layers of larger rodlike colloidal particles is completed with a new model of density and orientational order in the interfacial layer, whose parameters are derived from a density functional theory. Consequences of applying a hard rod fluid model as the interfacial particle layer are examined. Chapter 7 summarizes and concludes the thesis, contextualizes

the methods and outcomes with respect to the literature, and proposes further investigations.

Bibliography

[1] H. Jiang, Y. Sheng, and T. Ngai, Curr Opin Colloid Interface Sci **49**, 1 (2020).

[2] C. C. Berton-Carabin and K. Schroën, Annu Rev Food Sci Technol **6**, 263 (2015).

[3] B. P. Binks, Curr Opin Colloid Interface Sci **7**, 21 (2002).

[4] R. Lopetinsky, *Solids-stabilized emulsions: a review* (Cambridge University Press, 2006), pp. 186–224.

[5] G. B. Davies, T. Krüger, P. V. Coveney, and J. Harting, J Chem Phys **141**, 154902 (2014).

[6] C. Huang *et al.*, Nature Nanotechnol **12**, 1060 (2017).

[7] D. Cai, P. S. Clegg, T. Li, K. A. Rumble, and J. W. Tavacoli, Soft Matter **13**, 4824 (2017).

[8] A. B. Subramaniam, M. Abkarian, L. Mahadevan, and H. A. Stone, Nature **438**, 930 (2005).

[9] T. S. Horozov, R. Aveyard, J. H. Clint, and B. P. Binks, Langmuir **19**, 2822 (2003).

[10] K. Stratford, R. Adhikari, I. Pagonabarraga, J.-C. Desplat, and M. E. Cates, Science **309**, 2198 (2005).

[11] E. M. Herzig, K. A. White, A. B. Schofield, W. C. Poon, and P. S. Clegg, Nat Mater **6**, 966 (2007).

[12] M. F. Haase *et al.*, Nat Comm **8**, 1 (2017).

[13] M. N. Lee and A. Mohraz, Adv Mater **22**, 4836 (2010).

[14] S. D. Hoath *et al.*, J Nonnewton Fluid Mech **205**, 1 (2014).

[15] R. A. L. Jones*Soft condensed matter* Vol. 6 (Oxford University Press, 2002).

[16] P. M. Chaikin and T. C. Lubensky, *Principles of condensed matter physics* (Cambridge university press Cambridge, 1995).

[17] B. Halperin and D. R. Nelson, Phys Rev Lett **41**, 121 (1978).

[18] W. Poon, Science **304**, 830 (2004).

[19] P. Keim, G. Maret, and H. H. von Grünberg, Phys Rev E **75**, 031402 (2007), 0610332.

[20] A. L. Thorneywork, J. L. Abbott, D. G. Aarts, and R. P. Dullens, Phys Rev Lett **118**, 158001 (2017).

[21] A. L. Thorneywork, J. L. Abbott, D. G. Aarts, P. Keim, and R. P. Dullens, J Phys Condens Matter **30**, 104003 (2018).

[22] B.-J. Lin and L.-J. Chen, J Chem Phys **126**, 034706 (2007).

[23] R. McGorty, J. Fung, D. Kaz, and V. N. Manoharan, Mater Today **13**, 34 (2010).

[24] T. S. Horozov and B. P. Binks, Angew Chem **118**, 787 (2006).

[25] F. Gautier *et al.*, Phys Chem Chem Phys **9**, 6455 (2007).

[26] S. Tarimala and L. L. Dai, Langmuir **20**, 3492 (2004).

[27] R. M. L. Evans, *A theoretical investigation of orientational order in liquid crystal vesicles*, PhD thesis, The University of Manchester, 1995.

[28] D. R. Nelson and B. Halperin, Phys Rev B **19**, 2457 (1979).

[29] M. J. Bowick and L. Giomi, Adv Phys **58**, 449 (2009).

[30] J.-M. Park, T. C. Lubensky, and F. C. MacKintosh, EPL **20**, 279 (1992), 9606105.

[31] C.-M. Ghim and J.-M. Park, J Phys Condens Matter **15**, 3891 (2003).

[32] J. Lidmar, L. Mirny, and D. R. Nelson, Phys Rev E **68**, 051910 (2003).

[33] O. Marin, M. Tkachev, E. Sloutskin, and M. Deutsch, Curr Opin Colloid Interface Sci (2020).

[34] D. Nelson, T. Piran, and S. Weinberg, *Statistical mechanics of membranes and surfaces* (World Scientific, 2004).

[35] S. A. Safran, *Statistical thermodynamics of surfaces, interfaces, and membranes* (CRC Press, 2018).

[36] D. A. Huse and S. Leibler, J Phys (Paris) **49**, 605 (1988).

[37] P. Kralchevsky, J. Eriksson, and S. Ljunggren, Adv Colloid Interface Sci **48**, 19 (1994).

[38] N. Taccoen, F. Lequeux, D. Z. Gunes, and C. N. Baroud, Phys Rev X **6**, 011010 (2016).

[39] K. Danov, D. Petsev, N. Denkov, and R. Borwankar, Journal Chem Phys **99**, 7179 (1993).

[40] R. M. L. Evans, Eur Phys J **5**, 507 (1995), 9410010.

[41] L. Giomi and M. J. Bowick, Eur Phys J E **27**, 275 (2008).

[42] M. J. Bowick and Z. Yao, EPL **93**, 36001 (2011).

[43] L. Giomi and M. Bowick, Phys Rev B **76**, 054106 (2007).

[44] S. T. Hyde, Curr Opin Solid State Mater Sci **1**, 653 (1996).

CHAPTER 2

Mechanics of modulated cylindrical interfaces

Abstract

In this chapter I introduce the geometry of the model surface used throughout this thesis, a sinusoidally modulated cylinder. The stability of an axisymmetric interface or membrane subject to surface tension and bending rigidity effects is examined, retrieving length criteria for the stability of membrane tubules. I compare linear stability analysis with results from the energetics of more strongly modulated channel shapes, finding nucleation phenomena and metastable states overlooked in the linear analysis. The energy functions describing membrane mechanics will be additively built on throughout the rest of this thesis.

Table 2.1: Table of symbols, Chapter 2

symbol	meaning
$\hat{e}_\rho$, $\hat{e}_\theta$, $\hat{e}_z$	basis of a cylindrical coordinate system in $\mathbb{R}^3$
$\hat{t}_\theta$, $\hat{t}_z$	basis of a coordinate system on the tangent plane of the surface
r_0	the radius of the unmodulated cylinder
$r(a)$	mean radius of the modulated cylinder with conserved volume
$r(a,z)$	local radius of the modulated cylinder
a	amplitude of the shape modulation
λ	wavelength of the shape modulated
k	wavenumber $2\pi/\lambda$ of the shape modulation
k_c	critical wavenumber for stability
A	surface area
A_0	surface area of the unmodulated cylinder
$\mathcal{H}_E$	external Hamiltonian; energy from interfacial mechanics
$\mathcal{H}_E^{surf}$	surface-tension-related part of the energy
$\mathcal{H}_E^{curv}$	curvature-related part of the energy
γ_0	microscopic surface tension
γ	effective surface tension
κ	bending rigidity with respect to mean curvature
$\bar{\kappa}$	bending rigidity with respect to Gaussian curvature
C_0	spontaneous total curvature
H	mean curvature
K	Gaussian curvature
K_j^i	curvature tensor
g_{ij}	metric on the tangent plane
η_{ij}	metric of the cylindrical polar coordinate system
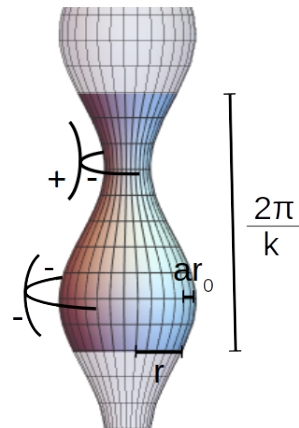
Figure 2.1: An illustration of the undulating cylinder surface. A section of the surface of length $\lambda = 2\pi/k$ is highlighted; the model surface is an infinite periodic repetition of this section. In this illustration the amplitude a of the sinusoidal modulation is 0.5 (in units of r_0). The surface has both positive and negative principal curvatures.

2.1 Geometry

Throughout this thesis, I examine a model surface consisting of a cylinder with a sinusoidal modulation in radius (Figure 2.1). This model surface is interesting because it features spatially varying curvature, including both positive and negative principal curvatures. With small perturbations, the surface is standard for the study of instability of liquid threads, jets, or bridges, [1–3] as occur in emulsion formation or in complex emulsions. Structures with larger shape modulations also occur. While these are possibly unduloid, a minimal surface, the sinusoid is a close model. More loosely, the sinusoidally modulated cylinder represents more irregularly modulated elongated emulsion droplets and bridges

in solid-stabilized emulsion-like materials. Stability of particle-coated channels is one of two indicators of bijel stability [4].

The surface is defined by a parametric equation in a cylindrical polar coordinate basis ($\hat{e}_\rho$, $\hat{e}_\theta$, $\hat{e}_z$):

$$\mathbf{x}(\theta, z) = r(a)(1 + a\sin(kz))\hat{e}_\rho + z\hat{e}_z \tag{2.1}$$

The system is constrained to a constant volume such that $V(a) = V_0 = (2\pi)^2 r_0^2/k$. On introduction of a sinusoidal perturbation with amplitude $a \neq 0$, the mean radius $r(a)$ must scale as

$$r(a) = \frac{r_0}{\sqrt{1 + a^2/2}}. \tag{2.2}$$

The system is characterized by radius r_0, wavenumber k, and shape amplitude a. Although the system is periodic, I consider a section of cylinder of length $\lambda = \frac{2\pi}{k}$. Without loss of generality I define the length unit of the system by setting $r_0 = 1$. The amplitude a of the deformation is then a dimensionless parameter in the range $-1 < a < 1$.

We can also construct a two-dimensional coordinate system intrinsic to the surface. The basis vectors of this coordinate system are two orthonormal tangent vectors (Figure 2.2) defined as:

$$\hat{t}_i = \frac{\partial_i \mathbf{x}}{|\partial_i \mathbf{x}|}. \tag{2.3}$$

Here

$$\begin{aligned}
\hat{t}_\theta &= \hat{e}_\theta \\
\hat{t}_z &= \frac{r(a)ak\cos(kz)\hat{e}_\rho + \hat{e}_z}{\sqrt{g_{zz}}},
\end{aligned} \tag{2.4}$$

with g_{zz} defined below. The azimuthal tangent vector $\hat{t}_\theta$ is identical to the extrinsic basis vector $\hat{e}_\theta$. In contrast, axial tangent vector $\hat{t}_z$ is in general not parallel to $\hat{e}_z$. Instead, it has a component in the radial direction.

The unit normal vector is defined as

$$\hat{n} = \frac{\hat{t}_\theta \times \hat{t}_z}{|\hat{t}_\theta \times \hat{t}_z|}. \tag{2.5}$$

Via the usual chirality of the cylindrical coordinate system and via the order of terms in this cross product, the normal vector is defined as pointing outwards.
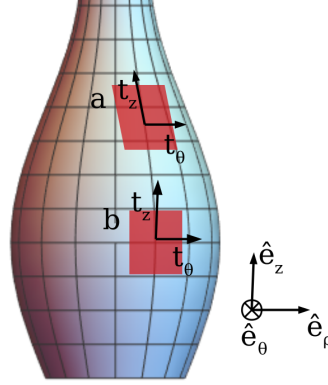
Figure 2.2: The extrinsic coordinate basis consists of the basis vectors $(\hat{e}_\rho, \hat{e}_\theta, \hat{e}_z)$ of the cylindrical polar coordinate system. Two examples of intrinsic basis vectors $(\hat{t}_\theta, \hat{t}_z)$, spanning local tangent planes a and b on the modulated cylinder, are illustrated. In all locations on the surface, $\hat{t}_\theta = \hat{e}_\theta$. In general $\hat{t}_z$ is not equal to $\hat{e}_z$, as seen in tangent plane a. Only in specific cases $z = \pi/(2k), 3\pi/(2k), ...,$ represented by b, does $\hat{t}_z$ coincide with $\hat{e}_z$.

The metric tensor g_{ij} is defined in the extrinsic (e_θ, e_z) basis as

$$g_{ij} = \partial_i \mathbf{x} \cdot \partial_j \mathbf{x}; \tag{2.6}$$

here it is

$$
\begin{aligned}
g_{\theta\theta} &= r(a, z)^2, \\
g_{zz} &= 1 + a^2 r(a)^2 k^2 \cos^2(kz), \\
g_{\theta z} &= g_{z\theta} = 0.
\end{aligned}
\tag{2.7}
$$

The square root of the metric determinant, here $\sqrt{g} = \sqrt{g_{\theta\theta} g_{zz}}$, can be seen as describing the relative size of an infinitesimal area element and is used as the measure of integrals over the surface:

$$\sqrt{g} = r(z)\sqrt{g_{zz}} = r(a)(1 + a\sin(kz))\sqrt{r(a)^2 a^2 k^2 \cos^2(kz) + 1}. \tag{2.8}$$

The factors $\sqrt{g_{ii}}$ can be seen as giving the length of infinitesimal line elements in azimuthal and axial directions on the surface.

The metric inverse $g^{ij} = g_{ij}^{-1}$ is

$$g^{\theta\theta} = 1/g_{\theta\theta},$$
$$g^{zz} = 1/g_{zz} \tag{2.9}$$

.

The curvature tensor K^i_j can be derived as $K_{ij} = \partial_i \partial_j \mathbf{x}$, $K^i_j = K_{kj} g^{ki}$ [1]. Here its elements are

$$K^\theta_\theta = \frac{-1}{\sqrt{g_{zz}} r(a,z)},$$
$$K^z_z = \frac{-r(a)ak^2 \sin(kz)}{(g_{zz})^{3/2}}. \tag{2.10}$$

In the (e_θ, e_z) basis, the shape operator of the surface of revolution is diagonal. When diagonal, its elements correspond to the two principal curvatures (inverse of two principal radii of curvature) at each point. Mean curvature H and Gaussian curvature K are given by trace and determinant of the diagonal shape operator respectively, $2H = K^\theta_\theta + K^z_z$ and $K = K^\theta_\theta K^z_z$.

I will also use the spin connection A_i. The spin connection corrects for changes in vector quantities induced by parallel transport on curved surfaces, allowing comparison of a vector field at two distant points. One way to derive the spin connection is $A_i = \mathbf{t}_\theta \cdot \partial_i \hat{t}_z = -\mathbf{t}_z \cdot \partial_i \mathbf{t}_\theta$.[2] The spin connection for the given surface is

$$A_z = 0$$
$$A_\theta = \frac{r(a)ak \cos(kz)}{\sqrt{g_{zz}}}. \tag{2.11}$$

The spin connection is related to Gaussian curvature via the Mermin-Ho relation [5, 6]

$$K = \hat{n} \cdot [\nabla \times \Omega] = \frac{1}{2} \epsilon_{\alpha\beta\gamma} n^\gamma \epsilon_{ijk} n^k \partial_i n^\alpha \partial_j n^\beta, \tag{2.12}$$

---

[1] The object generically called 'the curvature tensor' here is equivalent to the shape operator, Weingarten map, or coefficients of the second fundamental form.

[2] Equivalent to Christoffel symbols (first kind: 3 lower indices) in the Levi-Civita connection, $A_i = \Gamma_{\theta i z} = -\Gamma_{zi\theta}$. All other Γ_{ijk} $(i, j, k = z, \theta)$ are zero. Like the Levi-Civita connection, in general the spin connection does not transform like a tensor. However, in the form defined here indexes can be raised and lowered the usual way, with metric η_{ij} of the cylindrical coordinate basis, in parallel to those of the derivative operator.
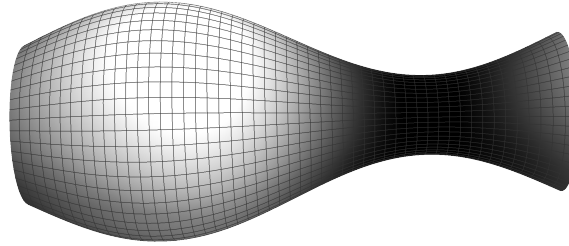
(a) The value of $\sqrt{g}$, corresponding to the relative size of area elements, is indicated by shading on the surface.
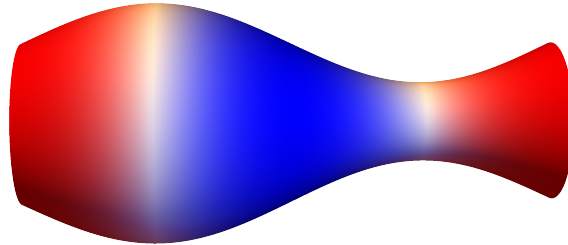
(b) Spin connection component A_θ takes negative (blue) and positive (red) values.

Figure 2.3: Square root of metric determinant $\sqrt{g}$ and spin connection component A_θ as shading on the surface shape on the example of a surface with $k = 1$, $a = 0.5$.

where Ω is a variant spin connection[3]. While values of the spin connection components depend on choice of coordinate system, the vector $[\nabla \times \Omega]$ and Gaussian curvature do not.

---

[3] Just as there are two different conventions for the Christoffel symbols, using either ∂_i or ∇_i, are in use [7], note that some references [6] work instead with spin connection $\Omega_i := \mathbf{t}_\theta \cdot \nabla_i \hat{t}_z$. In cylindrical coordinate systems, the value of the spin connection component Ω_θ differs from ours by a factor of $1/\sqrt{g_{\theta\theta}} = 1/r(a, z)$.

2.2 Instability induced by surface tension

A long-standing question of interest is whether a fluid cylinder or jet is stable with respect to small sinusoidal perturbations. Fluctuations, which can be generically decomposed into sinusoids, naturally occur in noisy or thermal environments. If any such initial perturbations grow, the system is unstable; it is commonly extrapolated that the cylinder will break up into spherical droplets. Conversely if all sinusoidal perturbations decay the system is linearly stable. The longest wavelength perturbation a fluid cylinder can support is determined by its length. The question of whether perturbations of a certain wavelength or wavenumber are unstable is equivalent to the question of which finite-length cylindrical objects are stable.

In early experiments by Plateau, it was observed that fluid cylinders longer than a certain length-diameter ratio $\lambda_0/2r \approx \pi$ are unstable to breakup [8]. Rayleigh theoretically explained the stability citerion as well as further results via both enegetic and hydrodynamic routes [1]. In this thesis I focus on deriving stability criteria via perturbative energy analysis. For systems dominated by surface tension, energy is given by

$$
\begin{aligned}
\mathcal{H}_E^{surf} &= \gamma_0 \int_S dS \\
&= \gamma_0 \int_0^\lambda \int_0^{2\pi} \sqrt{g} d\theta dz
\end{aligned}
\tag{2.13}
$$

with $\sqrt{g}$ as in Equations 2.8. For a small shape perturbation with shape amplitude $|a| \ll 1$, I insert the series expansion

$$
\sqrt{g} = 1 + \sin(kz)a + \left(\frac{k^2 \cos^2(kz)}{2} - \frac{1}{4} \right) a^2 + O(a^3);
\tag{2.14}
$$

note that this includes the series expansion of the factor $r(a) = \frac{1}{\sqrt{1+a^2/2}} r_0$.

Carrying out the integral 2.13, the next-to-leading-order term in energy is then

$$
\frac{\Delta \mathcal{H}_0^{surf}}{A_0 a^2} = \frac{\gamma_0}{4} \left(r_0^2 k^2 - 1 \right),
\tag{2.15}
$$

denoting the surface area of a section of unperturbed cylinder of length λ as $A_0 = 2\pi\lambda$. Roots of Equation 2.15 give the well-known Plateau-Rayleigh

instability criterion: the energy difference on introduction of a small perturbation of amplitude a is negative and the perturbation grows for wavenumbers $k < k_c = 1$ (in units where $r_0 = 1$).

The total surface area of a cylinder grows when the sinusoidal perturbation is introduced due to an increased axial path length along the sinusoid. However, due to conserved volume, the mean radius $r(a)$ also decreases globally when a perturbation is introduced, resulting in an overall narrower modulated cylinder and a corresponding decrease in surface area corresponding to the second term in Equation 2.15. Which of these effects dominates depends on the wavelength of the perturbation, with longer-wavelength perturbations tending to decrease the overall surface area and destabilize the system.

Equivalent hydrodynamic instability

Throughout this thesis I build on the equilibrium energetic approach as outlined above for the simplest case. On the other hand, the more common derivation of the PR instability is given by the hydrodynamic approach, incorporating local forces and the dynamics of the surrounding fluids. The hydrodynamic approach is discussed in this section to show that the two approaches, despite the apparent differences, are mathematically equivalent as far as obtaining the linear stability criterion. The hydrodynamic approach has the advantages of retrieving further information such as dispersion relation (growth rate as a function of wavenumber, allowing the identification of the fastest-growing modes and thus predicting the size of the resulting droplets) and timescale, but is only applicable in the perturbative regime. It allows the incorporation of other fluid-dynamic factors, such as fluid viscosities.

In general, prior to imposing a volume constraint, the energy of a system such as a droplet is [9]

$$E = \gamma \int_S dS + p \int_V dV. \tag{2.16}$$

In the hydrodynamic route, the pressure-volume contribution to energy is retained and no volume constraint is explicitly imposed. Locally

$$\gamma \int \sqrt{h} d\theta dz = \gamma \int (1 + 2H\delta r + ...)\sqrt{h_0} d\theta dz, \tag{2.17}$$

where metric h_{ij} is the metric tensor of the non-volume-conserving modulated cylinder

$$\vec{y} = r_0(1 + a\sin kz)\hat{e}_\rho + z\hat{e}_z \tag{2.18}$$

and $\sqrt{h_0} = \sqrt{g_0} = r_0$ denotes its value on the unperturbed cylinder. Thus

$$\sqrt{h} = r_0(1 + a\sin kz)\sqrt{1 + a^2k^2r_0^2\cos^2 kz}, \tag{2.19}$$

while $\sqrt{h_0}$ is the metric of the unperturbed cylindrical surface

$$\sqrt{h_0} = r_0. \tag{2.20}$$

The total curvature $2H$ is, to first order, the variational derivative of surface area as a surface element is displaced radially to a parallel position, per unit area of the initial surface shape. It is obtained by dividing the first variation in $\sqrt{h}$ by $\sqrt{h_{\theta\theta}}$, the measure of the integral in the cylindrical coordinate system [10].

The pressure-volume term in Equation 2.16 is given to linear order by [9]

$$pV = p\int (r + \delta r + ...)\sqrt{h_0}\,d\rho\, d\theta\, dz, \tag{2.21}$$

Equating integrands, we obtain the Laplace pressure

$$-p = 2\gamma H. \tag{2.22}$$

In the specific case of a cylinder with a small sinusoidal perturbation, at zeroth order the equilibrium Laplace pressure is

$$-p_0 = \frac{\gamma}{r_0}, \tag{2.23}$$

while at first order a pressure perturbation

$$-\delta p(z) = \frac{\gamma}{r_0}(1 - r_0^2 k^2)a\sin kz \tag{2.24}$$

is induced by the shape perturbation. To fully treat the Plateau-Rayleigh instability, the time-dependent sinusoidal perturbation

$$r = r_0(1 + a\sin kze^{\omega t}) \tag{2.25}$$

in interface position induces analogous perturbations in Laplace pressure and in the radial component of the surrounding fluids' velocity fields [1]. Solutions to the inviscid linearized Navier-Stokes equations in a cylindrical system, with vanishing velocity fields at central and far-field locations, are the Bessel functions of the first kind, $I_0(kr_0)$ and $I_0(kr_0)$. The Laplace pressure difference across the interface supplies another boundary condition joining the inner and outer radial velocity fields. The result is the dispersion relation

$$\omega^2(k) = \frac{\gamma_0 k I_1(kr_0)(1 - k^2 r_0^2)}{\rho r_0^2 I_1(kr_0)}. \tag{2.26}$$

Among other things the same Plateau-Rayleigh instability criterion is implied: solutions with real positive growth rates ω exist for wavenumbers $k_c \leq 1$.

Fundamentally the stability criterion is whether the Laplace pressure perturbation, proportional to differences in total curvature, is positive (aligned) or negative (antialigned) with a fluctuation in the radial fluid velocity field. For the specific case of axisymmetric surfaces in a cylindrical polar basis, the question of stability is exactly equivalent to the question of balancing one principal curvature against the other for an overall positive or negative first order change in total curvature.

For the special case of modulations of a cylinder in the cylindrical basis, two conceptually different changes in local surface area element are encoded in $\sqrt{h_{\theta\theta}}$ and $\sqrt{h_{zz}}$, and in the two principal curvatures K_θ^θ and K_z^z, respectively. In this case a balance between changes to local azimuthal and axial curvatures components is the stability criterion.

On the other hand, to derive the global static energy balance route on a volume-conserving cylinder, used in this thesis, from Equation 2.1, pressure can be seen as a Lagrange multiplier constraining the inner volume to a value $\int_V dV = V_0$ or

$$\int r dr \theta dz = \int r(a) \left(1 + a \sin kz\right) dr d\theta dz$$
$$r(a) = r_0(1 - a^2/2 \int \sin^2 kz dz). \tag{2.27}$$

Minimizing the energy subject to the constraint results in a system of equations whose solution is formally the volume-conserving radius given in Equations 2.2 and the roots of Equation 2.15.

Inserting $r(a)$ into the surface area term, the energy to minimize is, to first order

$$\mathcal{H} = \gamma A = \int (1 + \frac{1}{2}a^2 k^2 r_0^2 \cos^2 kz) r_0 (1 - a^2/2 \int \sin^2 kz dz)(1 + a\sin kz) dz d\theta;$$

(2.28)

the first order difference is Equation 2.15, an $O(a^2)$ energy difference balancing a term $\propto 1$ and a term $\propto k^2$. The $\propto k^2$ effect is derived from the increased axial pathlength; it is clearly related to the axial principal curvature term in the hydrodynamic derivation. On the other hand, the second effect, from the global radius adjustment, is harder to identify with the azimuthal principal curvature term in Equation 2.24. It is in fact analogous to dividing by $\sqrt{h_{\theta\theta}}$ in Equation 2.17.

Despite the apparent differences that second order terms $\propto a^2$ are the leading order energy difference; that a volume-conserving mean radius has been additionally imposed; and that global rather than local energy balance is considered, the resulting instability criterion is the same. The agreement between local and global stability criteria is general to any droplet shape and coordinate basis, but the neat relationship between two opposing forces and two principal curvatures is specific to axisymmetric variations in a cylindrical coordinate basis.

The apparently conceptually distinct procedures of 1) balancing local principal curvatures to obtain local Laplace pressure and 2) adjusting radius to constrain the system yield equivalent results to first order. It is therefore appropriate that Lenz and Nelson [11] take a mixed approach when examining the linear instability criterion of a cylindrical system with hexatic order. They calculate the global energy difference, with volume constraint, of a surface with a hexatic field, but add to this the usual hydrodynamic instability criterion of a surface derived via the hydrodynamic route.

2.3 Systems with surface tension and bending rigidity

Table 2.3 lists a range of experimental systems with typical values for surface tension and bending rigidity.

Table 2.2: Surface tension and bending rigidity of various systems

	Surface tension in erg/cm^2 [4]	bending rigidity in 10^{-13} ergs [5]
Air-water interface		
at $25°C$ [12]	72	-
MD simulation [13]	60	.001
Oil-air interface		
vegetable oils, $23°C$ [14]	$30-32$	-
Oil-water interface		
vegetable triglycerides [15]	$23-26$	-
purified n-decane [16]	53	-
mineral oil [17]	49	-
benzene [17]	33	-
isopropyl myristate [17]	24	-
n-butyl acetate [17]	13	-
benzyl alcohol [17]	3	-
heptane [18]	51	
lutidine (near-critical) [19]	36	-
Soap film [20]	25	-
Oil-water-surfactant		
AOT, alkane, salt water [21]	1	0.42
AOT, heptane, salt water [18]	$10^{-4}-10$	-
CTAB, oil, water [22]	-	$40-4000$
Cell membrane/lipid bilayer		
cholesterol bilayer, closed [23]	0	1
phospholipid bilayer [24]	-	$10-20$
various cells [25]	$.1-.001$	-
HeLa cells, various life stages [26]	$0.2-1.6$	-
bilayer vesicle, pressure applied [27]	$10-10^{-4}$	10
bilayer with cholesterol [28]	-	42

---

[4] $erg/cm^2 = dyn/cm = mN/m$

[5] $erg = 10^{-7}J = 10^{-7}Nm \approx 2.4 \times 10^{13} k_B T$ at $300K$

In general, I label any Lagrange multiplier of a linear surface area term 'surface tension' or 'membrane tension' γ. The surface tension concept used here is agnostic regarding the mechanism causing a resistance to an increase in surface area. Such a surface tension emerges in a wide range of systems through various mechanisms. In the context of emulsions, interfaces between two immiscible fluids have a surface tension due to the energetic cost of intermediate volume fractions. With an interfacial monolayer of surfactant molecules, the surface tension is decreased. In the context of lipid bilayers and cell membranes between two aqueous phases, there is no intrinsic surface tension in equilibrium, but attempts to increase surface area by extending the fluctuating membrane are resisted due to configurational entropy; the system has an emergent surface tension [23].

Additional phenomena acting as an effective surface tension in systems of interest include a dynamic effects of pulling and effects of order. A temporary surface tension can also be dynamically induced in materials lacking an appreciable equilibrium surface tension. For instance, in cylindrical tubes of lipid bilayer, Bar-Ziv and Moses [29] have established an experimental system where a cylindrical lipid vesicle is pulled by optical tweezers, inducing a surface tension. A body of theoretical literature exists on this experimental system. Because the surface tension varies over time and material is displaced, a realistic analysis is necessarily dynamic, finding dynamic effects such as the characteristic velocity of front propagation [30].

Another relevant experimental system is that of cooled emulsion droplets stabilized by a CTAB monolayer [31]. The material has a temperature-dependent energy density of the form $\Delta F = \Delta E - T\Delta S$, where differences are relative to the surfactant dissolved in the bulk fluid [22]. In general, the interfacial and bulk material achieve chemical equilibrium and the relative surface tension is zero. However, as the temperature is dynamically adjusted, the effective surface tension is transiently nonzero. For a newly ordered interfacial material, it can be transiently negative [22].

These cells and lipid bilayer vesicles have a small bending rigidity coefficient on the order of $10k_BT$ or $10^{-12}ergs$. However, the relevance of the bending rigidity term also depends on the radius of curvature, so that small lipid mono-

layer nanotubes [32], for example, are bending-rigidity-dominated and stable. The Föppl-von Kármán number [33]

$$\Gamma = \frac{\gamma r^2}{\kappa} \tag{2.29}$$

encapsulates this relationship; it is of order $1 - 10$ for nanoscale lipid bilayer tubes [33], indicating competition between the two effects.

The model in Equation 2.30 includes a value C_0 for spontaneous curvature, the total curvature which the interfacial material tends to adopt due to various chemical or mechanical effects. A value of zero indicates that a planar configuration minimizes the energy of the interface, while the material resists bending in the sense of mean curvature, for example into a cylinder. A nonzero spontaneous curvature value may be present due to various mechanisms. In solid-stabilized emulsions, wetting properties of the micro- or nano-particle surface are a crucial determinant of emulsion morphology [34]. Non-neutrally-wetting spherical particles lie in the interface asymetrically (Figure 1.2), producing a curved interface on close packing. Similarly, lipid or surfactant molecules are thought to sterically induce a preferred curvature in an interface, which in turn determines the type of emulsion that is formed (Bancroft rule). Cell membranes and lipid bilayers may also have a spontaneous curvature due to assymetry of lipid bilayer sheafs, or by introducing ions, solvents, or variant lipid molecules into one side of the lipid bilayer to increase its area [35, 36]. The membrane eventually regains symmetry due to exchange of material between the two layers, but the difference is long-lived on experimentally relevant timescales. Lastly specialized proteins, such as BAR-domain proteins, can induce an anisotropic spontaneous curvature in cell membranes via their arc-like shape [37, 38].

2.4 Linear stability analysis

To analyze systems with both surface tension and bending rigidity effects, I adopt the Helfrich [39] Hamiltonian

$$\begin{aligned}
\mathcal{H}_E &= \gamma_0 \int_S dS + \frac{\kappa}{2} \int_S (2H - C_0)^2 dS + \frac{\bar{\kappa}}{2} \int_S K dS \\
&= \mathcal{H}_E^{surf} + \mathcal{H}_E^{curv}
\end{aligned} \tag{2.30}$$

with γ_0 membrane or surface tension, H mean curvature (and $2H$ total curvature), C_0 a preferred or spontaneous total curvature value, K Gaussian curvature, and κ and $\bar{\kappa}$ two bending rigidities. As usual the integral stands for $\int_S dS = \int_0^\lambda \int_0^{2\pi} \sqrt{g}\,d\theta dz$, integrating over one period of the surface with the appropriate metric. I label surface area and curvature parts of the external Hamiltonian $\mathcal{H}_E^{surf}$ and $\mathcal{H}_E^{curv}$. The Helfrich Hamiltonian was first proposed as a model for cell membranes [40] and has been widely used since.

The surface is a periodic tube; I take this model literally and assume it is a closed surface of topological genus $g = 1$. On a closed surface of constant topological genus, the total surface integral over Gaussian curvature is a constant $2\pi\chi$, determined completely by the surface's Euler characteristic $\chi = 2 - 2g$ (Gauss-Bonnet theorem). Hence, the third term in Equation 2.30, relating to total Gaussian curvature, is a constant and will be dropped. Expanding the second term in Equation 2.30, a cross-term $-2\kappa K_\theta^\theta K_z^z$ is also proportional to the Gaussian curvature, thus its integral is also a constant. The external Hamiltonian is reduced to

$$
\begin{aligned}
\mathcal{H}_E &= \mathcal{H}_E^{surf} + \mathcal{H}_E^{curv} \\
\mathcal{H}_E^{surf} &= \gamma_0 \int_S dS \\
\mathcal{H}_E^{curv} &= \frac{\kappa}{2} \int_S dS((K_\theta^\theta)^2 + (K_z^z)^2 - 2K_\theta^\theta C_0 - 2K_z^z C_0 + C_0^2)
\end{aligned}
\tag{2.31}
$$

Inserting expressions from Equations 2.10 and 6.8, I expand all analytic functions in Equation 2.31 as series in small a and integrate over one period. Examining the next-to-leading order term, I retrieve the energy difference induced by a small sinusoidal perturbation of amplitude a and wavenumber k:

$$
\frac{\Delta \mathcal{H}_E}{A_0 a^2} = \frac{\gamma}{4}\left(k^2 - 1\right) + \frac{\kappa}{8}\left(2k^4 + (4C_0 - 1)k^2 + 3\right),
\tag{2.32}
$$

where $A_0 = 4\pi^2/k$ is the surface area of a section of length $\lambda = 2\pi/k$ of the unperturbed cylindrical surface. The last term in Equation 2.31 has been absorbed into the effective surface tension $\gamma := \gamma_0 - \frac{1}{2}C_0^2$ and all energy densities are given in units of κ.

Roots of Equation 2.32 are the critical wavenumbers

$$k_c(\gamma_0, C_0) = \frac{1}{2}\left(1 - 2\gamma - 4C_0 \pm \sqrt{8(2\gamma - 3) + (-1 + 4C_0 + 2\gamma)^2}\right)^{1/2}.$$
(2.33)

Smaller wavenumbers (larger wavelengths) than the critical value are unstable, while systems shorter than the critical value are stable.

For the system of tweezed lipid tubules exhibiting the pearling phenomenon, the same limit of stability has been derived in various forms and limits; an overview of the equivalance of various author's results with special cases of Equation 2.33 is given in refernce [41]. The same limit results from the hydrodynamic route or the energy balance route. For example, Granek and Olami [42] follow equivalent steps (i.e. first order energy balance with explicit volume constraint) with the same Helfrich Hamiltonian, although with no spontaneous curvature term, to obtain Equation 2.33 via Equation 2.32 (Eq 16 in their paper), in addition to considering hydrodynamics. In the following sections I review the commonly predicted stability limits in the special cases $C_0 = 0$ (spontaneous curvature omitted), $\gamma_0 = 0$ (vanishing surface tension), and including both effects, before moving on to non-linear analysis.

2.4.1 Neutral spontaneous curvature

First, I set spontaneous curvature to $C_0 = 0$ to represent an interfacial material preferring a neutral (planar) curvature. Equation 2.33 becomes

$$k_c(\gamma_0) = \frac{1}{2}\left(1 - 2\gamma_0 \pm \sqrt{8(2\gamma_0 - 3) + (-1 + 2\gamma_0)^2}\right)^{1/2}.$$
(2.34)

The limiting wavenumbers in the case $C_0 = 0$ are shown in Figure 2.4, plotted against γ_0 and $1/\gamma_0$.

Larger bending-rigidity–surface-tension ratios have a stabilizing effect, rendering increasingly long cylinders stable. For bending-rigidity–surface-tension ratios above a limiting value $\kappa/\gamma_0 = 2/3$, cylinders are stable against fluctuations of all wavelengths [41, 43]. h

2.4.2 Vanishing surface tension

Setting intrinsic surface tension to $\gamma_0 = 0$, as is the case in many systems such as closed lipid vesicles and cell membranes or emulsion droplets in chemical
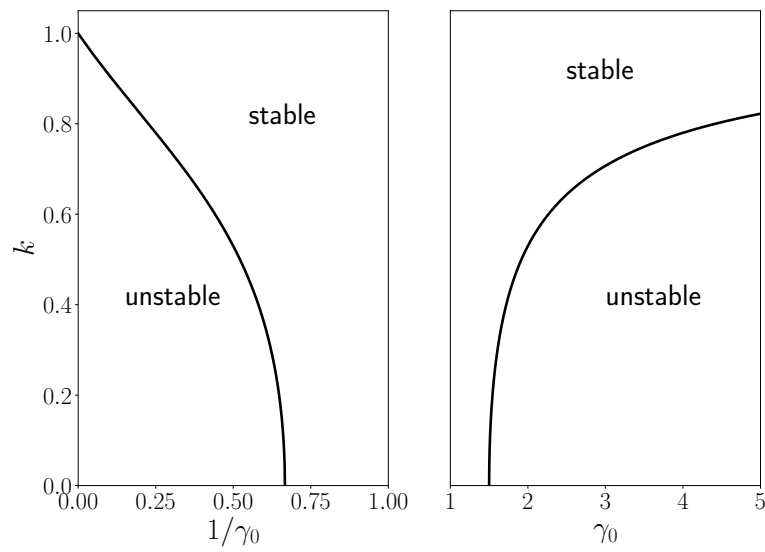
Figure 2.4: Critical wavenumber k_c as a function of surface tension γ_0 (in units where bending rigidity $\kappa = 1$) and as a function of $1/\gamma_0$, i.e. bending rigidity-surface tension ratio. The critical wavenumber (inverse to a critical wavelength) delineates systems which are linearly stable from those which are unstable by cylinder length and bending rigidity.
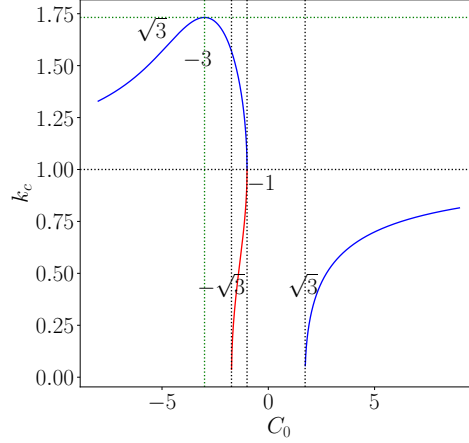
Figure 2.5: Critical wavenumber k_c as a function of spontaneous curvature C_0 in the case of vanishing intrinsic surface tension $\gamma_0 = 0$. While Equation 2.35 has two solutions between $C_0 = -\sqrt{3}$ and -1, only the greater value is meaningful. The equation has no solutions (systems of all lengths are stable) between $C_0 = -1$ and $\sqrt{3}$ and the critical wavenumber reaches a maximum of $k_c = \sqrt{3}$ at spontaneous curvature $C_0 = -3$.

equilibrium with the bulk, Equation 2.33 becomes

$$k_c(C_0) = \frac{1}{2}\left(1 - 2\gamma - 4C_0 \pm \sqrt{8(2\gamma - 3) + (-1 + 4C_0 + 2\gamma)^2}\right)^{1/2}, \quad (2.35)$$

with effective surface tension $\gamma = 1/2C_0^2$.

The critical wavenumber at $\gamma_0 = 0$ is plotted in detail in Figure 2.5. While there are two real solutions $k_c(C_0)$ to Equation 2.32 for intrinsic curvatures between $C_0 = -\sqrt{3}$ to $C_0 = -1$, all systems with wavelengths longer than that indicated by the larger critical wavenumber should be counted as unstable because these long-wavelength systems experience shape perturbations of all smaller wavelengths. Note that even in the absence of an intrinsic interfacial tension, a function of spontaneous curvature, $\gamma := \frac{C_0^2}{2}$, acts as an effective surface tension [35]. At extreme spontaneous curvature of either sign, this term dominates and the system approaches the original Plateau-Rayleigh stability criterion, $k_c = 1$.
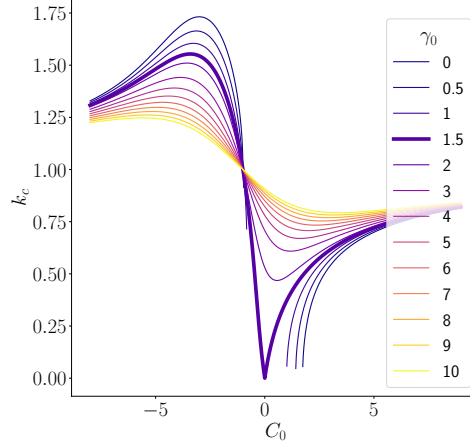
Figure 2.6: $k_c(C_0)$ at a range of γ_0

As is conventional [6], orientation of the surface was defined so that the original cylinder has the negative total curvature $2H = -\frac{1}{r_0} = -1$. Surprisingly, a preferred curvature with the same sign as that of the initial cylinder has a more prominent destabilizing effect than a preferred curvature opposite to that of the initial cylinder. The maximum critical wavenumber $k_c = \sqrt{3}$ occurs at $C_0 = -3$. At this spontaneous curvature, the sphere-like sections of a heavily modulated cylinder most closely approximate the material's preferred curvature value.

2.4.3 Competing surface tension and spontaneous curvature

In systems with competing intrinsic surface tension and bending rigidity effects, the full Equation 2.33 is relevant. The limiting wavenumbers are plotted as a function of spontaneous curvature for a range of intrinsic surface tension in Figure 2.6. As identified in Section 2.4.1, a surface tension of $\gamma_0 = 1.5$ (in units of κ) delineates systems where bending rigidity effects create a region of absolute stability. In the limit of large surface tensions dominating over any spontaneous curvature effects, the critical wavenumber approaches $k_c = 1$ at all spontaneous curvature values.

2.5 Numerical stability analysis

I also semi-numerically integrate equation 2.30, which is explicitly written as

$$\mathcal{H}_E = \mathcal{H}_E^{surf} + \mathcal{H}_E^{curv}$$

$$\mathcal{H}_E^{surf} = 2\pi\gamma \int_0^{2\pi/k} dz \frac{r_0}{\sqrt{1 - \frac{a^2}{2}}} (1 + a\sin(kz))\sqrt{1 + a^2 k^2 r(a)^2 \cos^2 kz}$$

$$\mathcal{H}_E^{curv} = 2\pi\frac{\kappa}{2} \int_0^{2\pi/k} dz \frac{\sqrt{1 + \frac{a^2}{2}}}{r_0(1 + a\sin(kz))\sqrt{1 + a^2 k^2 r_0^2 \cos(kz)}}$$

$$+ 2\pi\frac{\kappa}{2} \int_0^{2\pi/k} dz \frac{(r_0 a k^2 \sin(kz))^2 r_0(1 + a\sin(kz))}{\left(1 + \frac{a^2}{2}\right)^{3/2}(1 + a^2 k^2 \cos^2(kz))^{5/2}}$$

$$+ 2\pi\frac{\kappa}{2}4C_0 \int_0^{2\pi/k} dz$$

$$+ 2\pi\frac{\kappa}{2}4C_0 \int_0^{2\pi/k} dz \frac{a k^2 r_0^2 \sin(kz)(1 + a\sin(kz))}{(1 + \frac{a^2}{2})(1 + r_0^2 a^2 k^2 \cos^2(kz))}.$$

(2.36)

The values of complete elliptic integrals of the second kind, $E(m) := \int dz\sqrt{1 + m^2}$, are used where applicable and the remaining intractable terms are integrated numerically. By repeating the integration for a range of values $0 < |a| < 1$, I numerically identify minima of the potential $\mathcal{H}_E(a)$. For a grid of values of (k, γ_0) and (k, C_0) respectively, the minimizing shape amplitude $|a|$ is shown as the background shading in Figure 2.7 and 2.8. The analysis goes beyond first order energy differences around $a \approx 0$, and so is applicable to systems with greater shape amplitudes.

2.5.1 Metastability

In general the numerical results replicate the perturbatively predicted stability criterion well. However, there is a discrepancy in perturbative and numerical predictions around $\kappa = 0$, $k = 1$: around the classical Plateau-Rayleigh instability for surface-tension dominated systems.

To interpret the discrepancy, I examine the one-dimensional energy landscape $\mathcal{H}_E^{surf}(a)$ at values around $k = k_c = 1$ (Figure 2.9). In these cases, linear
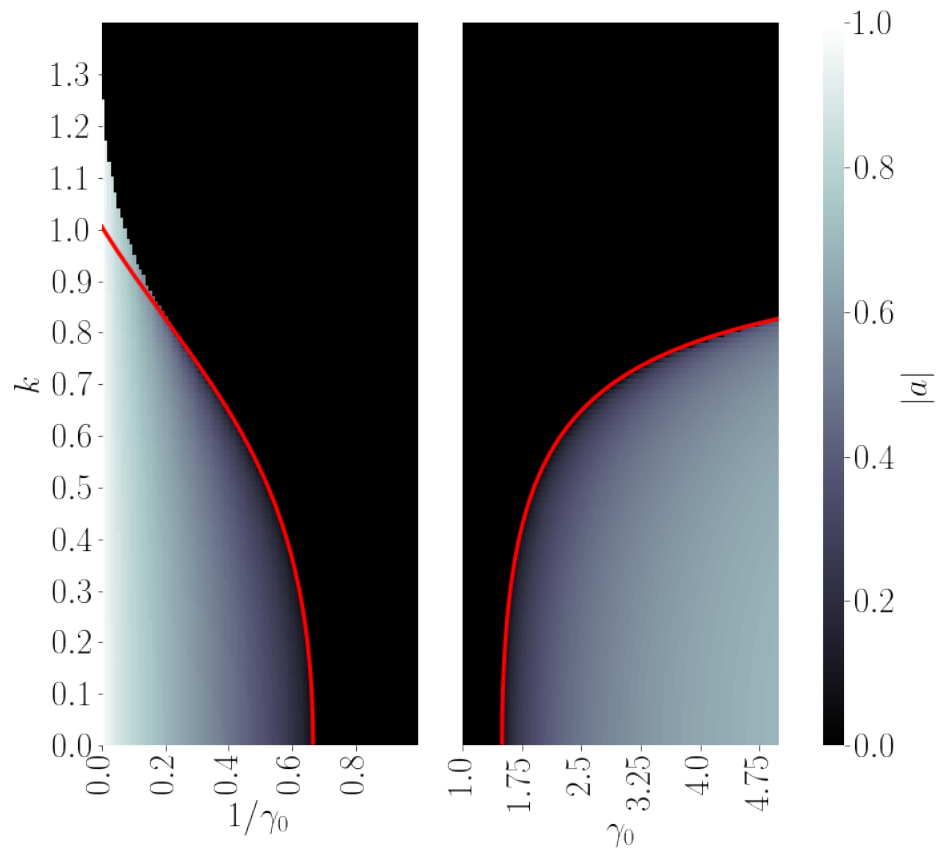
Figure 2.7: Linear and numerical stability at neutral spontaneous total curvature $C_0 = 0$. The red line shows the result of linear stability analysis, delineating linearly stable from unstable regions as in Figure 2.4. The background shading gives the energy-minimizing shape amplitude $|a|$ according to numerical analysis. There is a region of metastability, where the system is modulated according to numerical analysis but stable according to linear analysis, around $1/\gamma_0$, $k \gtrsim 1$.
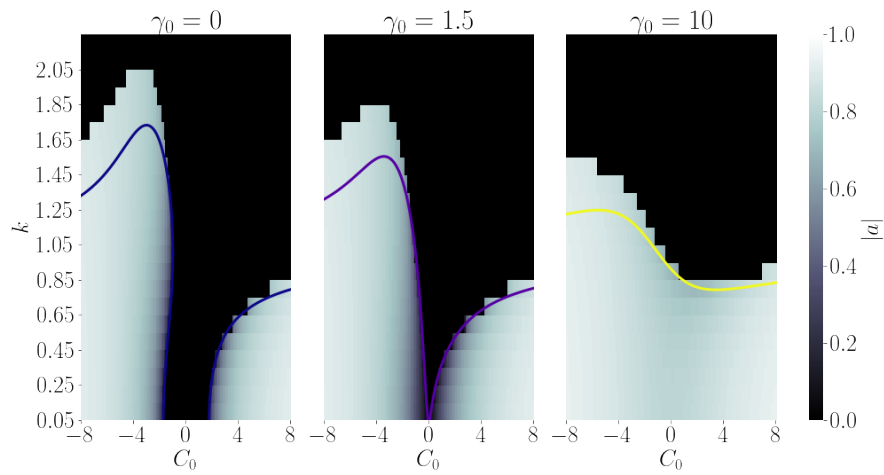
Figure 2.8: Linear and numerical stability for varying C_0 at three fixed γ_0. Colored lines taken from linear stability analysis, Figure 2.6. The background shading gives the energy-minimizing shape amplitude $|a|$ according to numerical analysis for a given set of values (k, C_0). There are a metastability regions especially at negative spontaneous curvature values, where numerical analysis indicates $|a| \gg 0$ above the linear stability line.

stability analysis correctly identified $|a| = 0$ as a local minimum. However, there are more significant global minima at $|a| = 1$. These are detected by the numerical minimization analysis. The system is metastable: the flat cylinder is stable against small fluctuations, but larger fluctuations will induce a transition to the global minimum at $|a| = 1$, interpreted as breakup into droplets. The phenomenon has already been noted by Carter and Glaeser [44] in the context of instability of wires and cylindrical metal inclusions; they point out the amplitude-dependent ('nucleation barrier') stability criterion is $k_c(a) = \sqrt{1 + \frac{a^2}{2}}$ (in units of $1/r_0$) . In general, predictions from linear stability analysis are similar to those from numeric minimization.

In Figure 2.8, we see that the metastability effect is greater at negative spontaneous curvatures, whose linearly destabilizing effect is also greater than that of positive spontaneous curvatures, as has been discussed previously. At negative spontaneous curvature, a highly modulated shape, that is approaching spheres with the preferred curvature everywhere, is the energetic minimum of the system. The strong metastability reflects in a region around $C_0 \approx -3$ reflects this nearby strong energetic minimum.

2.5.2 Stability of modulated tubules

The numerically retrieved energy-minimizing values $|a|$ in Figures 2.7 and 2.8 can take on intermediate values $0 < |a| < 1$. That is, for wavenumber and surface tension combinations where the cylinder is unstable (minimizing shape amplitude a_{min} is not zero), the minimizing shape amplitude is not always $|a_{min}| = 1$. A stable modulated morphology is predicted. I here examine whether this prediction can be taken literally, despite the system being artificially restricted to the family of sinusoidally perturbed shapes.

One major approximation in the analysis is that only a single sinusoidal modulation of wavenumber k, which may be seen as the longest wavelength a system can support, is considered. This is in contrast to solving the full axisymmetric shape equations, i.e. solving for the functional $r(z)$ minimizing system energy $\mathcal{H}_E[r(z)]$. The simplification has allowed me to reduce the problem to a simple single-parameter minimization. Equivalently, the exact shape $r(z)$ of the system can be fully decomposed into sinusoids, of which we have examined only
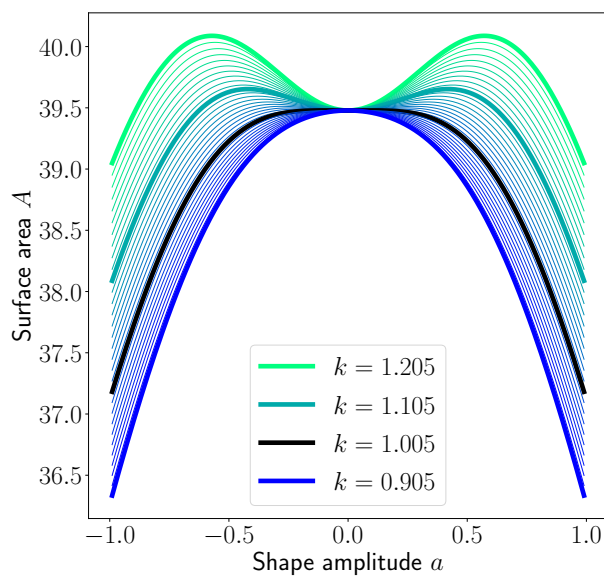
Figure 2.9: Surface area of modulated cylinders with a range of wavenumbers k around $k = 1$. The illustration shows how the numerically detected global minima and a stability analysis around $a = 0$ can give apparently contradictory outcomes. Maxima are marked to show that, just above $k = 1$, the local minimum at $a = 0$ is separated from the collapsed state by very low energy barriers and thus for practical purposes the shape is unstable at some $k > 1$ at nonzero temperatures.
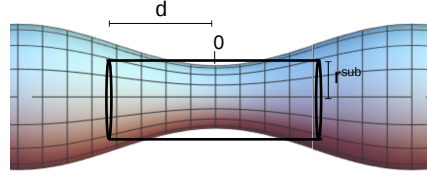
Figure 2.10: Approximating the neck as a cylinder.

the longest-wavelength one, thought to be the primary indicator of stability. In reality, fluctuations of all wavelengths smaller and up to the length of the system exist simultaneously. Instability against fluctuations of any such wavelength indicates overall instability of the system. I here refine the initial estimate by considering the addition of smaller-wavelength fluctuations on crucial sections of the system.

I here estimate whether the predicted modulated morphology is stable against smaller-wavelength perturbations on the resulting narrow neck by considering the narrow neck as a subsystem which can be subjected to the same analysis as the parent system. A subsystem centered on the narrowest point is approximated as an initially straight cylinder of length $2d$, where d may range from 0 to $\pi/2$ (Figure 2.10), and with its radius approximated by its mean radius

$$r^{sub} = \langle r \rangle = \frac{2\int_0^d r(a)\,(1 - a\cos(kz))\,dz}{2d}$$
$$= r(a)(1 - a/d\sin(kz)). \tag{2.37}$$

In this approximation, initial curvature of the subsystem is also neglected. The pre-existing slight axial curvature would stabilize the subsystem relative to my estimate. Finally the narrow neck is assumed to obey the same analysis as the larger system, with a volume constraint on subsystem volume.

I find the subsystem's critical wavenumber, $k_c^{sub}(d)$, by applying Equation 2.33 to the subsystem. By absorbing factors of r^{sub} into κ, the subsystem can be seen as a similar system with larger effective bending rigidity $\kappa' = \kappa/(r^{sub}(a))^2$, and smaller relative surface tension $\gamma^{sub} = \gamma(r^{sub}(a))^2$. Effective spontaneous curvature is, in units of the subsystem radius, scaled to $C_0' = C_0 r^{sub}$.

Starting from a system with k, C_0, and the shape amplitude a indicated by the numerical analysis in section 2.5, I check numerically whether, for any $d \in (0, \pi/2)$, there exists a subsystem of length $2d$ whose aspect ratio is smaller than its critical aspect ratio $k_c^{sub}(d)/r_0$.

Where such a linearly unstable subsystem exists, this does not necessarily indicate the modulated cylinder will breakup: the linearly unstable narrow neck may develop a large-amplitude fluctuation which leads to pinch-off or the subsystem may itself develop to only a mildly modulated shape, which is not itself linearly unstable to any smaller wavelengths. On the other hand, where no linear instability of the narrow neck is found (cases indicated by the hatched area on Figure 2.11), the mildly modulated channel shape indicated by the numerical analysis is indeed a stable equilibrium. The first iteration of the recursive stability analysis scheme indicates that at least some such stable modulated channels exist. The exact extent of the phenomenon is likely underestimated by only including absolutely stable cases, and the scheme is a rough estimate where approximations, for example the choice to take mean radius as the effective radius, were made. Like the identification of a metastability phenomenon, the novel analysis highlights another limitation of the linear stability prediction.

2.6 Discussion and Conclusions

I review the static energy balance approach to the instability of fluid columns with surface tension (the Plateau-Rayleigh instability) as well as those with some combination of surface tension, bending rigidity, and nonzero spontaneous curvature. Various combinations of surface tension, bending rigidity, and spontaneous curvature are examined analytically using perturbative stability analysis. By numerical analysis beyond small shape amplitudes, I find a metastability phenomenon, where some linearly stable cases are in fact unstable against larger fluctuations. I also find that some apparently unstable systems may in fact reach equilibrium in a stable, mildly modulated channel shape. Expressions for linear limits of stability of such systems are well known in the literature; they are re-derived here as a basis and comparison. I add the suggestion that the energy landscape beyond the linear regime, which I explore numerically, gives rise to

(a) Varying γ_0, $C_0 = 0$

(b) Varying C_0, $\gamma_0 = 0$
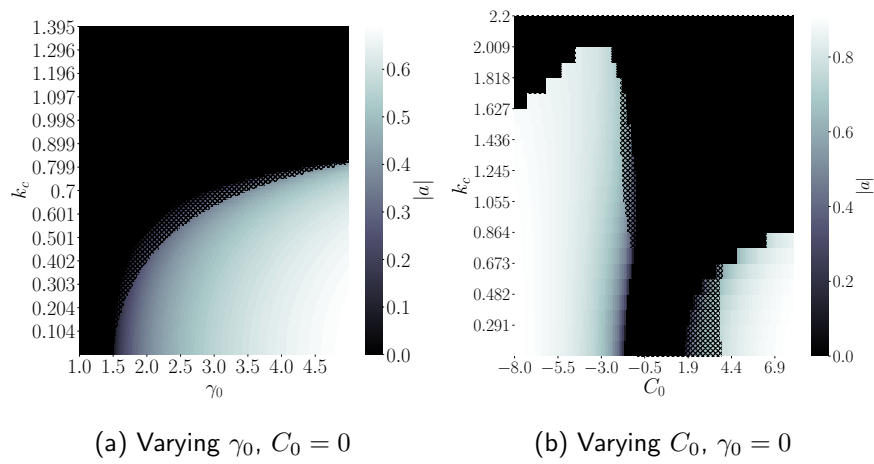
Figure 2.11: Where an intermediate value $0 < |a| < 1$ is indicated as the equilibrium shape amplitude, the stability of the modulated channel shape against smaller-wavelength fluctuations was numerically investigated. The hatched area indicates systems where the resulting modulated morphology is linearly stable against all smaller-wavelength fluctuations. Contrary to the linear prediction, such systems can be considered stable.

physically relevant effects in the case of solid-stabilized interfaces. The chapter sets up the approach - comparing the energetics of equilibrium configurations; linear perturbative and numerical nonperturbative analysis - which I will build on throughout the thesis.

As can be seen in the body of experimental and theoretical literature on tweezed lipid membrane tubes [29, 30, 41, 45], it is possible to induce the relevant surface tension scales in lipid membranes with bending rigidity dynamically. Highly modulated channel shapes which nevertheless do not separate into droplets are observed, but this is not necessarily the effect predicted in Section 2.5.2. Granek and Olami [42] suggest that the modulated shape is not accounted for in the simple model with uniform material properties, but is some additional effect such as dynamic fractionation of lipid molecules by spontaneous curvature, where a mixture of two or more lipid species varies in compositions according to emerging surface curvatures.

An arbitrary choice was made to retain an energy density from spontaneous curvature, as an effective surface tension in $\gamma = \gamma_0 + \frac{C_0^2}{2}$ as well as to reserve a symbol γ_0 for miscellaneous 'other' energy densities of the interfacial material. These energy densities are relative to a reference system, in particular to molecules in the bulk. The reservoir is arbitrarily assumed to have been in equilibrium with a version of the system with neutral spontaneous curvature. In reality the appropriate chemical potential or energy density of the interfacial material depends on circumstances of the experiment. Granek, Nelson *et al.* [35, 45] find a destabilizing effective surface tension from spontaneous curvature appropriate for an experiment where a spontaneous curvature is introduced in a lipid tubule by the addition of solutes to the outer liquid.

In my bending rigidity term, potential anisotropic properties of the interfacial material have been omitted. They may play a role in technical and biological lipid membrane system, for example when a spontaneous mean curvature is induced by arc-shaped proteins [46]. A spontaneous mean curvature term could be added to the model to study additional effects.

Only sinusoidal axisymmetric shape deformations of a cylinder are examined, omitting the possibility of azimuthal modes as well as other shapes. Nevertheless, the system approximates possibly irregular channels in emulsions, as general

principles are similar. The shape of a pearled membrane tube is likely a unduloid, an axisymmetric minimal surface. However, it closely resembles a sinusoid. More angular and faceted shapes become a likely outcome in later chapters, but will not be accurately represented by the shape deformations examined here.

The system is said to be a closed infinite or periodic tube (a 'straight torus'), a clearly unphysical object. The enclosed fluid volume (per periodic section) is assumed to be constant on this basis. The real object of interest, a channel or tubule attached to constant-pressure droplet reservoirs or a larger structure, is subject to equivalent effects. The topological genus (and thus integral over Gaussian curvature) is said to be constant if the tubule is periodic. Shape changes in which topological genus is changed, such as breakup into spheres, are also excluded from the model except as the implied consequence of high-amplitude deformations.

Furthermore the mechanical model described by the Helfrich Hamiltonian is a simplified one, assuming spatially homogeneous properties of the interfacial material. In-plane stresses and flows are omitted. While in some systems the interfacial layer may be relatively homogeneous, in others, effects such as the fractionation of lipid species by curvature occur. As a consequence, there is spatial variation in the material properties of the interface. One example of a spatially varying property of the interfacial material, orientational order, is the subject of the rest of this thesis. The formulation will be additive, retaining the material properties described in this chapter as a background of spatially uniform 'external' terms in the energy while adding complex additional effects.

Bibliography

[1] L. Rayleigh, Proc London Math So **s1-10**, 4 (1878).

[2] S. Chandrasekhar, *Hydrodynamic and Hydromagnetic Stability*Dover Books on Physics (Dover Publications, Mineola, NY, 1981).

[3] F. Gallaire and P.-T. Brun, Philos Trans R Soc A **375**, 20160155 (2017).

[4] K. Stratford, R. Adhikari, I. Pagonabarraga, J.-C. Desplat, and M. E. Cates, Science **309**, 2198 (2005).

[5] N. Mermin and T.-L. Ho, Phys Rev Lett **36**, 594 (1976).

[6] R. D. Kamien, Rev Mod Phys **74**, 953 (2002).

[7] E. W. Weisstein, Christoffel Symbol of the Second Kind. From MathWorld—A Wolfram Web Resource, Last visited on 17/5/2022.

[8] J. Plateau, Ann Phys (Leipzig) **158**, 387 (1851).

[9] S. A. Safran, *Statistical thermodynamics of surfaces, interfaces, and membranes* (CRC Press, 2018).

[10] L. D. Landau and E. M. Lifshitz, *Fluid Mechanics*, Course of Theoretical Physics Vol. 6, 2 ed. (Pergamon Press, 1987).

[11] P. Lenz and D. R. Nelson, Phys Rev Lett **87**, 125703 (2001).

[12] N. Vargaftik, B. Volkov, and L. Voljak, J Phys Chem Ref Data **12**, 817 (1983).

[13] F. Sedlmeier, D. Horinek, and R. R. Netz, Phys Rev Lett **103**, 136102 (2009).

[14] S. N. Sahasrabudhe, V. Rodriguez-Martinez, M. O'Meara, and B. E. Farkas, Int J Food Prop **20**, 1965 (2017).

[15] L. Fisher, E. Mitchell, and N. Parker, J Food Sci **50**, 1201 (1985).

[16] A. Goebel and K. Lunkenheimer, Langmuir **13**, 369 (1997).

[17] H. Kim and D. J. Burgess, J Colloid Interface Sci **241**, 509 (2001).

[18] R. Aveyard, B. P. Binks, S. Clark, and J. Mead, J Chem Soc Faraday Trans **82**, 125 (1986).

[19] C. A. Grattoni, R. A. Dawe, C. Y. Seah, and J. D. Gray, J Chem Eng Data **38**, 516 (1993).

[20] G. Rämme, Phys Educ **32**, 191 (1997).

[21] B. Binks, H. Kellay, and J. Meunier, EPL **16**, 53 (1991).

[22] S. Guttman *et al.*, Proc National Acad Sci U S A **113**, 493 (2016).

[23] F. Brochard, P. De Gennes, and P. Pfeuty, J Phys (Paris) **37**, 1099 (1976).

[24] M. Schneider, J. Jenkins, and W. Webb, J Phys (Paris) **45**, 1457 (1984).

[25] C. Morris and U. Homann, J Membr Bio **179**, 79 (2001).

[26] E. Fischer-Friedrich, A. A. Hyman, F. Jülicher, D. J. Müller, and J. Helenius, Sci Rep **4**, 1 (2014).

[27] M. Bloom, E. Evans, and O. G. Mouritsen, Q Rev Biophys **24**, 293 (1991).

[28] H. Duwe, J. Kaes, and E. Sackmann, J Phys (Paris) **51**, 945 (1990).

[29] R. Bar-Ziv and E. Moses, Phys Rev Lett **73**, 1392 (1994).

[30] P. D. Olmsted and F. C. Macintosh, J Phys (Paris) **7**, 139 (1997).

[31] O. Marin, M. Tkachev, E. Sloutskin, and M. Deutsch, Curr Opin Colloid Interface Sci (2020).

[32] D. A. Woods, C. D. Mellor, J. M. Taylor, C. D. Bain, and A. D. Ward, Soft Matter **7**, 2517 (2011).

[33] A. Sahu, A. Glisman, J. Tchoufag, and K. K. Mandadapu, Phys Rev E **101**, 052401 (2020).

[34] K. White, A. B. Schofield, B. Binks, and P. Clegg, J Phys Condens Matter **20**, 494223 (2008).

[35] R. Granek, Langmuir **12**, 5022 (1996).

[36] S. Chaïeb and S. Rica, Phys Rev E **58**, 7733 (1998).

[37] A. Mahapatra, C. Uysalel, and P. Rangamani, J Membr Bio **254**, 273 (2021).

[38] J. Hu *et al.*, Science **319**, 1247 (2008).

[39] W. Helfrich, Z Naturforsch C **28**, 693 (1973).

[40] F. Campelo, C. Arnarez, S. J. Marrink, and M. M. Kozlov, Adv Col Interf Sci **208**, 25 (2014).

[41] G. Boedec, M. Jaeger, and M. Leonetti, J Fluid Mech **743**, 262 (2014).

[42] R. Granek and Z. Olami, J Phys (Paris) **5**, 1349 (1995).

[43] K. L. Gurin, V. V. Lebedev, and A. R. Muratov, Zh Eksp Teor Fiz [Sov Phys - JETP] **110**, 600 (1996).

[44] W. Carter and A. Glaeser, Mater Sci and Eng **89**, L41 (1987).

[45] P. Nelson, T. Powers, and U. Seifert, Phys Rev Lett (1995).

[46] V. Kralj-Iglič, A. Iglič, H. Hägerstrand, and P. Peterlin, Phys Rev E **61**, 4230 (2000).

CHAPTER 3

Landau-Ginzburg model of orientational order

Abstract

I introduce the Landau-Ginzburg theory of a curvature-coupled orientational order parameter field and derive analytic outcomes on the modulated channel shape in a range of cases. I first examine the corresponding Fourier-space theory of the quadratic operator Γ. For small shape perturbations, the interfacial material remains ordered; orientational order resists splay-inducing curvatures and the effect on a cylindrical system is stabilizing. On more strongly modulated channel shapes, I predict two distinct types of response of the orientational order. I distinguish type I systems, where only the magnitude of order varies in response to curvature, and a type II vortex state, where the orientation of order rotates around up to $4n$ defect cores.

Table 3.1: Table of symbols, Chapter 3

symbol	meaning
ϕ	angle of individual particles or bonds
a	shape amplitude of sinusoidally modulated surface
r_0	the radius of the unperturbed cylinder
γ	surface tension
κ	bending rigidity
$r(a)$	mean radius of the perturbed cylinder with conserved volume
$r = r(z, a)$	radius of the perturbed cylinder
A_i	spin connection, a local geometric quantity of the surface
n	order of rotational symmetry
α, c, u	phenomenological parameter in the LG theory
∂_i	partial derivative operator
D_i	covariant partial derivative operator
$\Psi, \ \Psi(\mathbf{x})$	order parameter field, a complex-valued field over the surface space
$\psi(z)$	a simplified, real and one dimensional, representation of the field
$\Psi_{\mathbf{q}}$	(component of the) Fourier space representation of the field
ψ_j	Fourier space representation real and one-dimensional field
$\Gamma_{\mathbf{qq'}}$	Fourier-space operator of the quadratic part of the Hamiltonian, a Hermitian matrix
$D_{\mathbf{qpq'p'}}$	Fourier-space operator of the quartic part of the Hamiltonian, a high-dimensional matrix
$\mathbf{q} = (j, \beta)$	wavevector; axial and azimuthal direction wavenumbers
g_i	Fourier basis
f_i	basis of eigenfunctions on the modulated cylinder
m	local azimuthal rotation number
M	number of defects
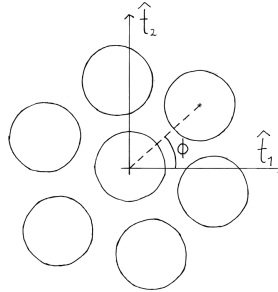
Figure 3.1: Definition of the angle ϕ in hexatic order: a 'bond' is drawn between a molecule or particle position and one of its neighbours. The angle ϕ is the angle between the intrinsic basis vector $\hat{t}_1$ and the bond. Any of the six neighbours can be chosen.

3.1 Introduction

In this chapter I examine an orientationally ordered fluid, such as a fluid of molecules or particles on the interfaces in emulsions, and its interactions with a curved surface. I examine how surface shape affects order in the material and how order affects shape and stability of a modulated channel.

As motivated in Section 1.2, monolayers of monodisperse spherical particles form a low-temperature hexatic phase, where particles are locally arranged in hexagonal configurations. The orientation of the hexagonal pattern persists over long distances. Another example of orientational order is order in the orientations of elongated molecules or particles in a nematic material. Various types of orientational order can be represented as the complex-valued order parameter field $\Psi(\mathbf{x})$, enabling a unified theoretical treatment.

The order parameter field is here constructed as

$$\Psi(\mathbf{x}) = \langle e^{in\phi(\mathbf{x})}\rangle. \tag{3.1}$$

The brackets $\langle \rangle$ denote a local spatial averaging over a certain lengthscale Λ, which should be chosen to encompass a few molecular/particle bonds while not being so big that the spatial average approaches zero. For each bond, the angle ϕ is defined as the angle between one of the basis vectors $\hat{t}_i$ of the local

coordinate system (Equation 2.3) and the 'bond' connecting a particle and its neighbour (Figure 3.1). This angle in the $\hat{t}_1, \hat{t}_2$ tangent plane is then mapped onto the phase of a complex number. The factor n for the multiplicity of the n-atic order, for example n=1,2,3,4,or 6, is introduced. For hexatic symmetry, $n = 6$. This factor ensures that Ψ has the same phase if any of the six 'bonds' are chosen as a reference by which ϕ is measured.

The internal Hamiltonian is the part of the Hamiltonian collecting terms relating to the energy associated with the arrangement of molecules or particles within the surface. This part of the Hamiltonian is a functional of the order parameter field $\Psi(\mathbf{x})$. An expression $\mathcal{H}_I(|\Psi|^2, |D_i\Psi|^2, |\Psi|^4, ...)$ is chosen according to Landau-Ginzburg theory. As usual, this derives from minimal assumptions of analyticity and symmetry of the energy functional [1]. In particular, symmetry under $\Psi \to -\Psi$ means that only even powers of Ψ and its derivatives are included. I here use

$$\mathcal{H}_I = \int_S dS \left(\alpha|\Psi|^2 + c|D_i\Psi|^2 + \frac{u}{2}|\Psi|^4 \right) \tag{3.2}$$

with $dS = \sqrt{g}dzd\theta$.

The notation $|\cdot|^2$ applied to a complex scalar indicates the usual square modulus, $|x|^2 = xx^*$. The same square modulus notation applied to a complex tensor indicates a tensor inner product as well as the complex absolute square, $|x_i|^2 := x_i x^{i*} = x_i x_j^* \eta^{ij}$, here using the metric η_{ij} of the cylindrical coordinate system.

The coefficients c and u are positive real numbers, and α is a real coefficient that may be positive of negative. The coefficients are in general functions of temperature and other variables, but the value of the first coefficient as a function of temperature is most critical to the phase behaviour of the order parameter field. The simplest expression near the critical point is a linear function

$$\alpha(T) = \alpha_0 \frac{T - T_c}{T_c}, \tag{3.3}$$

where T_c is the usual critical temperature of the material on a flat space.

The second coefficient, c, is a bending rigidity of the order parameter field. It is related to the Frank constant, which describes the bending rigidity of liquid crystals, in the one-Frank-constant approximation. The Frank constant

K is the coefficient to a gradient term $1/2((\nabla \cdot \hat{n})^2 + |\nabla \times \hat{n}|^2)$, where order is described as a vector field $\hat{n}$. According to the KTHNY theory of hexatic phases [2], the theoretical value of the Frank constant is $K = 72/\pi$ (in energy units $k_B T$) near the isotropic-hexatic transition, while in the low-temperature limit of the hexatic phase it diverges towards a hexatic-crystalline transition. For hexatic phases in monolayers of spherical colloidal particles, this constant has been experimentally measured and was found to be in good agreement with the theoretical prediction [3, 4]. Note that the value $K_a = 72/\pi$ is given in the framework of a different notational convention for orientational order in the hexatic material, where average bond orientation is included as a vector field rather then being mapped onto a 'spin n' complex field. A value of $K = 72/\pi = 2n^2/\pi$ in the literature corresponds to a value of $c = 1/\pi$ in my model, where an equivalent factor of n^2 is instead included in $|D_i \Psi|$.

The derivative term $c|D_i \Psi|^2$ can be interpreted as the energy cost of distorting the field $\Psi(\mathbf{x})$. The operator D_i is the covariant derivative operator, defined as

$$D_i = \partial_i - in A_i, \tag{3.4}$$

where A_i is the spin connection (Equation 2.11), a quantity relating to surface shape at each point. The use of the spin connection to construct the covariant derivative accounts for the difference between a parallel vector field as defined naively by the derivative and as produced by transport along a curved surface. It is via this term that the interaction of surface curvature with the order parameter field is taken into account. In the limit of a flat surface, $A_i = 0$ and the operator reduces to the conventional gradient of the order parameter field.

The Landau-Ginzburg model for n-atic order of membranes on curved interfaces has been introduced for spheres by Park et $al.$ [5] and studied on spheres and tori by Evans [6, 7]. For a summary of further developments in the study of Landau-Ginzburg n-atic order and of other representations of order on a variety of surface shapes, see review by Bowick and Giomi [8].

On a flat space and in the absence of thermal fluctuations, well-known solutions minimizing the Landau theory, i.e. Equation 3.2 without the gradient

term, are obtained by solving

$$\frac{\partial \mathcal{H}_I}{\partial \Psi^*} = \Psi_0(\alpha + u|\Psi_0|^2) = 0; \tag{3.5}$$

solutions are complex values Ψ_0 with arbitrary phase and with magnitude

$$|\Psi_0| = \begin{cases} \sqrt{\frac{-\alpha}{u}}, & \alpha \leq 0, \\ 0, & \alpha > 0. \end{cases} \tag{3.6}$$

Note that in this state the material has an energy density per unit area of

$$v_0 = \begin{cases} -\frac{\alpha^2}{2u}, & \alpha \leq 0, \\ 0, & \alpha > 0. \end{cases} \tag{3.7}$$

The negative free energy density of the ordered interface (relative to surfactants in the bulk) at low temperatures can act as an effective negative surface tension. A temporarily negative effective surface tension in combination with hexatic ordering of molecules on macroscopic droplets can have dramatic experimentally observed effect on spherical droplets, [9–11].

The material has a persistence length [1] of

$$\xi = \begin{cases} \sqrt{\frac{c}{2|\alpha|}}, & \alpha \leq 0, \\ \sqrt{\frac{c}{\alpha}}, & \alpha > 0. \end{cases} \tag{3.8}$$

It is common to use the London approximation in place of Equation 3.2, assuming that a constant-magnitude field $|\Psi| = |\Psi_0| = 1$ exists almost everywhere on the surface. Topological point defects are treated as discrete defect charges, but the local decrease in field magnitude at the defect core is neglected. The treatment allows elegant differential geometry solutions, for example by Alageshan *et al.* [12] on general shapes. In this view coupled with dynamic Plateau-Rayleigh instability, Lenz and Nelson [13] have treated instabilities of a cylindrical system with bending rigidity and n-atic order. The London approximation is appropriate for the low temperature ($\alpha < 0$) regime [14]. I here choose to retain the general theory, allowing the magnitude of $\Psi(\mathbf{x})$ to vary, with the quadratic-quartic potential loosely confining the field close to magnitude given in Equation 3.6. This additional information comes at the cost of analytic tractability but enables us to discover a high-temperature-like effect of curvature in simulation.

In general we seek solutions $\Psi(\mathbf{x})$ to Equation 3.2 with expressions D_i, $\sqrt{g}$ specific to the surface shape.

3.2 Fourier space field theory

The standard approach to wave equations in general is to examine the theory in Fourier space, as Fourier modes are eigenmodes of the Laplacian operator and the problem usually becomes linearly separable. I find that this does not apply on the modulated surface shape and the use of Fourier analysis is limited. Other insights are gained from the Fourier-space examination.

The field is decomposed as Fourier series

$$\Psi(\mathbf{x}) = \sum \Psi_{\mathbf{q}} e^{i\mathbf{q}\cdot\mathbf{x}'} = \sum \Psi_{\mathbf{q}} e^{\frac{i\theta\beta}{r_0}} e^{ikzj} \tag{3.9}$$

with scaled position vector $\mathbf{x}' = (\theta/r_0, zk)$ and with wavevector $\mathbf{q} = (\beta, j)$ ranging over both positive and negative integer values of β and j. The field $\Psi(\mathbf{x})$ is defined with respect to the external, cylindrical coordinate basis (θ, z); the decomposition is general to a field on any deformation of a cylindrical surface. The space is periodic, therefore the continuous field $\Psi(\mathbf{x})$ transforms into a discrete set of coefficients $\Psi_{\mathbf{q}}$ for $q_z, q_\theta = 0, \pm 1, \pm 2, ...,$ up to some cutoff wavenumber $|\mathbf{q}| = Q$.

Coefficients $\Psi_{\mathbf{q}}$ are formally given by the inverse Fourier transform

$$\Psi_{\mathbf{q}} = \frac{1}{A_0} \int_0^{2\pi} \int_0^{2\pi/k} d\theta dz \Psi(\mathbf{x}) e^{-i\beta\theta} e^{-ijkz}. \tag{3.10}$$

The Fourier transform convention is such that the real-space domain (the surface of a cylinder) has dimensions $2\pi r_0 \times 2\pi/k$ and area $A_0 = (2\pi)^2 r_0/k$.

To obtain low-temperature solutions I will be solving for the set of complex values $\{\Psi_{\mathbf{q}}\}$ minimizing $\mathcal{H}_I$. Inserting Equation 3.9 into Equation 3.2, the Hamiltonian can be expressed, in discrete Fourier space, as the sum

$$\mathcal{H}_I = \sum_{\mathbf{q}\mathbf{q}'} \Psi_{\mathbf{q}} \Psi_{\mathbf{q}'}^\dagger \int_S dS \left(\alpha e^{i(\mathbf{q}-\mathbf{q}')\cdot\mathbf{x}'} + c(D_i e^{i\mathbf{q}\mathbf{x}'})(D^i e^{i\mathbf{q}'\mathbf{x}'})^* \right)$$
$$+ \sum_{\mathbf{q}\mathbf{p}\mathbf{q}'\mathbf{p}'} \frac{u}{2} \Psi_{\mathbf{q}} \Psi_{\mathbf{p}} \Psi_{\mathbf{q}'}^\dagger \Psi_{\mathbf{p}'}^\dagger \int_S dS e^{i(\mathbf{q}+\mathbf{p}-\mathbf{q}'-\mathbf{p}')\cdot\mathbf{x}}, \tag{3.11}$$

or

$$\mathcal{H}_I = \sum_{\mathbf{q}\mathbf{q}'} \Psi_{\mathbf{q}} \Psi_{\mathbf{q}'}^\dagger \Gamma_{\mathbf{q}\mathbf{q}'} + \sum_{\mathbf{q}\mathbf{p}\mathbf{q}'\mathbf{p}} \Psi_{\mathbf{q}} \Psi_{\mathbf{p}} \Psi_{\mathbf{q}'}^\dagger \Psi_{\mathbf{p}'}^\dagger D_{\mathbf{q}\mathbf{p}\mathbf{q}'\mathbf{p}'}, \qquad (3.12)$$

with matrices Γ, D holding values of the integrals in Equation 3.11, evaluated over whole periods of a given surface shape. The matrix $\Gamma = G^{-1}$ of the quadratic part of the series can be identified as a propagator or inverse Green's function. For an unperturbed quadratic theory the propagator is $\Gamma_0 = diag(\alpha + c/r^2|q|^2)$. For flat space the operator/matrix Γ_0 is diagonal and the matrix D_0 is 'diagonal' in the sense that $D_{\mathbf{q}\mathbf{p}\mathbf{q}'\mathbf{p}'} \sim \delta_{(\mathbf{q}+\mathbf{p})(\mathbf{q}'+\mathbf{p}')}$.

The standard procedure for a quadratic-quartic field theory is that the quadratic operator is diagonal; the partition function related to the harmonic operator is trivial. The quartic part of the theory can then be added as a perturbation. However, on the curved surface the quadratic operator itself is not trivial. I therefore devote time to examining the quadratic operator. In the case of small surface shape modulations $|a| \ll 1$, effects of curvature on the quadratic part of the theory can be introduced perturbatively.

3.2.1   Quadratic operator

Let's find expressions for the off-diagonal values and the resulting low-temperature field on the slightly perturbed surface. Proceeding first with the harmonic part of the theory,

$$\mathcal{H}_I = \sum_{\mathbf{q}\mathbf{q}'} \psi_{\mathbf{q}'}^\dagger \Gamma_{\mathbf{q}\mathbf{q}'} \psi_{\mathbf{q}}. \qquad (3.13)$$

The operator $\Gamma_{\mathbf{q}\mathbf{q}'}$ is a Hermitian matrix, albeit an infinitely large one with indices running to $\pm\infty$ in both directions. The basis is the Hilbert space of Fourier modes $g_{\mathbf{q}} = e^{i\mathbf{q}\cdot\mathbf{x}}$. The wavevector indices $\mathbf{q} = (j, \beta)$ and $\mathbf{q}' = (j', \beta')$ stand for two wavenumber indices each; the matrix $\Gamma_{\mathbf{q}\mathbf{q}'}$ can alternatively be thought of as the four-dimensional object $\Gamma_{j\beta j'\beta'}$. However, even on the modulated shape $\Gamma_{j\beta j'\beta'} \sim \delta_{\beta\beta'}$. The operator is 'diagonal' in β indices; modes with different θ-direction momenta do not interact with each other. For each value β, there is a set of solutions $\Psi_{j\beta}, \Psi_{j',\beta}^\dagger$ which are uncoupled from and analogous to the set of solutions for any other value of β. It is sufficient to fix $\beta = \beta'$ to an arbitrary value, for example $\beta = 0$, and examine one such set of solutions. Without loss of generality I therefore drop the notation of β

indices and print a two-dimensional 'slice' $\Gamma_{jj'} := \Gamma_{j\beta j'\beta}$ of the four-dimensional operator. On a flat cylinder the operator is also diagonal in j-indices,

$$
\Gamma_{jj'}^{(0)} = A_0
\begin{bmatrix}
\ddots \\
& \alpha + 4cn^2 & 0 & 0 & 0 & 0 \\
& 0 & \alpha + cn^2 & 0 & 0 & 0 \\
& 0 & 0 & \alpha & 0 & 0 \\
& 0 & 0 & 0 & \alpha + cn^2 & 0 \\
& 0 & 0 & 0 & 0 & \alpha + 4cn^2 \\
& & & & & & \ddots
\end{bmatrix}, \quad (3.14)
$$

where the central row and column correspond to indices $j = 0, j' = 0$.

To obtain Γ on modulated surfaces, I evaluate the defining integrals

$$
\Gamma_{\mathbf{qq'}} = \int \int dz d\theta \sqrt{g} \left(\alpha e^{i(\mathbf{q}-\mathbf{q'})\cdot\mathbf{x}} + c(D_i e^{i\mathbf{qx}})(D^i e^{i\mathbf{q'x}})^* \right) \quad (3.15)
$$

I label four terms in this integral

$$
\begin{aligned}
\Gamma_\alpha &= \alpha \int \int d\theta dz \sqrt{g} e^{i(\beta-\beta')\theta} e^{i(j-j')kz}, \\
\Gamma_{c1} &= c \int \int d\theta dz \frac{\sqrt{g}}{g_{\theta\theta}} (jj' + \beta\beta') e^{i(\beta-\beta')\theta} e^{i(j-j')kz}, \\
\Gamma_{c2} &= cn \int \int_0^{2\pi} dz d\theta \frac{\sqrt{g}}{g_{\theta\theta}} (\beta - \beta') A_\theta e^{i(\beta+\beta')\theta} e^{i(j-j')kz}, \\
\Gamma_{c3} &= cn^2 \int \int dz d\theta \frac{\sqrt{g}}{g_{\theta\theta}} A_\theta^2 e^{i(\beta-\beta')\theta} e^{i(j-j')kz}.
\end{aligned}
\quad (3.16)
$$

The matrix $\Gamma_{jj'}$ has the following characteristics: In total, the matrix $\Gamma = \Gamma_\alpha + \Gamma_{c1} + \Gamma_{c2} + \Gamma_{c3}$ is Hermitian. While $\Gamma^{(0)}$ is diagonal, for small shape modulations, the perturbed matrix Γ is weakly non-diagonal. Off-diagonal elements are of order $a^{|j-j'|}$, that is increasingly small for increasingly off-diagonal index pairs.

In the perturbative case for weakly modulated surfaces, I insert series expansions for the quantities $\sqrt{g}$, $1/g_{\theta\theta} = 1/r(a)$, and A_θ in small a and evaluate the integrals up to order a^2. The analytic expressions for values of Equations 3.16 in the perturbative case are:

$$\Gamma_\alpha = \Gamma_\alpha^{(0)} + A_0 \alpha$$

$$\begin{bmatrix} \ddots & & & & & \\ & k^2a^2/4 & ia/2 & -k^2a^2/8 & & \\ & -ia/2 & k^2a^2/4 & ia/2 & -k^2a^2/8 & \\ & -k^2a^2/8 & -ia/2 & k^2a^2/4 & ia^2/2 & -k^2a^2/8 \\ & & -k^2a^2/8 & -ia/2 & k^2a^2/4 & ia/2 \\ & & & -^2k^2a^2/8 & -ia/2 & {}^2k^2a^2/4 \\ & & & & & \ddots \end{bmatrix}, \qquad (3.17)$$

$$\Gamma_{c1} = \Gamma_{c1}^{(0)} + A_0 c \begin{bmatrix} \ddots & & & & & \\ & k^2a^2 & ia & 0 & & \\ & -ia & k^2a^2/4 & 0 & +k^2a^2/8 & \\ & 0 & 0 & 0 & 0 & 0 \\ & k^2a^2/8 & 0 & k^2a^2/4 & ia & \\ & & 0 & -ia & k^2a^2 & \\ & & & & & \ddots \end{bmatrix}, \quad (3.18)$$

$$\Gamma_{c2} = cn^2\pi^2(\beta + \beta') \begin{bmatrix} \ddots & & & & & \\ & 0 & 2a & -ia^2 & 0 & 0 \\ & 2a & 0 & 2a & -ia^2 & 0 \\ & ia^2 & 2a & 0 & 2a & -ia^2 \\ & 0 & ia^2 & 2a & 0 & 2a \\ & 0 & 0 & ia^2 & 2a & 0 \\ & & & & & \ddots \end{bmatrix}, \quad (3.19)$$

$$\Gamma_{c3} = ckn^2\pi^2$$

$$
\begin{bmatrix}
\ddots & & & & & & \\
& ia^3/2 & 2a^2 & -ia^3/2 & a^2 & -ia^3/2 & 0 & 0 \\
& a^2 & ia^3/2 & 2a^2 & -ia^3/2 & a^2 & -ia^3/2 & 0 \\
& ia^3/2 & a^2 & ia^3/2 & 2a^2 & -ia^3/2 & a^2 & -ia^3/2 \\
& 0 & ia^3/2 & a^2 & ia^3/2 & 2a^2 & -ia^3/2 & a^2 \\
& 0 & 0 & ia^3/2 & a^2 & ia^3/2 & 2a^2 & -ia^3/2 \\
& & & & & & & \ddots
\end{bmatrix},
$$

(3.20)

with Equation 3.14 represented as $\Gamma_\alpha^{(0)} = diag(\alpha A_0)$ and $[\Gamma_{c1}^{(0)}]_{jj'} = diag(A_0 j^2 cn^2)$. In the above matrices 0 indicates a value of exactly zero, while a blank entry indicates a negligible value $o(a^3)$. For the concrete example of the perturbative analytic expression, I describe and interpret the four terms in Equation 3.16:

Γ_α relates purely to surface area. Because of variations in the area element ($\sqrt{g} \neq 1$), from this effect neighboring axial modes become coupled to each other $\sim a^{|j-j'|}$. The slice is identical for any two values $\beta = \beta'$, otherwise zero. Unlike axial modes, neighboring azimuthal modes are not coupled to each other by the perturbation in surface area.

The matrix Γ_α also gives elements of the matrix $D_{jlj'l'}$ pertaining to the quartic term, for which I introduce a shorthand notation $D_{ii'}$ with two indices:

$$D_{(j+l)(j'+l')} := D_{jlj'l'} = \frac{2}{\alpha u}(\Gamma_\alpha)_{(j+l)(j'+l')}. \tag{3.21}$$

The gradient term Γ_{c1} related to the part of momentum terms that is equivalent to flat space. It is affected by the shape perturbation in a way analogous to mass terms Γ_α, but includes factors of wavenumber $\mathbf{q} \cdot \mathbf{q}'$ in each element. In the β directions, slices are replicated times another factor of $\beta\beta'$.

Matrix $\Gamma_{c3} \sim |A_\theta|^2$ is an additional energy density, starting at $O(a^2)$, from surface-induced splaying of the order parameter field. It is nonzero where $\beta - \beta' = 0$ and $j - j' = 0$ or $j - j' = \pm 2$. As with Γ_α, the displayed slice is replicated identically for all $\beta - \beta' = 0$.
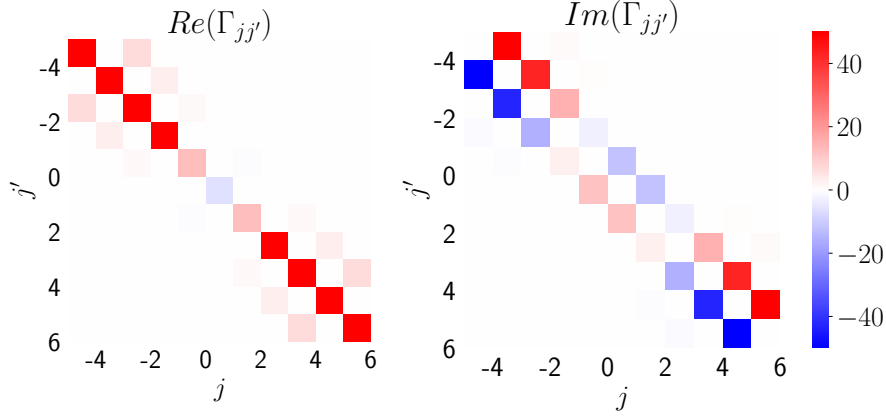
Figure 3.2: Total matrix $\Gamma_{jj'}$ at shape amplitude $a = 0.5$. Note that the colorscale has been capped at ± 50.

Finally let's examine Γ_{c2}: Here, factors of $\sqrt{g_{zz}}$, $r(a)$ cancel so that

$$(\Gamma_{c2})_{j\beta j'\beta'} = cnak(\beta + \beta') \int\int dz d\theta \cos kz e^{i(\beta+\beta')\theta} e^{i(j-j')kz}$$

$$\begin{cases} = \pm i(\beta + \beta')cn^2\pi^2a^2 & \text{if } |j - j'| = 2 \text{ and } |\beta - \beta'| = 0 \\ = 2(\beta + \beta')cn^2\pi^2a & \text{if } |j - j'| = 1 \text{ and } |\beta - \beta'| = 0 \\ = 0 & \text{otherwise.} \end{cases}$$

$$(3.22)$$

In the displayed slice at $\beta = \beta' = 0$, the matrix is trivially zero due to factor $(\beta + \beta')$. In general, this term has an interesting effect on higher azimuthal modes. Here it introduces a coupling between neighboring axial modes with the same small nonzero azimuthal wavenumber. It hints at the vortex configuration which we will see later.

The total quadratic operator $\Gamma_{jj'}$ is displayed in Figure 3.2. In general, in a statistical field theory of the form

$$Z = e^{-\beta\mathcal{H}}$$
$$\mathcal{H} = x^\dagger Ax = \sum x_j^* A_{ij} x_i,$$

$$(3.23)$$

with (possibly complex) vectors x and matrix A, correlations are given by the inverse of the matrix operator,

$$\beta\langle x_j^\dagger x_i \rangle = [A^{-1}]_{ij},$$

$$(3.24)$$
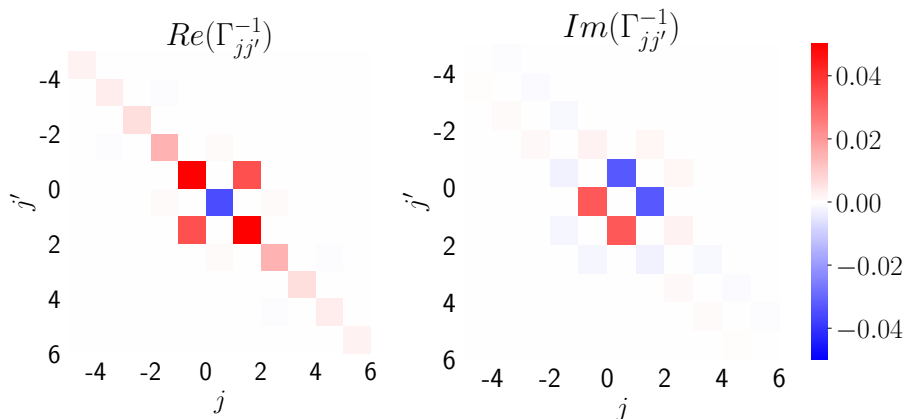
Figure 3.3: Inverse operator $G_{jj'} = [\Gamma_{jj'}]^{-1}$, indicating correlations between Fourier modes, at $a = 0.5$. While elements are displayed up to $j, j' = \pm 6$, matrices were numerically inverted using elements up to $j, j' = \pm 20$.

sometimes called the Green's function $G = A^{-1}$ [15]. On the diagonal of the inverted matrix $G = A^{-1}$, values $\langle x_i^\dagger x_i \rangle = G_{ii}$ indicate the mean magnitude of x_i. For correlators $\langle x_j^\dagger x_i \rangle = G_{ji}$, a positive value indicates statistical correlation between values of x_i and $x_j^\dagger$, while a negative value indicates anticorrelation. In systems with complex values, imaginary components of $\langle x_j^\dagger x_i \rangle$ indicate (anti-)correlation between real parts of x_i and imaginary parts of x_j and vice versa. If the phase of the complex values represents a spatial orientation, this would indicate that certain modes tend to be excited at right angles to each other.

Here, considering a system of quadratic form when $u_0 \ll |\alpha|$, the quadratic operator Γ can be inverted to give the Green's functions $G = \Gamma^{-1}$, elements of which have the direct interpretation as two-point correlation functions between two Fourier modes $\Psi_{\mathbf{q}}$ and $\Psi_{\mathbf{q}'}^*$: $\langle \Psi_{\mathbf{q}} \Psi_{\mathbf{q}'}^* \rangle = G_{\mathbf{q}\mathbf{q}'}$. Examples of values of $G_{jj'}$ are displayed in Figure 3.3. The values are complex. In the real part, the central negative value is unusual - the theory has negative 'mass' α and must include the quartic part to give meaningful results from this potential. Otherwise, the real part of the Green's function indicates (on the diagonal) decreasing expected amplitudes of Fourier modes with higher frequencies and (off-diagonal) positive correlations between modes j and $j \pm 2$. More interestingly, the imaginary part shows that imaginary modes $j \pm 1$ are correlated with modes j and therefore

tend to be antialigned with the corresponding mode $-j$. The symmetric pairs of Fourier modes with (on average) antialigned phases add up to a real mode of constant phase and spatially modulated magnitude, anticipating a sinusoidal pattern of increased and decreased magnitude of order on the surface.

3.2.2   Eigenfunctions

The sinusoidal modes $e^{i\mathbf{q}\cdot\mathbf{x}}$ are eigenfunctions of the Laplace operator on a periodic plane, or, equivalently, on the surface of the unperturbed cylinder. However, on modulated cylinders, Fourier modes are not eigenmodes of the covariant Laplacian. Having obtained expressions for the operator Γ, I numerically examine approximations of its eigenfunctions.

   The operators Γ are expressed as Hermitian matrices on the Hilbert basis of the set of fourier functions $g_i = e^{i\mathbf{q}\cdot\mathbf{x}}$. The basis and operator extends infinitely in all directions. It is no obstacle that in the most general case they are indexed by two vectors $\mathbf{q} = (\beta, j), \mathbf{q}' = (\beta', j')$ and appear four-dimensional; we can alternatively view this as a two-dimensional matrix by listing vector indices in arbitrary order.

   In general a Hermitian matrix operator can be diagonalized; the property extends to infinite-dimensional cases on a Hilbert basis (spectral theorem) such as Γ. In

$$\Gamma = U\Lambda U^H; \tag{3.25}$$

the diagonal matrix Λ gives the real eigenvalues λ_i, while columns of the Hermitian matrix U are eigenvectors of the operator Γ. The eigenvectors are a map from the space of Fourier modes to eigenfunctions of the covariant Laplacian on the given shape. Assuming eigenfunctions f_i of the operator Γ exist such that

$$\Gamma f_i = \lambda_i f_i, \tag{3.26}$$

eigenfunctions can be constructed from columns of U and the Fourier basis g_i as

$$f_j = u_{ij}g_i. \tag{3.27}$$

   There is no simple analytic expression for eigenfunctions on a sinusoidal cylinder. In the perturbative regime of shape modulations, I posit that eigen-

functions are only slight modifications to Fourier modes, $f_i = g_i + O(a^2)$, based on the example in the next section.

To numerically work with these matrices, I truncate the Fourier series at twenty terms in each direction. I obtain numerical values of $\Gamma_{jj'}$ and its eigenvalues and eigenfunctions for a specific example α, c, a, k. Entries of $\Gamma_{jj'}$ are obtained by numerically integrating Equation 3.16.

These numerical results can show us the shape of eigenfunctions. Coefficients u_{ij}, which can be used to construct eigenfunctions from Fourier basis functions as in Equation 3.27, are shown in Figure 3.4; examples of the resulting numerically constructed eigenfunctions are shown in Figure 3.5.

Examples

For the lowest eigenfunction, f_0, on the surface $a = 0.9$, we read off the top row of Figure 3.4-d. As indicated by the nonzero coefficients in this row, components of the eigenfunction f_0 are predominantly the Fourier basis functions $g_{-1} = e^{-iz}$ and $g_1 = e^{iz}$, with lesser contributions from $g_{\pm 2} = e^{\pm 2iz}$. In Figure 3.5-d, the lowest eigenfunction $f_0(z)$ is shown as the black line. The function has been constructed predominantly from Fourier components $g_{\pm 1}$ and $g_{\pm 1}$, weighted by the numerical coefficients in the first row of 3.4-d.

As another example, in 3.5-b, the second eigenfunction f_1 (green) on a lightly modulated shape $a = 0.1$ visually resembles a sinusoid with frequency 1. As can be read from the second row of in 3.4-b, it is nearly identical to (an arbitrary combination of the real parts of) Fourier components $g_{-1} = e^{-iz}$ and $g_1 = e^{iz}$.

The lowest-energy eigenfunction only will be excited at $0K$ and, approximately, dominate in the low temperature limit (lowest Landau level approximation). At higher temperatures additional eigenmodes are independently excited.

For small shape perturbations, the lowest energy level is almost identical to the first Fourier mode. Higher eigenfunctions differ more prominently from higher Fourier modes.

(a) $a = 0$

(b) $a = 0.1$

(c) $a = 0.5$

(d) $a = 0.9$
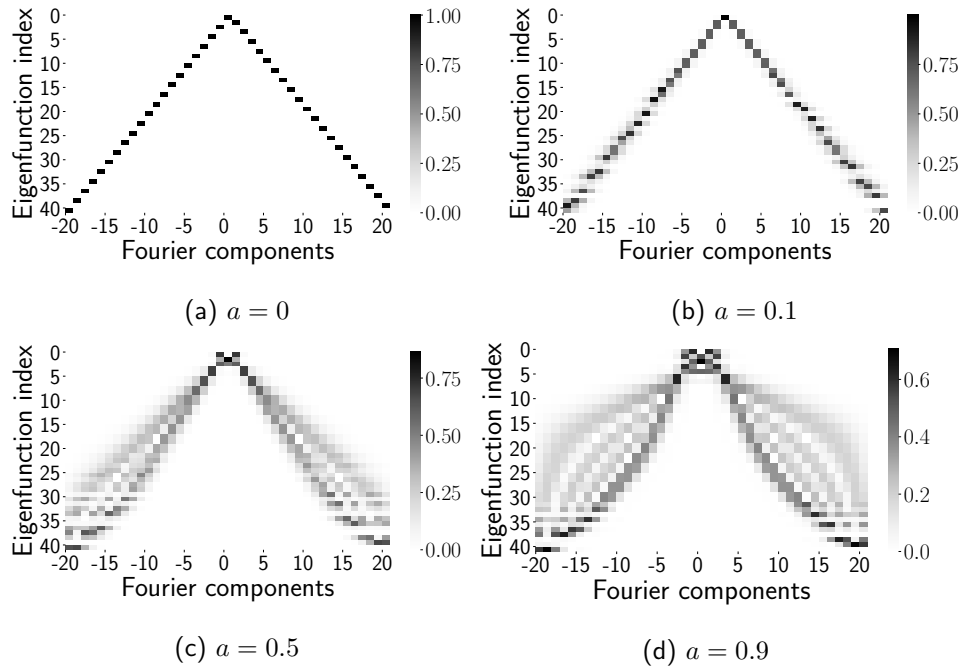
Figure 3.4: Visualization of the matrix U of eigenvectors, which gives a mapping from the basis of Fourier functions to the eigenfunctions f_i, labeled in order of increasing eigenvalue / decreasing statistical mean amplitude. (a) On the unperturbed shape, the set of eigenfunctions is identical to the set of Fourier modes, merely labels are changed from labeling by wavenumber to indexing by magnitude of eigenvalue. Fourier- and eigenmodes come in degenerate pairs. (b) Small perturbation to eigenfunctions: Eigenfunctions take on small components of neighboring Fourier modes and there is arbitrary mixing among degenerate eigenfunction pairs f_i, f_{i+1}. (c, d) For large shape modulations, the eigenvectors take on an alternating structure. Top eigenfunctions change place; the most significant eigenfunction f_0 is no longer one based on Fourier mode g_0.

(a) $a = 0$

(b) $a = 0.1$

(c) $a = 0.5$

(d) $a = 0.9$
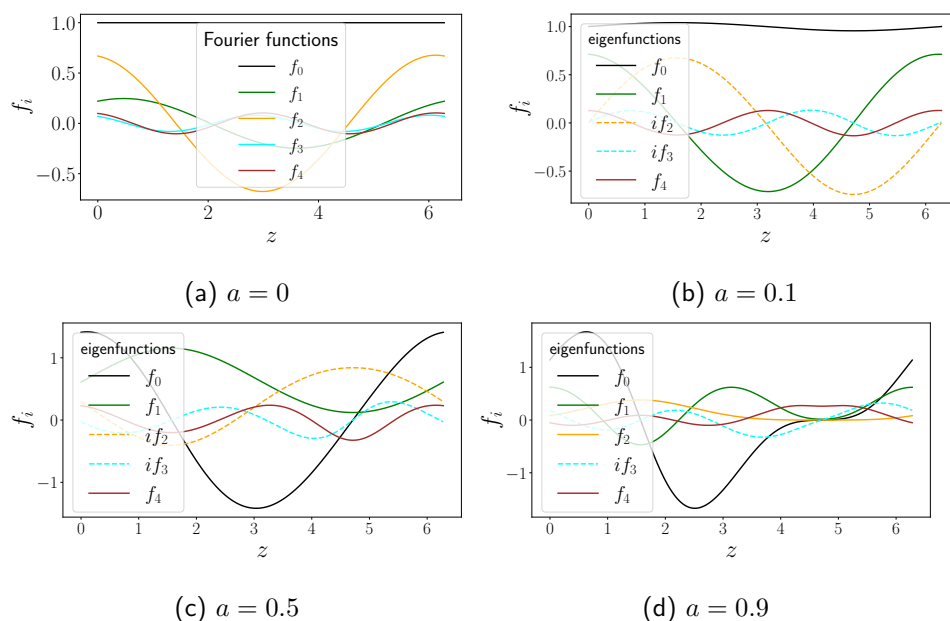
Figure 3.5: Examples of eigenfunctions. In (b-d) the arbitrary overall phase of the set of eigenfunctions has been rotated so eigenfunctions come in purely real and purely imaginary pairs. Eigenfunctions are weighted by their mean amplitude $1/\lambda_i$, normalized so that the first eigenfunction has mean amplitude 1. In the low temperature limit only the lowest eigenfunction (black) occurs. (a) Unperturbed eigenfunctions, identical to the Fourier modes. Here phase is arbitrary and only the real part is displayed. (b) In the mildly perturbed case f_i correspond to the first five sinusoidal modes g_i, albeit slightly altered. (c) On the highly modulated shape, an eigenfunction based on f_1 overtakes one based on f_0 as the first eigenmode. (d) On extremely modulated shapes, eigenfunctions are prominently asymmetrical, here indicating an overall decreased field amplitude on the narrow neck.

On more heavily modulated shapes, eigenfunctions have no obvious correspondence to Fourier modes. Field magnitude is decreased in two locations corresponding to the widest and narrowest parts of the cylinder. This anticipates the defect configuration predicted in Section 3.4. However, the eigenfunctions give an averaged picture of the ground state and cannot represent the breaking of continuous symmetries revealed by later analysis.

3.2.3 Perturbative effect of shape modulation on a uniform field

In the perturbative case, I now add the quartic term to the analysis. I examine the excitation, via coupling in the quadratic and quartic operators, of adjacent modes due to the onset of a small shape modulation on an initially uniform field. The nascent excitation of other modes is negligible (in other words, when the shape perturbation is small the 0th eigenmode of the true shape is sufficiently similar to the 0th Fourier mode), so that the common assumption of a uniform field in linear stability analysis (for example, by Lenz and Nelson [13]) is justified.

On an axisymmetric surface shape, modes with different azimuthal wavenumbers q_θ are decoupled from each other. If initially only the zeroth mode, Ψ_0, has a nonzero amplitude, azimuthally varying modes with $\beta \neq 0$, are not excited by curvature-induced coupling to this mode. I will therefore ignore the existence of azimuthally varying modes. The problem at $0K$ is reduced to the quasi-one-dimensional problem, with the one-dimensional field $\psi(z)$ denoted by lowercase ψ. Its Fourier transform is $\psi_j = \psi_{\mathbf{q}=(j,0)}$.

The one-dimensional field is subject to Hamiltonian

$$\mathcal{H}_I = \sum_{jj'} \psi_{j'}^\dagger \Gamma_{jj'} \psi_j + \sum_{jlj'l'} \psi_{j'}^\dagger \psi_{l'}^\dagger D_{j'l'jl} \psi_j \psi_l. \tag{3.28}$$

By perturbing around the flat-space solutions $|\psi_0^{(0)}| = \sqrt{\frac{-\alpha}{u}}$, and other $\psi_{\pm i}^{(0)} = 0$, we have

$$\psi_0 = \psi_0^{(0)} + \psi_0^{(1)} + \psi_0^{(2)} + o(a^3)$$
$$\psi_{\pm 1} = 0 + \psi_{\pm 1}^{(1)} + \psi_{\pm 1}^{(2)} + o(a^3)$$
$$\psi_{\pm 2} = 0 + \psi_{\pm 2}^{(1)} + \psi_{\pm 2}^{(2)} + o(a^3)$$

$$\tag{3.29}$$

$$\ldots$$

with $\psi_i^{(1)}$ representing an order a term, $\psi_i^{(2)}$ an order a^2 term.

Keeping in mind that matrix elements $\Gamma_{jj'}$ are of order $a^{|j-j'|}$ and $D_{jlj'l'}$ are of order $a^{|j+l-j'-l'|}$, we retain only elements of Equation 3.28 up to order a^2:

$$
\begin{aligned}
\mathcal{H}_I = {} & \psi_0\psi_0^*\Gamma_{00} \\
& + \psi_1\psi_0^*\Gamma_{10} + \psi_{-1}\psi_0^*\Gamma_{-10} \\
& + \psi_0\psi_1^*\Gamma_{01} + \psi_0\psi_{-1}^*\Gamma_{0-1} \\
& + \sum_{j\geq 1}\left(\psi_j\psi_j^*\Gamma_{jj} + \psi_{-j}\psi_{-j}^*\Gamma_{-j-j}\right) \\
& + \psi_0\psi_0\psi_0^*\psi_0^*D_{00} \\
& + 2\psi_1\psi_0\psi_0^*\psi_0^*D_{10} + 2\psi_{-1}\psi_0\psi_0^*\psi_0^*D_{-10} \\
& + 2\psi_0\psi_0\psi_1^*\psi_0^*D_{01} + 2\psi_0\psi_0\psi_{-1}^*\psi_0^*D_{0-1} \\
& + \sum_{j\geq 1}\left(4\psi_0\psi_j\psi_0^*\psi_j^* + 4\psi_0\psi_{-j}\psi_0^*\psi_{-j}^* + 2\psi_j\psi_{-j}\psi_0^*\psi_0^* + 2\psi_0\psi_0\psi_j^*\psi_{-j}^*\right)D_{00},
\end{aligned}
$$
$$(3.30)$$

In the last line we have used the fact that all values on the diagonal of D in its reduced notation are equal (Equations 3.21 and 3.17) to replace D_{jj} and D_{-j-j} with D_{00}.

Let k stand for an index $|k| \geq 2$. To find ψ_k, we solve $\frac{\partial \mathcal{H}}{\partial \psi_k^*} = 0$:

$$\frac{\partial\mathcal{H}}{\partial\psi_k^*} = \psi_k\Gamma_{kk} + (4\psi_0\psi_k\psi_0^* + 2\psi_0\psi_0\psi_{-k}^*)D_{00} = 0 \tag{3.31}$$

at leading order, a,

$$
\begin{aligned}
\frac{\partial\mathcal{H}}{\partial\psi_k^*} &= \psi_k^{(1)}\Gamma_{kk}^{(0)} + (4\psi_0^{(0)}\psi_k^{(1)}\psi_0^{*(0)} + 2\psi_0^{(0)}\psi_0^{(0)}\psi_{-k}^{*(1)})D_{00}^{(0)} = 0 \\
&(\Gamma_{kk}^{(0)} + 4|\psi_0^{(0)}|^2 D_{00}^{(0)})\psi_k^{(1)} + |\psi_0^{(0)}|^2 D_{00}^{(0)}\psi_{-k}^{*(1)} = 0
\end{aligned}
\tag{3.32}
$$

All matrix elements are on the diagonal of the Hermitian matrices Γ and $D_{ij} \sim \Gamma_{ij}^\alpha$ and therefore real. $(\psi_0^{(0)})^2 = |\psi_0^{(0)}|^2$ is real because we have chosen earlier without loss of generality to fix the phase of $\psi_0^{(0)}$ to the real direction. At first order equation 3.32 we have

$$\psi_k^{(1)} = -\frac{|\psi_0^{(0)}|^2 D_{00}^{(0)}}{\Gamma_{kk}^{(0)} + 4|\psi_0^{(0)}|^2 D_{00}^{(0)}}\psi_{-k}^{*(1)}. \tag{3.33}$$

However, by starting with another other choice of minimization, $\frac{\partial \mathcal{H}}{\partial \psi_{-k}^*} = 0$, the outcome is

$$\psi_{-k}^{(1)} = -\frac{|\psi_0^{(0)}|^2 D_{00}^{(0)}}{\Gamma_{-k-k}^{(0)} + 4|\psi_0^{(0)}|^2 D_{00}^{(0)}} \psi_k^{*(1)}, \tag{3.34}$$

Equations 3.33 and 3.34 are in general contradictory statements about the magnitudes of $\psi_k^{(1)}$ and $\psi_{-k}^{(1)}$. They imply that the only general solution is $\psi_k^{(1)} = 0, \psi_{-k}^{(1)} = 0$ for all $|k| \geq 2$. The magnitude of the modes $\psi_{\pm k}$, $k \geq 2$ is then at leading order proportional to (a^2) or smaller; their contribution to the energy $\mathcal{H}_I$ is at least $O(a^4)$.

For indices $j = \pm 1$, solving $\frac{\partial \mathcal{H}}{\partial \psi_1^*} = 0$, we have

$$\frac{\partial \mathcal{H}}{\partial \psi_1^*} = \psi_0 \Gamma_{01} + \psi_1 \Gamma_{11} + 2\psi_0 \psi_0 \psi_{-1}^* D_{01} + (4\psi_0 \psi_1 \psi_0^* + 2\psi_0 \psi_0 \psi_{-1}^*) D_{00} = 0 \tag{3.35}$$

at leading order

$$\frac{\partial \mathcal{H}}{\partial \psi_1^*} = \psi_0^{(0)} \Gamma_{01}^{(0)} + \psi_k^{(1)} \Gamma_{11}^{(0)} + (4\psi_0^{(0)} \psi_k^{(1)} \psi_0^{*(0)} + 2\psi_0^{(0)} \psi_0^{(0)} \psi_{-k}^{*(1)}) D_{00}^{(0)} = 0$$

$$(\Gamma_{kk}^{(0)} + 4|\psi_0^{(0)}|^2 D_{00}^{(0)})\psi_k^{(1)} + |\psi_0^{(0)}|^2 D_{00}^{(0)} \psi_{-k}^{*(1)} = -\psi_0^{(0)} \Gamma_{01}^{(0)} \tag{3.36}$$

The value $\Gamma_{01}^{(0)}$ is order a, complex conjugate to $\Gamma_{10}^{(0)}$ and $\Gamma_{0-1}^{(0)}$, and equal to $\Gamma_{-10}^{(0)}$. Bringing together all four equations $\frac{\partial \mathcal{H}}{\partial \psi_1^*} = 0$, $\frac{\partial \mathcal{H}}{\partial \psi_1} = 0$, $\frac{\partial \mathcal{H}}{\partial \psi_{-1}^*} = 0$, $\frac{\partial \mathcal{H}}{\partial \psi_{-1}} = 0$, we again arrive at a contradiction unless $\psi_1^{(1)} = \psi_{-1}^{(1)} = 0$.

Lastly we examine next order terms of ψ_0 in Equation 3.30. For symmetry reasons, $\psi_0^{(1)} \sim a$ must vanish: whether the overall magnitude of the field on the surface increases or decreases on shape perturbation cannot depend on the sign of the sinusoidal perturbation. For $\psi_0^{(2)}$, we solve

$$\frac{\partial H}{\partial \psi_0^*} = \psi_0 \Gamma_{00} + 2\psi_0 \psi_0 \psi_0^* D_{0000}$$
$$+ \sum_{j \geq 1} \left(4\psi_0 \psi_j \psi_j^* + 4\psi_0 \psi_{-j} \psi_{-j}^* + 4\psi_j \psi_{-j} \psi_0^*\right) \Gamma_{00} = 0. \tag{3.37}$$

At order a^2 we must solve

$$\psi_0^{(2)} \Gamma_{00}^{(0)} + \psi_0^{(0)} \Gamma_{00}^{(2)} + 2(\psi_0^{(0)})^3 D_{0000}^{(2)} + 6\psi_0^{(2)} (\psi_0^{(0)})^2 D_{0000}^{(0)} = 0 \tag{3.38}$$

$$\psi_0^{(2)} = -\frac{\psi_0^{(0)}\Gamma_{00}^{(2)} + 2(\psi_0^{(0)})^3 D_{00}^{(2)}}{(1 - 6(\psi_0^{(0)})^2)\Gamma_{00}^{(0)}} \tag{3.39}$$

By definition of $\psi_0^{(0)}$ as solutions to Equation 3.5, $\psi_0^{(2)} = 0$.

Plugging the remaining potential perturbations starting at $o(a^2)$ into Equation 3.28, the resulting effects on system energy will be $o(a^4)$. The field can be regarded as constant as far as is relevant to the linear stability analysis.

3.3 Linear stability analysis

I now consider the effect of the interfacial order on the shape modulations. First, in line with the previous linear stability analysis of a cylindrical interface with spontaneous curvature, I examine the linear effect of n-atic order. Assuming the field is initially ordered $(\Psi(\mathbf{x}) = \Psi_0)$ on the unperturbed cylinder, at small shape perturbations with amplitude $a \ll 1$, according to the previous analysis the induced changes in field configuration are negligible in terms of their energetic contribution. In general, the energy a perfectly ordered field $|\Psi|(\mathbf{x}) = |\Psi_0| = \sqrt{-\alpha/u}$ would have on the modulated surface, including its contribution via γ, is

$$\mathcal{H}_I[\Psi(z) = \Psi_0] = 2\chi \int_S dS |A_\theta|^2 - \frac{\alpha^2}{2u} \int_S dS. \tag{3.40}$$

Inserting a perturbative expansion, to leading order the difference in internal energy is the gradient energy difference plus a term proportional to surface area change

$$\frac{\Delta\mathcal{H}}{A_0 a^2} = \chi k^2 - \frac{\alpha^2}{2u}\Delta A, \tag{3.41}$$

collecting field characteristics as $\chi = |\alpha|cn^2/(2u)$. The second term, an energy difference proportional to change in surface area ΔA, will be absorbed into surface tension. Lenz and Nelson [13], treating a hexatic field with constant magnitude equivalent to $|\alpha|/u = 1$, obtain a linear energy difference equivalent to the first term. Adding the effect of n-atic order to the energy difference Equation 2.32 and again finding roots, the limit of stability is

$$k_c(C_0, \chi) = \frac{1}{2}\Big(1 - 2\gamma - 4C_0 - 8\chi$$
$$\pm \sqrt{8(2\gamma - 3) + (-1 + 4C_0 + 2\gamma + 8\chi)^2}\Big)^{1/2}. \tag{3.42}$$

with energy densities again in units where $\kappa = 1$, $r_0 = 1$ and with γ here representing both the surface energy density $v_0 = -\alpha^2/(2u)$ and an effective surface tension from spontaneous curvature: $\gamma = \gamma_0 - \alpha^2/(2u) + C_0^2/2$. According to the linear analysis, a preferentially ordered field ($\alpha < 0$) has a stabilizing effect on the system via the first term of equation 3.41. While the second term, a negative effective surface tension from the ordered material, can theoretically induce an inverse Plateau-Rayleigh instability, where short-wavelength fluctuations grow to increase surface area, in the regime $|\alpha| \approx c$ studied here the stabilizing effect is dominant. Examples of the effect of order on critical wavenumber are shown in Figures 3.6 and 3.7. Increasing field alignment $|\alpha|$ results in a lower critical wavenumber (increasingly longer systems are stabilizes), including a lower critical bending rigidity κ_c, above which systems of all all lengths are stable. On the other hand increasing field bending rigidity and curvature coupling cn^2 results in a lower critical wavenumber function, while critical bending rigidity (x-intercept) and critical wavenumber in the absence of bending rigidity (y-intercept, $k_c = 1$) remain fixed.

3.4   Type II: The vortex state

Regarding energy-minimizing configurations of the order parameter field on more modulated shapes, Equation 3.2 allows some predictions.

In the azimuthal gradient term of Equation 3.2,

$$|D_\theta \Psi|^2 = |\partial_\theta \Psi|^2 + \frac{2nA_\theta}{r^2(a)}\mathfrak{Im}((\partial_\theta \Psi)\Psi^*) + n^2|A_\theta|^2|\Psi|^2, \qquad (3.43)$$

I note that the cross-term can take negative values, suggesting that gradient energy can be decreased by orientational order whose direction rotates as it winds around the cylinder in the azimuthal direction. The factor $g^{\theta\theta} = 1/g_{\theta\theta} = 1/r^2$, explicitly written in the middle term, is also implicitly present in tensor inner products $|X_\theta|^2$ in the other two terms.

The equation implies that, to minimize gradient energy, the order parameter field rotates azimuthally clockwise (counter-clockwise) in locations with positive (negative) values of the spin connection component A_θ, giving a maximally negative value of $A_\theta \mathfrak{Im}((\partial_\theta \Psi)\Psi^*)$. At a given axial location, the field orientation by an integer number m turns as it winds around the cylinder. Because

Figure 3.6: (a) Tuning field alignment α in Equation 3.42 has the effects of both lowering effective surface tension (moving critical surface-tension–bending rigidity from $\gamma_0 = 1.5$ to a higher intrinsic surface tension) and suppressing the onset of instability vie the χ term in Equation 3.42. Here $cn^2/u = 1$. (b) Tuning parameter $\chi \sim cn^2$ while leaving $v_0 = -1/2$ fixed has the effect of suppressing the critical wavenumber to lower values while leaving the critical bending rigidity (x-intercept), the bending rigidity-surface tension ration above which systems of all lengths are stable, fixed.

Figure 3.7: (a) Tuning field alignment α actually destabilized the cylinder around $C_0 = -3$, where the instability is induced by spontaneous curvature effects, while at higher $|\alpha|$ the onset of instability is suppressed via the χ term. Here $cn^2/u = 1$. (b) Parameter $\chi \sim cn^2$ is varied.
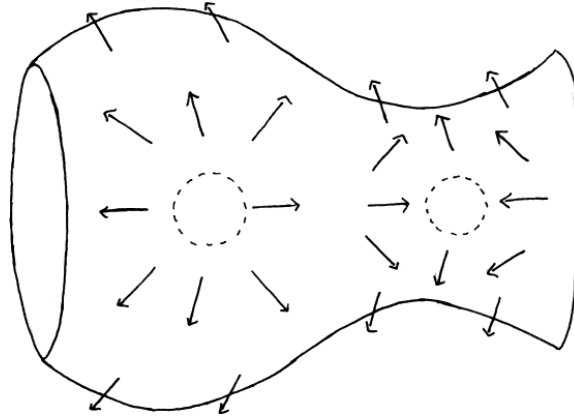
Figure 3.8: Simplest example of the predicted vortex state in a vector $(n = 1)$ field: Here a $+1$ defect is visible on the widest location and a -1 defect on the narrow neck. Two further defects are located on the back. Here the local rotation number is $m = \pm 1$ in axial regions between the defects and $M = |\Delta m| = 2$ defects occur where where the bands with different rotation number meet.

positive and negative values of the A_θ alternate on the modulated cylinder, there will be locations where counter-rotating bands of the order parameter field meet. In these locations, there will be at least $|\Delta m| = 2m$ topological defects. The simplest example of the predicted pattern, 4 defects in a vector field, is illustrated in Figure 3.8.

The vortex state is analogous to the Abrikosov [16] lattice phase of type II superconductors. In analogy with superconductors, I distinguish type I and type II systems. In type I superconductors, the material transitions directly from the superconducting state which expels an applied magnetic field (n-atic order which expels Gaussian curvature) to a non-superconducting state penetrated by a magnetic field (no order on a modulated surface). In type II superconductors, on the other hand, there is an intermediate vortex state, where the material is in the superconducting state almost everywhere but its phase (orientation of order) rotates around point defects, at which the magnetic field (Gaussian curvature) is concentrated. It is not surprising that behavior analogous to superconductors emerges, as the description of n-atic order coupled to surface

curvature is adapted from the Landau-Ginzburg equations for superconductors.

Counterintuitively, equation 3.43 implies that a certain chirality of the vortex state is always selected for: here system energy is minimized only by azimuthal modes winding around the cylinder clockwise on sections with positive spin connection and counterclockwise on sections with negative spin connection. However, this apparent symmetry breaking is a consequence of our choice to represent n-atic rotational order by Equation 3.1 rather than its complex conjugate field, or equivalently, to associate the order of rotational symmetry with the charge n rather than $-n$. In reality states that are solutions to either set of equations occur; the chiral symmetry is spontaneously broken when a vortex state develops. In contrast, where equations with the same form of minimal coupling are applied to electromagnetic phenomena (e.g. Dirac equation, Landau-Ginzburg equation for superconductors), with A_i representing the electromagnetic vector potential, there is only one correct set of equations describing the present universe: the equivalent chirality of electromagnetism is fixed.

3.4.1   Local onset of the vortex state

On the given closed surface, the n-atic field can undergo m/n rotations as it winds around the cylinder once, with integer m. Such a field is represented by the mode $\Psi = |\Psi_0|e^{im\theta/n}$. Plugging this trial mode into Equation 3.43, the local azimuthal gradient term is proportional to

$$|D_\theta \Psi|^2 = (m + nA_\theta)^2 \frac{|\Psi|^2}{r(a)} \qquad (3.44)$$

The first transition, when the energy can be minimized by selecting $m = 1$ rather than $m = 0$ rotations, occurs at the axial location $kz = \pi/2 + m\pi$, where the spin connection attains its maximal value of $|A_\theta| = 1$, at wavenumber

$$k(a) = \frac{\sqrt{2 + a^2}}{a\sqrt{-2 + 8n^2}}; \qquad (3.45)$$

In the case of $n = 6$ the lower bound wavenumber for onset of type II behavior is $\sqrt{3/286} \approx 0.102$, whereas in the case of $n = 1$ it is $1/\sqrt{2} \approx 0.707$. Analogous calculations for the transition from other values of m to $m + 1$ states suggest

that for 1- atic fields, modes with more than $m = 1$ azimuthal rotations are never energetically advantageous, while for hexatic fields the spectrum extends to $m = 6$. Locally, on cone-like sections of the object, the phenomenon is similar to one recently described on cones by Zhang and Nelson [17]. However, rather than being concentrated at the apex of a cone, $M = \Delta m$ defects here occur at the transitions between differently-sloped local areas. On one period of the surface vector order has either 0 or 4 defects, while for hexatic order there is a spectrum of states with $M = 4i$ defects extending up to $4n = 24$ defects. The wavenumber of onset predicted here is a lower bound based on local energy balance at locations $kz = \pi/2 + m\pi$. It depends on n but not on values of field parameters $\alpha < 0$, c. The true wavenumber of onset for the whole system will be increased by the interplay of several additional factors, including the energetic cost of defect cores, axial gradients, and the fact that the spin connection is less extreme at other locations; it does depend on coefficients c and α.

The prediction of up to $4n$ defects (per period of the modulation) in a system with n-atic order is an upper bound; it is the number of defects that can be attained at maximum curvature, limited to $|A_\theta| = 1$ in sinusoidal systems, and disregarding nonlocal consequences of field stiffness, which tend to decrease the number of defects actually realized.

3.4.2   Defects and defect charge

According to the above upper-bound calculation which considers only axially localized effects, defects of charge $\pm 1/n$ emerge preferentially at certain locations on the cylinder, namely on the widest and narrowest part. The defect charge is analogous to an electrostatic charge; like defects are repelled from each other. A line of Δm like charges on the wide/narrow neck will be maximally spaced from one another.

In the effective charge cancellation principle [18], Gaussian curvature acts as a diffuse background charge which interacts with defect charge. The sum of defect charge and Gaussian curvature charge in a small region s approximates

a locally neutral total charge:

$$qM + \frac{1}{2\pi} \int_s dS K \approx 0, \tag{3.46}$$

where M is the number of defects in a region s and $q = \pm 1/n$ their charge. Whether a defect around which the field winds clockwise or counterclockwise is assigned positive or negative defect charge varies between instances of the same system; it depends on the spontaneously broken chiral symmetry of order-curvature coupling.

Equation 3.46 can be derived in the special case of our cylinder-like system as follows: As reasoned above, at each axial location, in an idealized system the local number of azimuthal rotations m takes the integer value most closely minimizing local gradient energy (Equation 3.44), that is

$$m + nA_\theta \approx 0. \tag{3.47}$$

On the cylinder-like shape, the total number and sign of defects in a region between two axial locations z_1 and z_2 is the sum of differences in local rotation numbers, $\pm M = \int_{z_1}^{z_2} dz \sqrt{g_{zz}} \Delta_z m$. We similarly take an axial derivative and integrate axially over the second term of Equation 3.47 to obtain

$$\frac{\pm M}{n} + \int_{z_1}^{z_2} dz \sqrt{g_{zz}} \partial_z A_\theta \approx 0. \tag{3.48}$$

By relating spin connection to Gaussian curvature via the Mermin-Ho theorem (Equation 2.12), in this case simply as $\partial_z A_\theta = \sqrt{g_{\theta\theta}} K$, and by labeling charge $q = \pm 1/n$, we recognize Equation 3.46. The factor of 2π is equivalent to additionally carrying out an azimuthal integration over the latter term.

Like Equation 3.45, the number of defects predicted by topological charge cancellation is an upper bound; for materials with large persistence length fewer defects may be realized.

Although curvature-induced, the defects are not topologically mandatory, as the topological genus of the periodic cylinder is compatible with zero defects. They occur in charge-neutral pairs of defects with defect charge $+1/n$ and $-1/n$. The defects are analogous to excess defect pairs that could appear on a sphere in addition to the topologically mandated $2n$ defects.

3.5   Type I: One-dimensional modulation

In the type I regime the field remains axially symmetric and constant in phase. The equations can therefore be simplified to a real field in a one-dimensional potential:

$$\mathcal{H}_I^{m=0} = \int dS \left[\alpha'(z)\psi^2 + \frac{c}{r^2(a,z)}(\partial_z\psi)^2 + \frac{u}{2}\psi^4 \right], \qquad (3.49)$$

with spatially varying coefficient

$$\alpha'(a,z) := \alpha + \frac{c}{r^2(a,z)}n^2(A_\theta(a,z))^2 \qquad (3.50)$$

where $m = 0$ denotes the vortex-free type I state and lowercase $\psi(z)$ stands for a one-dimensional real field, as orientation of order is uniform in an arbitrarily chosen direction.

I further integrate azimuthally to obtain

$$\mathcal{H}_I^{m=0} = 2\pi r(a) \int dz \sqrt{g_{zz}} \left[\alpha'(a,z)\psi^2 + \frac{c}{r^2(a,z)}(\partial_z\psi)^2 + \frac{u}{2}\psi^4 \right]. \qquad (3.51)$$

Examples of the spatially varying coefficient $\alpha'(a,z)$, are shown in Figures 3.11 to 3.12. The curvature-induced addition A_θ^2 to α' is zero on both the narrow neck and the broadest part of the cylinder, where the surface is flat in the sense of the splay-inducing connection. The splay-inducing effect is largest on the curved, but narrow regions of the cylinder. This factor indicates that the cylinder is more tightly curved and the splay-inducing effect is amplified where its radius is small.

I numerically minimize the function $\psi(z)$. Alongside the potentials, I show the energy-minimizing field profile in a range of cases in Figures 3.11 to 3.12. I examine high and low bending rigidity c and the cases $n = 1$ and $n = 6$. While field bending rigidity c affects both the gradient and the coupling to surface curvature, the factor n affects only the field's sensitivity to surface curvature. Hexatic (n=6) layers are more resistant to surface-induced splay. With $n^2 = 36$, the effect can be large and the curvature-induced gradient dominates over the other gradient term. The two effects are to some extent separately tunable via the parameter n in the equations, although in practice it is a material parameter occurring only as the values $n = 1, 2, 4, 6$.
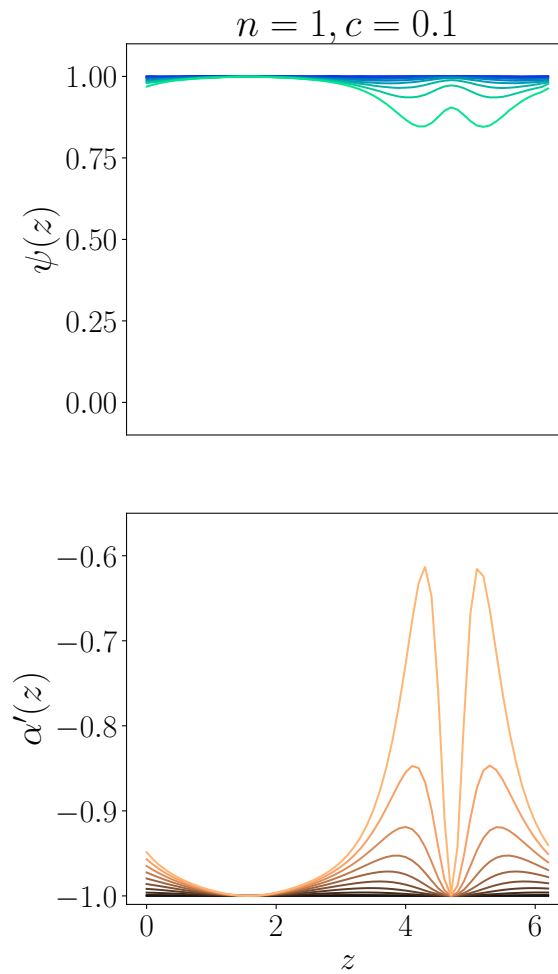
Figure 3.9: (top) The solution $\psi(z)$ minimizing Equation 3.51 in the case $c = 0.1, n = 1$, for a range of surface shape amplitudes a. (bottom) The spatially varying coefficient $\alpha'(z) = \alpha_0 + c_0 n^2 |A_\theta(z)|^2$ characterizing the spatially varying effective potential in Equation 3.51.
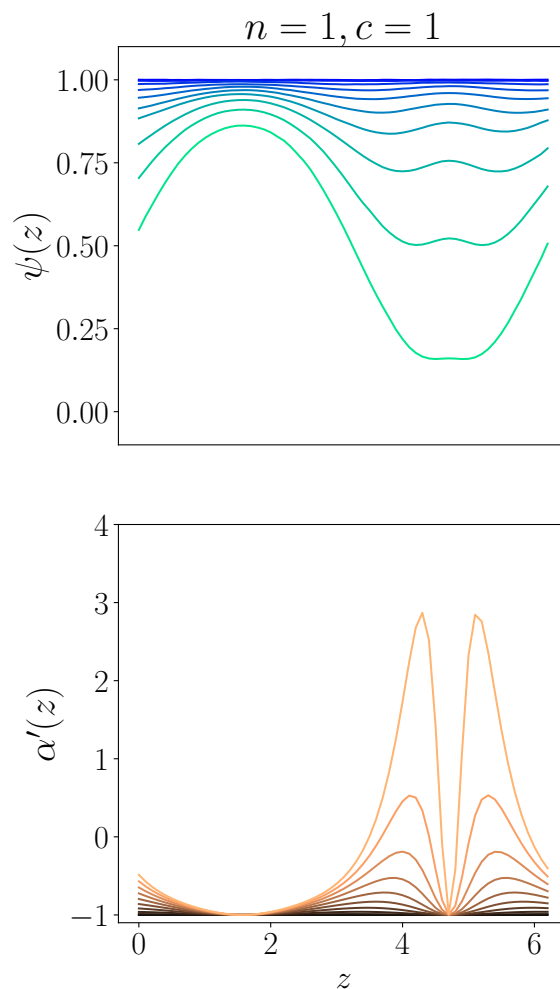
Figure 3.10: (top) The solution $\psi(z)$ minimizing Equation 3.51 in the hexatic case $c = 1, n = 1$, for a range of surface shape amplitudes a. (bottom) The spatially varying coefficient $\alpha'(z)$. Note different y-axis scale than in Figure 3.11. With higher curvature coupling, the effect of curvature is greater but solutions are less localized.
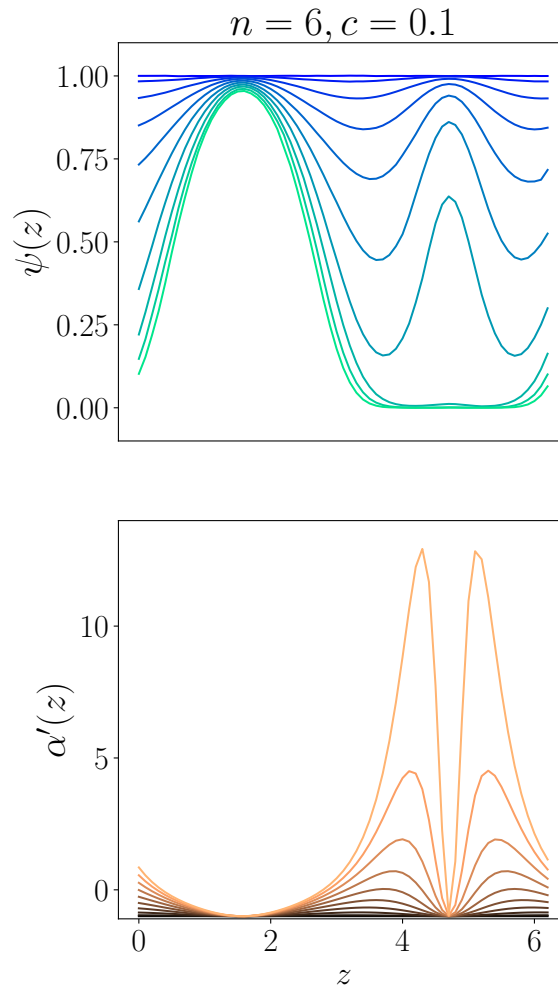
Figure 3.11: (top) The solution $\psi(z)$ minimizing Equation 3.51 in the hexatic case $c = 0.1, n = 6$, for a range of surface shape amplitudes a. (bottom) The spatially varying coefficient $\alpha'(z)$. In the hexatic case the effect of curvature on $\alpha'(z)$ is stronger and solutions are more effectively dampened.
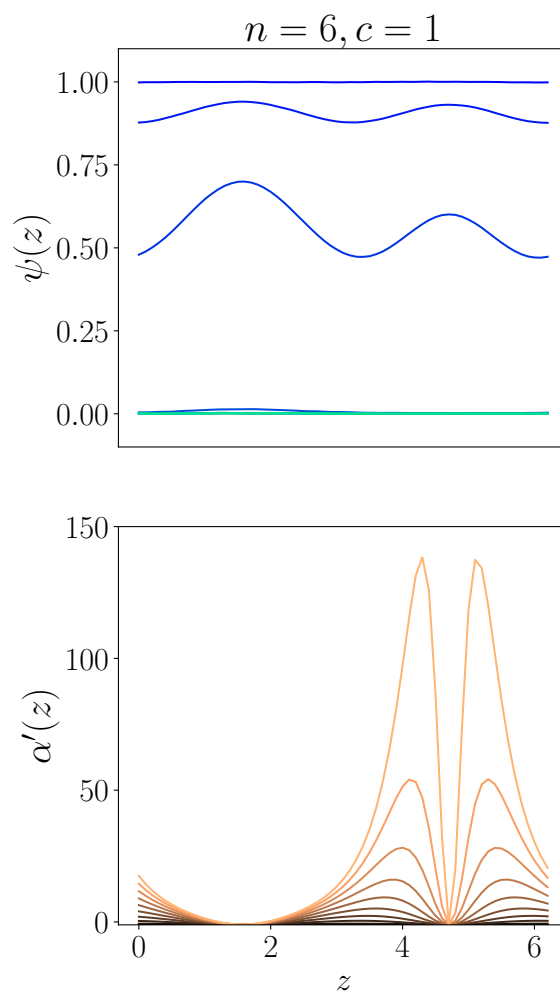
Figure 3.12: (top) The solution $\psi(z)$ minimizing Equation 3.51 in the hexatic case $c = 1, n = 6$, for a range of surface shape amplitudes a. (bottom) The spatially varying coefficient $\alpha'(z)$. For both hexatic order and high curvature coupling, the solution can be an everywhere isotropic field $\psi(z) = 0$.

3.6   Discussion and Conclusions

In this chapter I set up the Landau-Ginzburg theory of an n-atic order parameter field on the modulated channel shape and derive analytic outcomes in a range of cases. Together, the predictions form a comprehensive picture of field behavior in the low temperature limit.

Fourier-space analysis of the quadratic operator shows various ways in which the curvature-coupled field is affected by the geometric setting. Field configurations on the curved shapes can be predicted on a statistical level by numerical analysis in Fourier space. For perturbative small shape fluctuations, the Fourier space analysis further reveals that the field configuration does not change to relevant orders, justifying the linear treatment with an unchanged field.

In real space and beyond the perturbative regime of shapes, I predict a delineation into type I and type II behaviors. The predicted type II vortex phase is analogous to the Abrikosov vortex lattice phase of superconductors. There are multiple broken symmetries. In the defect-free type I case, the Hamiltonian can be cast in a simpler one-dimensional form with locally varying effective mass. An estimation of when the simpler treatment is applicable and when more complex, probably numeric treatment is necessary is therefore useful.

Fourier space and real space analysis provide simplifying assumptions and allow a wide range of special cases to be accessed analytically.

One simplifying assumption I did not directly use is an abstraction into discrete defects in an otherwise uniform field. The theory on the level of defects is standard and has been extensively covered elsewhere in the literature. Full representation of the order parameter field, including the possibility of varying magnitude, is here crucial to revealing a high-temperature-like effect of curvature, resulting in a banded profile of alternating ordered and isotropic material.

As in Chapter 2, the surface shape remains confined to axisymmetric sinusoidal variations on a cylinder. Given the analogy to the Abrikosov vortex state, where magnetic field lines are concentrated at vortex centers, and experimental observations of facetted droplets as a result of hexatic order [10], it is reasonable to expect faceting of the cylinder-like shape. Defects are expected to coincide with angular protrusions or vertices in the surface shape, at which Gaussian curvature is concentrated. Such shape variations are beyond the scope of this

study and would be an interesting avenue for further research.

Similarly, fluctuations of the surface shape are neglected. At higher temperatures, thermal surface fluctuations would occur and have an effect on the field theory. A phenomenon analogous to the superheating transition of superconductors, where the field theory is renormalized by magnetic field fluctuations to include a cubic term [19, 20], might even be expected at higher temperatures. In addition, hexatic order in thermally fluctuating membranes modifies properties such as bending rigidity of the membrane [19].

For reasons explained in Chapter 4, fluctuations are in general not explored, as neither the Fourier space nor the numerical real space analysis used here consistently represents fluctuations. The results are accurate in the low temperature limit. I find the energy-minimizing field configuration, but do not explore properties of the high-temperature statistical ensemble of configurations.

Bibliography

[1] P. M. Chaikin and T. C. Lubensky, *Principles of condensed matter physics* (Cambridge university press Cambridge, 1995).

[2] D. R. Nelson and B. Halperin, Phys Rev B **19**, 2457 (1979).

[3] P. Keim, G. Maret, and H. H. von Grünberg, Phys Rev E **75**, 031402 (2007), 0610332.

[4] A. L. Thorneywork, J. L. Abbott, D. G. Aarts, P. Keim, and R. P. Dullens, J Phys Condens Matter **30**, 104003 (2018).

[5] J.-M. Park, T. C. Lubensky, and F. C. MacKintosh, EPL **20**, 279 (1992), 9606105.

[6] R. M. L. Evans, Eur Phys J **5**, 507 (1995), 9410010.

[7] R. M. L. Evans, Phys Rev E **53**, 935 (1996).

[8] M. J. Bowick and L. Giomi, Adv Phys **58**, 449 (2009).

[9] S. Guttman *et al.*, Proc National Acad Sci U S A **113**, 493 (2016).

[10] O. Marin, M. Tkachev, E. Sloutskin, and M. Deutsch, Curr Opin Colloid Interface Sci (2020).

[11] I. García-Aguilar, P. Fonda, E. Sloutskin, and L. Giomi, Phys Rev Lett **126**, 038001 (2021).

[12] J. Kumar Alageshan, B. Chakrabarti, and Y. Hatwalne, Phys Rev E **95**, 042806 (2017).

[13] P. Lenz and D. R. Nelson, Phys Rev E **67**, 19 (2003).

[14] G. Foltin and R. A. Lehrer, J Phys A **33**, 1139 (2000), 9901095.

[15] D. Tong, Lecture Notes (2017).

[16] A. A. Abrikosov, J Phys Chem Solids **2**, 199 (1957).

[17] G. H. Zhang and D. R. Nelson, Phys Rev E **105**, 054703 (2022).

[18] L. Mesarec, W. Góźdź, A. Iglič, and S. Kralj, Sci Rep **6**, 1 (2016).

[19] D. Nelson and L. Peliti, J Phys (Paris) **48**, 1085 (1987).

[20] M. K. Transtrum, G. Catelani, and J. P. Sethna, Phys Rev B **83**, 094505 (2011).

Chapter 4

Simulation

Abstract

A lattice Markov chain Monte Carlo simulation reveals field configurations on modulated cylindrical surface shapes. Simulations confirm the predicted delineation into type I and type II systems, with uniform orientation or up to $4n$ defects respectively. Combining the results from simulation with numerical data from Chapter 2, I estimate the combined effect of both membrane mechanics and orientational order on surface shape and stability. The effect of order is generally stabilizing, but the occurrence of the vortex state in type II systems amplifies the previously seen metastability phenomenon, where, despite local stability of the flat cylinder, a modulated shape is the global energy minimum. As the shape modulation increases, the system goes through a spectrum of discrete defect states, implying that there is a polymorphic spectrum of possible channel shapes. The accuracy of the lattice-based method applied to the curved surface is evaluated.

Table 4.1: Table of symbols, Chapter 4

symbol	meaning
ϕ	angle of individual particles or bonds
Ψ_{ij}	order parameter as a lattice
ℓ_z, ℓ_θ	dimensions of lattice cells
N	size of lattice
σ	sampling width in the McMC simulation protocol
E	field energy in simulation
n	order of discrete rotational symmetry or orientational order
α, c, u	coefficients of the field theory,
	material properties of the ordered interfacial layer
γ_0, κ, C_0	mechanical properties of the interface
k, a	parameters describing surface shape
m	local azimuthal rotation number
M	total number of defects

4.1   Simulation method

I turn to stochastic simulation to find field configurations minimizing Equation 3.2 on modulated surface shapes, and ultimately to estimate the configurations $[a, \Psi(\mathbf{x})]$ jointly minimizing total energy of the system modulated with a fixed wavenumber k. The simulation is a sequential Markov chain Monte Carlo simulation. Despite the curved surface shape, I represent the field as a square lattice.

The n-atic order parameter field is represented as a two-dimensional lattice of $N = (\lfloor 50/k \rfloor \times 50)$ complex values $\Psi(z_i, \theta_j)$. Each lattice point represents an area with dimensions $\ell_z^0 = 2\pi/\lfloor 50/k \rfloor$, $l_\theta^0 = 2\pi/50$ on the unperturbed cylinder; on modulated cylinders cell areas are modified to $\ell_z = \ell_z^0 \sqrt{g_{zz}}$, $\ell_\theta = \ell_\theta^0 \sqrt{g_{\theta\theta}}$. Each lattice cell is associated with a values g_{zz} and $g_{\theta\theta}$ of the metric as well as a value of the spin connection A_θ. The values are retrieved according to Equations 6.8 and 2.11 based on the axial location z of the cell and amplitude a of the surface.

As the basic step of the simulation, a single lattice cell is selected and its value $\Psi(z_i, \theta_j)$ is updated to a value drawn from a complex Gaussian distribution. The new value is accepted or rejected with acceptance probability $A = \min(1, e^{-\frac{\Delta E}{T}})$. This is the standard Metropolis-Hastings algorithm [1] for any symmetric proposal distribution; it fulfills detailed balance and converges on a stationary distribution proportional to states' Boltzmann probabilities. Here, the proposal distribution is a Gaussian around the current value.

In one Monte Carlo step , N randomly chosen cells are updated. Data is recorded at each measuring step consisting of 100 Monte Carlo steps. Simulations were usually run for 50000 measuring steps. Wavenumbers $k \leq 0.8$ in Figure 4.8 were run for 200000 steps and the additional data in the same figure, covering wavenumbers $k = 0.15$ to 0.3, the simulation was run for 100000 steps, as the longer lattices take longer to reach equilibrium. Throughout this study, the sampling temperature is $T = 0.001$.

An adaptive sampling protocol was used. Proposed values are drawn from a complex Gaussian distribution centered on the old value and with sampling width σ_Ψ. The base sampling width σ_Ψ is evolved according to the adaptive algorithm recomended by Garthwaite *et al.* [2]. The target acceptance rate was

set to 0.5. A single lattice sampling width σ_Ψ is used for each cell.

The Metropolis algorithm produces sampled data strictly proportional (in the limit of infinite sampling time) to the system's Boltzmann distribution for any constant and symmetric sampling distribution [3]. Here steps are sampled from Gaussian a distributions with an adaptive width σ; the distribution is symmetric but not constant over simulation time. A Metroplis algorithm with an adaptive sampling width is in general at risk of biased sampling, as certain regions of parameter space may be systematically sampled using a different distribution than others. However, the adaptive algorithm used here converges on a fixed sampling width after the first few hundred steps. Thus, later data, with a near-fixed sampling width, produces strictly valid sampling under the Metropolis algorithm [4, 5].

The energy difference on changing the value at a single lattice cell is calculated as

$$
\begin{aligned}
\frac{\Delta E_{i,j}}{\ell_z \ell_\theta} = {} & E^{mag}(\Psi_{i,j}^f) - E^{mag}(\Psi_{i,j}^i) \\
& + E^{zgrad}(\Psi_{i,j}^f, \Psi_{i-1,j}^i) - E^{zgrad}(\Psi_{i,j}^i, \Psi_{i-1,j}^i) \\
& + E^{zgrad}(\Psi_{i+1,j}^i, \Psi_{i,j}^f) - E^{zgrad}(\Psi_{i+1,j}^i, \Psi_{i,j}^i) \\
& + E^{\theta grad}(\Psi_{i,j-1}^f, \Psi_{i,j}^i) - E^{\theta grad}(\Psi_{i,j-1}^i, \Psi_{i,j}^i) \\
& + E^{\theta grad}(\Psi_{i,j+1}^i, \Psi_{i,j}^f) - E^{\theta grad}(\Psi_{i,j}^i, \Psi_{i,j+1}^i).
\end{aligned}
\tag{4.1}
$$

The magnitude-associated part of the energy is

$$
E^{mag}(\Psi_{i,j}) = (\alpha + cn^2 |A_\theta|^2)|\Psi_{i,j}|^2 + \frac{u}{2}|\Psi_{i,j}|^4.
\tag{4.2}
$$

Gradient energy ascribed to a site (z_i, θ_j) is the sum of

$$
E^{zgrad}(\Psi_{i,j}, \Psi_{i-1,j}) = cn \left| \frac{\Psi_{i,j} - \Psi_{i-1,j}}{\ell_z} \right|^2
\tag{4.3}
$$

and

$$
\begin{aligned}
E^{\theta grad}(\Psi_{i,j}, \Psi_{i,j-1}) = {} & \frac{cn}{r(a,z)} \left| \frac{\Psi_{i,j} - \Psi_{i,j-1}}{\ell_\theta} \right|^2 \\
& + 2cn \Im \left[(A_\theta \Psi_{i,j})^* \left(\frac{\Psi_{i,j} - \Psi_{i,j-1}}{\ell_\theta} \right) \right].
\end{aligned}
\tag{4.4}
$$

As the numerical implementation of the derivative operator, a simple back-

wards derivative is chosen:

$$\partial_z \Psi_{i,j} \approx \frac{\Psi(z_i, \theta_j) - \Psi(z_{i-1}, \theta_j)}{\ell_z}$$

$$\partial_\theta \Psi_{i,j} \approx \frac{\Psi(z_i, \theta_j) - \Psi(z_i, \theta_{j-1})}{\ell_\theta}$$

(4.5)

The chosen derivative implementation is asymmetric. Alternative implementations, for example the more symmetric three-point stencil, exist. However, the symmetric stencil suffers a checkerboard artifact, where diagonal sub-lattices become decoupled. I used the simplest and asymmetric choice, with which no apparent artifacts were observed. Formally, the error of the backwards numerical derivative compared to the true value of the first derivative of a function at (θ, z_j) is $O(\ell)$. However, the main contribution to the error is that the numerical derivative more closely describes the derivative at an intermediate location. If the numerical derivative is instead interpreted as a central difference around locations $\theta_{i-1/2}$ and $z_{j-1/2}$, the error relative to the true value of derivatives at the interstitial locations is $O(\ell^2)$. To calculate the total system energy, where squared directional derivatives are summed over the lattice, it is equally valid to sample numerical derivatives at interstitial locations. At the base lattice spacing $\ell^0 \approx 2\pi/50 \approx 0.13$ used here, in the worst cases with the largest local lattice spacing (unperturbed cylinders and on the widest locations), error on numerical derivatives is therefore of order 0.01. Decreasing the base lattice spacing ℓ_z^0 and ℓ_θ^0 would increase numerical accuracy of gradient energy terms, but was judged unnecessary as results were qualitatively similar in exploratory simulations.

The value of the gradient ascribed to a lattice site i more accurately applies to the interstitial location $i - 1/2$. While arbitrary labeling of gradient terms in their respective arrays usually has no effect on gradient energies, we here have field-gradient cross-terms such as $\Psi^*(\partial_i \Psi)$. The numerically calculated values of Ψ and $\partial_i \Psi$ describe the field at slightly different locations. In parallel with values of derivatives, values of A_θ are also retrieved at interstitial axial locations. There were apparently no symmetry-breaking artifacts from the location-discordant cross-terms.

A change to the value at lattice site (z_i, θ_j) also affects the gradient energy ascribed to neighbouring lattice sites (z_{i+1}, θ_j) and (z, θ_{j+1}). For this reason change in gradient energy both at the site itself and at two adjacent site appears

in Equation 4.1.

After each sweep, the total field energy E, a numerical representation of the internal energy $\mathcal{H}_I$ of the corresponding configurations of continuous fields, is evaluated and recorded as the sum

$$E(t) = \sum_{ij} \left[E^{mag}(\Psi_{i,j}) + E^{zgrad}(\Psi_{i,j}, \Psi_{i-1,j}) + E^{\theta grad}(\Psi_{i,j}, \Psi_{i,j-1}) \right] \quad (4.6)$$

over each lattice cell.

In addition to total field energy E, after each sweep an azimuthally averaged magnitude $\langle|\Psi|\rangle_\theta$ is recorded for every 10th axial location z_i. The system has several continuous symmetries; the global phase of the field and azimuthal placement of defects may vary slowly over simulation time without indicating a departure from equilibrium. On the other hand the quantity $\langle|\Psi|\rangle_\theta$ is a suitable observable for detecting equilibration. The optimal production dataset was detected by the method of minimizing statistical inefficiency [6], as implemented in the pymbar timeseries module [7, 8]. Autocorrelation in the timeseries of each observable was analysed independently and the maximum cutoff time from among these was used as a global cutoff for the simulation. By inspection of time series (Figure 4.1), it corresponds well to equilibration. For $n = 6$ simulations, cutoff times (in measuring steps of 100 Monte Carlo steps) were on average $\bar{\tau}_0 = 11140$ for the set of simulations of length 50000, $\bar{\tau}_0 = 79160$ for simulations of length 200000, and $\bar{\tau}_0 = 16804$ for simulations of length 100000. For the $n = 1$ simulations, which all remained in the relatively trivial defect-free states, simulation length was always 50000, and the average cutoff time was $\bar{\tau}_0 = 10203$. Mean quantities such as $\langle E \rangle_t$ refer to averages over the production region of the simulation, from cutoff τ_0 to the end.

The simulation was implemented in Python 3.8. The simulation was run on ARC3, part of the High Performance Computing facilities at the University of Leeds, UK. Arrays of simulations in two parameters, such as (α, c) or (a, k), of the single-threaded Python simulation were run in parallel using the scheduler's taskarray facility.
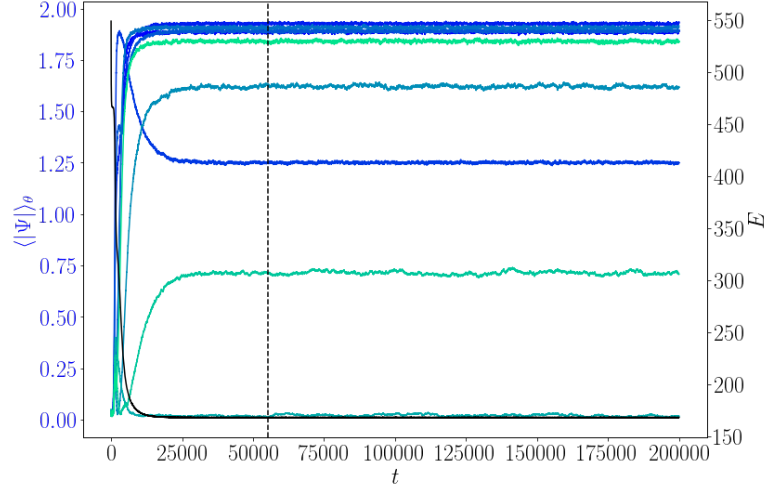
(a) Simulation $n = 6, \alpha = -4, c = 1, k = 0.6, a = 0.9$. A well-equilibrated but non-trivial type II example with cutoff point $\tau_0 = 55080$.
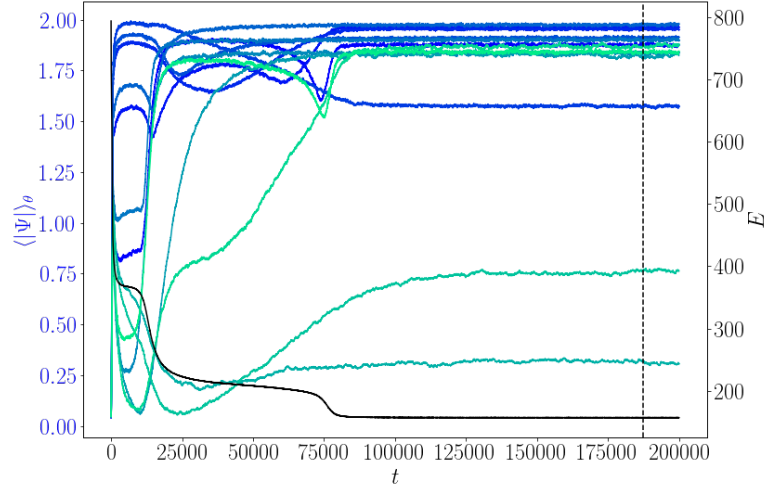
(b) Simulation $n = 6, \alpha = -4, c = 1, k = 0.4, a = 0.8$. An example with a late cutoff point $\tau_0 = 187440$.

Figure 4.1: Time series in total field energy E (solid black line) and additional observables $\langle |\Psi(z_i)| \rangle_\theta$ (solid blue to green lines), recorded at every 10th axial location z_i, over simulation time. Cutoff time τ_0 is shown as the dotted black line. Early trends in these values correspond to the emergence and axial migration of defects.

4.1.1 Scale-dependence of the high temperature theory

In the Ginzburg-Landau field theory 3.2, the coefficients $\alpha(T), c$, and u are scale-dependent phenomenological quantities. They encapsulate all effects, including entropic and interparticle interactions, below the scale on which the field theory is defined.

On the other hand, in the lattice simulation, the value Ψ_{ij} assigned to a lattice cell represents the mean over that cell of area $\ell_z \times \ell_\theta$. Unusually, cell dimensions vary spatially within the same simulation. Where the surface shape changes over simulation time, cell dimensions also vary over time within the same simulation. As an example, on a highly modulated surface $|a| = 0.9$, $k = 1$, the largest cells have dimensions $\ell_z^0 \times 1.6\ell_\theta^0$, while the smallest cells have dimensions $\ell_z^0 \times .08\ell_\theta^0$. In this case, areas of cells within the same simulation differ by a factor of 20. In addition, the smallest cells are highly anisotropic.

To more accurately represent statistical sampling of the same interfacial material on the different areas in the same simulation or set of simulations, scale-dependent phenomenological coefficients should be substituted.

In general the appropriate phenomenological coefficients are difficult to obtain, in certain limits, i.e. the near-Gaussian case $u_0 \ll |\alpha|$, these can be obtained perturbatively. The well-known perturbative momentum-shell renormalization of a quartic-quadratic field theory in two dimensions reads [9]

$$
\begin{aligned}
\alpha' &= \ell_z \ell_\theta (\alpha_0 + 8\frac{u_0}{2} \int_Q^{Q_{max}} G_0(\mathbf{q}) d\mathbf{q} + o(u_0^2)) \\
c' &= c_0 \\
u' &= \ell_z \ell_\theta (u_0 + o(u_0^2))
\end{aligned}
\tag{4.7}
$$

with $G_0 = \Gamma_0^{-1} = diag(\frac{1}{\alpha_0 + c_0 \mathbf{q}^2})$. The momentum-space integration carried out from the smallest cell dimension (largest wavenumber Q_{max}) in the simulation, in reference to which the unscaled coefficients α_0, u_0 are defined, to the wavenumber corresponding to the length of the cell in question. The factor 8 is appropriate for a complex field, equivalent in the Gaussian limit to two uncoupled scalar fields. For $x = 2$ fields (indexed $i, j = 1, 2$) there are $2(2+x) = 8$ combinatoric possibilities of connecting two legs in diagrams
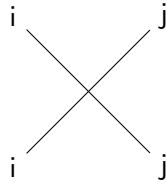
to form diagrams of the type
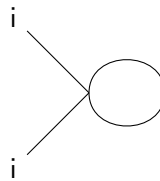
with two similarly-labeled external legs and one internal 4-way vertex corresponding to a factor of $u_0/2$.

The naive simulation, where energy is simply proportional to cell area, is equivalent to the correct rescaling of coefficients at zeroeth order in Equation 4.7.

For more accurate high-temperature simulations, coefficients in Equation 3.2 could be renormalized to better represent the behavior of the same field at the different lengthscales present in the same simulation. However, the utility of the perturbative equations is limited to certain regimes $u_0 \ll |\alpha_0|$ and $|c_0 Q^2| > |\alpha_0|$.

The effective coefficients become constants in the limiting cases of low temperature, where there are no rescaling thermal fluctuations. The rescaling is also less dramatic (logarithmic) when the scale of molecules or particles is a lot smaller than the scale of observation.

The Fourier-space analysis in Chapter 3 has the same problem as the real-space lattice simulation. Modes up to some cutoff wavenumber Q are considered. The coefficients are assumed to be defined at scales smaller than the smallest wavelength thus explicitly represented. For azimuthal modes, the cutoff is an angular wavenumber. However, the distance corresponding to the same angular wavenumber varies with local circumference of the modulated cylinder. Thus the Fourier space field theory is inconsistently defined, including modes up to a small cutoff wavelength on locations with a smaller radius and up to

a larger cutoff wavelength on wider sections of the object. Information about coupling between Fourier modes and the resulting eigenfunctions in Chapter 3 is thus only accurate in the low-temperature limit. While the analysis in Chapter 3 seems to give information about the statistical ensemble of Fourier modes and consequently of eigenfunctions, including statistical mean amplitude and correlations of higher modes, any results beyond the low-temperature ensemble, trivially comprising only the lowest eigenfunction, may be subject to some inaccuracy. The effect is less pronounced in the perturbative case of slightly modulated cylinders.

Without higher-order corrections to coefficients, the simulation protocol becomes exact only in the low-temperature limit. On the other hand, the uncorrected implementation used here has the advantage of conceptual and computational simplicity. While a balance must be struck between avoiding higher sampling temperatures and achieving adequate Monte Carlo sampling, the simulation protocol performs well in low-temperature simulations and is suitable to give qualitative results.

4.2 Simulation results

4.2.1 Configurations of orientational order

The lattice Markov chain Monte Carlo simulation was performed to obtain a qualitative picture of field configurations on a range of fixed surface shapes (k, a) in the low temperature limit. For hexatic order, a stepped dependence of internal energy on shape is apparent (Figure 4.2), with contours following lines of constant ka. The first discontinuity in energy corresponds to the onset of type II behavior in the form of the first defect state with $m = 1$, while each additional discontinuity corresponding to a transition to the next vortex state. The wavenumber of onset is about $k = 0.2$ in the hexatic cases. In an analogous set of simulations with $n = 1$ the onset of type II behavior is not seen for any k up to $k = 2.0$. While a transition to type II behavior is theoretically possible at some $k \geq 0.707$, as predicted in 3.4.2, for vector order it apparently occurs at larger wavenumber, smaller field stiffness c, or larger order $|\alpha|$ than those studied here.

(a) $n = 6, \alpha = -4$

(b) $n = 6, \alpha = -1$

(c) $n = 1, \alpha = -1$
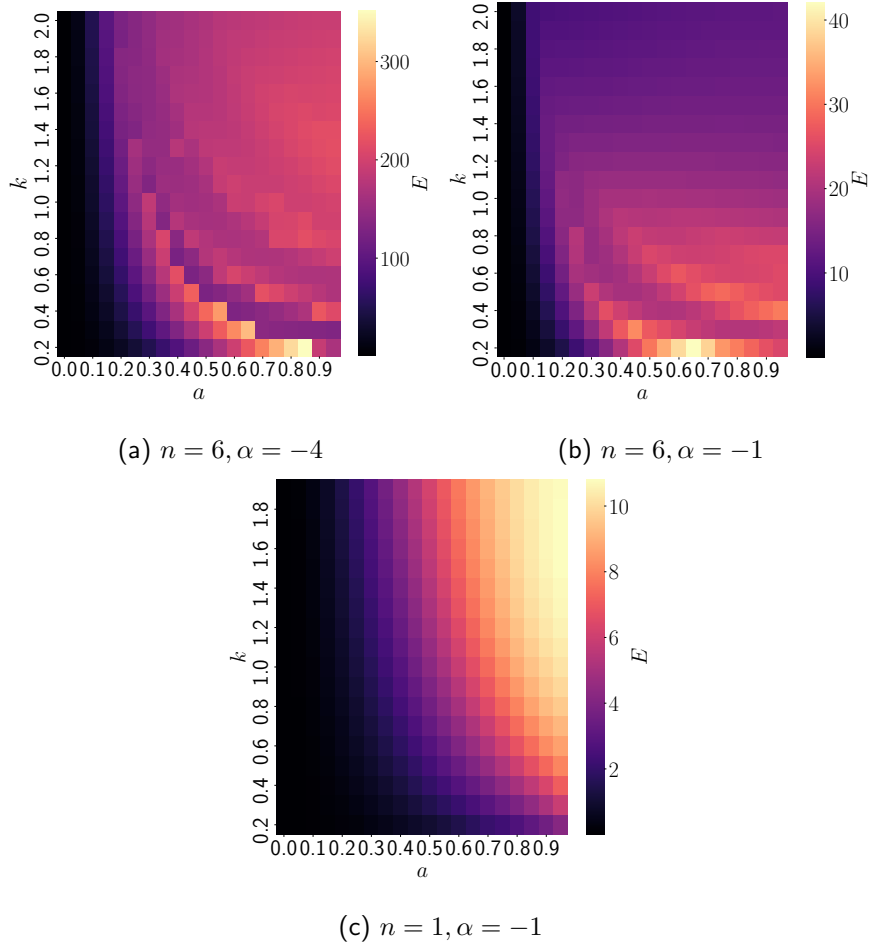
Figure 4.2: Total field energy $\langle E \rangle$ obtained on a range of surface shapes (k, a) with $c = 1$. While in the $n = 1$ case field energy increases monotonically in a for all k, for $n = 6$ there are multiple steps in the energy landscape, as the field transitions from the defect-free state to a spectrum of states $m = 0, ..., n$ with $4m$ defects.
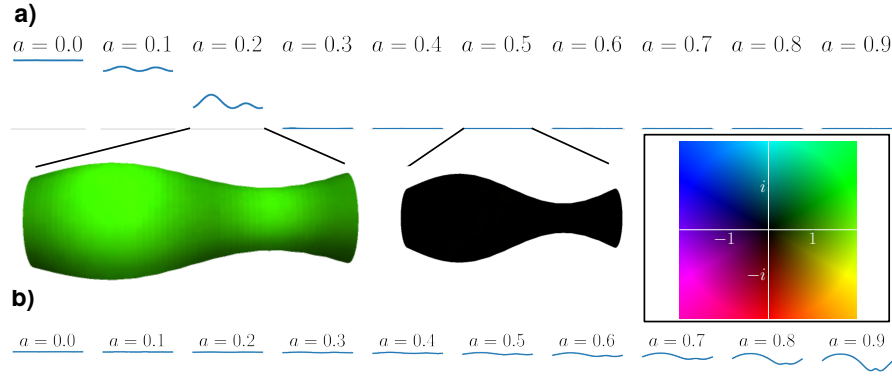
Figure 4.3: Examples of type I behaviour. Here the field configuration remains defect-free on a series of shape amplitudes from $a = 0$ to $a = 0.9$. The averaged field magnitude profile $\langle |\Psi| \rangle_{\theta,t}$ as a function of z is shown as a graph, with a horizontal axis where $|\Psi| = 0$ and $|\Psi| = 2$ at $a = 0$. (a) Magnitude profiles from series of simulations with $n = 6, \alpha = -4, c = 6.5, k = 0.9$. As shape amplitude increases, the field transitions from ordered field to locally depressed, then to everywhere isotropic. The characteristic magnitude profile is most depressed at two locations on either side of the narrow neck. Two simulation snapshots, a banded configuration and the uniform isotropic state, are rendered on the surface shape. (b) Series of magnitude profiles from simulations $n = 1, \alpha = -4, c = 4.5, k = 0.9$. The 1-atic field is more weakly affected by shape modulations. Inset: Colormap allowing visualization of complex values. Saturation, ranging from 0 to $|\Psi| = 2$, indicates field magnitude or amount of n-atic order, while hue indicates the phase of the complex field or the direction, up to a factor of n, of orientational order. Black corresponds to a value of $|\Psi| = 0$, the isotropic phase.

Two examples from simulation are shown in Figure 4.3, which shows, as profile plots $|\Psi|(z)$ and as rendered on the surface shape, two series of field configurations from simulation where the orientation of the field remained spatially uniform. The magnitude of order is modulated in characteristic profiles minimizing the one-dimensional Equation 3.51, while the uniform orientation is randomly selected. At sufficiently high curvatures, field bending rigidity and curvature coupling, the solution is everywhere isotropic, $|\Psi(z)| = 0$.

On the other hand, type II behavior is shown in Figure 4.4. As in the type I cases, order is locally decreased relative to the flat-space solution Ψ_0, especially on either side of the narrow neck. Additionally orientational order rotates azimuthally m times around the cylinder, and m times in the opposite direction on the other half. There must be $M = 2m$ defects with the total charge $\pm 2m/n$ where the counter-rotating bands meet at the narrowest and widest regions, for a total of $4m$ defects on the surface and a vanishing total defect charge. The defects on the narrow neck are topologically present but are often obscured by an isotropic band. At more extreme curvatures, the defects lie on a line at the narrowest and widest locations, whereas placement is more distributed in cases of less extreme curvature. The lattice simulation seems to qualitatively reproduce the well-known phenomenon that defect density is proportional to local Gaussian curvature, and indeed the number of defects appearing on the wider half of the cylinder in simulations roughly agrees with that predicted via the effective topological charge cancellation mechanism (Section 3.4.2).

I compare the energy obtained in low-temperature Monte Carlo simulation to the energies of these reference states. In Figure 4.5, we see that energy of the simulated field, which is allowed to adopt spatially varying configurations, is lower than that of either of the two uniform reference states. Type II behavior is again evident in the form of stepped energy functionals in the $n = 6$ case, Figure 4.5-b. The stepped energy function implies that certain surface shapes (k, a) are more compatible with the ordered interfacial layer than others, so that morphologies will be biased towards a discrete set of shapes.
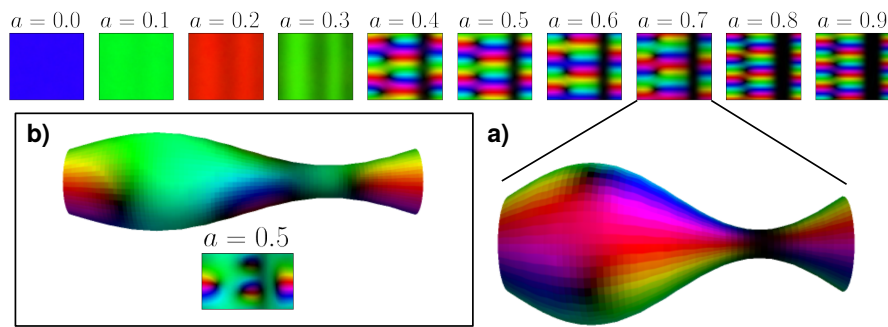
Figure 4.4: Examples of type II behavior in hexatic fields. The final field configuration snapshot is shown on the (z, θ) plane using the complex colormap (Figure 4.3, inset) to represent complex values. (a) Series in a with $n = 6, \alpha = -4$, $c = 1.5$, $k = 0.9$. As shape amplitude increases, the field here transitions from adapting to curvature via defect-free magnitude modulations to a state with $m = \pm 2$ discrete azimuthal rotations and finally one with $m = \pm 3$ rotations. There are $\Delta m = 2|m|$ visible defects on the widest part of the cylinder, while their counterparts on the narrow neck are often merged to an isotropic band. (b) An example of a more complex banding pattern on a longer cylinder, simulation $n = 6, \alpha = -4$, $c = 2.5$, $k = 0.6$, $a = 0.5$.
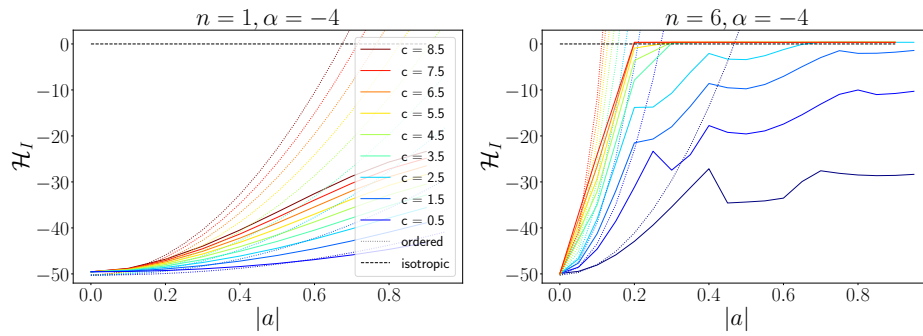
Figure 4.5: Solid coloured lines show mean field energy $\mathcal{H}_I(a)$ (per unit length) retrieved from simulations on fixed surfaces. As reference, I show the energy a uniformly ordered field Ψ_0 would have on the curved surface shape (coloured dotted lines), obtained by semi-numerically integrating Equation 3.40, and the energy of a uniformly isotropic field (black dashed line, zero). (a) For $n = 1$, the field is ordered at low a and at higher a adjusts by locally adapting magnitude, lowering energy slightly below that of the perfectly uniform field on the same surface. (b) For $n = 6$ the field with high bending rigidity c transition to the uniformly isotropic state on curved surfaces. For lower c the hexatic field, in addition to locally adapting its magnitude, is able to decrease its energy by adopting rotational states with defects, resulting in stepped energy curves.

4.2.2 Effects on stability

Having obtained energy functions $\mathcal{H}_I(k, a)$ for an array of values (k, a) from simulation, I combine these with semi-numerically integrated values $\mathcal{H}_E(k, \gamma_0, C_0)$ from Section 2.5. For each point (k, γ_0) in parameter space, I search numerically for shape amplitude a minimizing $\mathcal{H}(a) = \mathcal{H}_I(a) + \mathcal{H}_E(a)$.

The effect of a preferentially ordered field on cylinders with a range of spontaneous curvatures is shown in Figures 4.6, 4.7, and 4.8 as the shaded background, in comparison to the linear limit of stability.

For vector order $n = 1$, the vortex state does not emerge. The result seen in simulations aligns with the limit of stability predicted by linear analysis (Figure 4.6). The onset of shape instability is suppressed compared to the order-less scenario. The transition is continuous; at wavenumbers just below the critical wavenumber there are mildly modulated shapes which may actually be stable according to the analysis in Section 2.5.2.

For hexatic order, shape instability is more strongly suppressed. Below a certain wavenumber $k \approx 0.2$, where the behavior is of type I, the linear limit of stability is a good description and the shape transition is continuous. On the other hand at larger k, in the regime of type II behavior, the transition from flat to modulated cylinders induced by increasing γ_0 is discontinuous. The deviations from the linear prediction at larger wavenumbers is a result of the vortex state. It coincides with the previously observed metastability (Section 2.5.1). The effect of hexatic order on the phase diagram in C_0 (figure 4.8) is similar. Apparent critical endpoints, delineating type I from type II states and continuous from discontinuous transitions, are marked with orange crossed in Figures 4.7 and 4.8. The critical endpoint delineates second order transitions from unmodulated to modulated defect-free cylinders from a second order transition from unmodulated to modulated cylinders which may or may not have defects. Initially, close to the critical endpoint, the appearance of a first order phase transition is due to emerging secondary minima in the shape energy $\mathcal{H}_E$ only, as seen in Chapter 2 2 and exemplified by the energy landscape in Figure 2.9. Further into the metastability region above the critical endpoints, the vortex state appears and adds to the depth of the global secondary minima, extending the stability of the modulated and defect-bearing state.
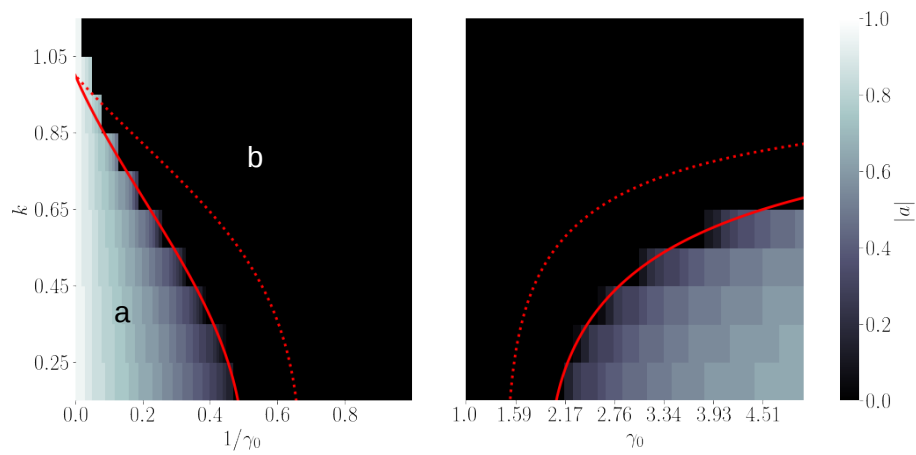
Figure 4.6: Shape amplitude predicted by simulation compared to linearly predicted critical wavenumber as a function of κ/γ_0 ratio and its inverse, (right) as a function of surface tension (in units of bending rigidity); (left) the same data as a function of inverse surface tension (in units of bending rigidity) , i.e. bending rigidity to surface tension ratio . The linear limit of stability (solid red line) is suppressed compared to the case with no order (dotted red line). For the $n = 1$ case simulation results corresponds closely to the linear prediction. There is a continuous transition between modulated (a) and flat (b) morphologies.
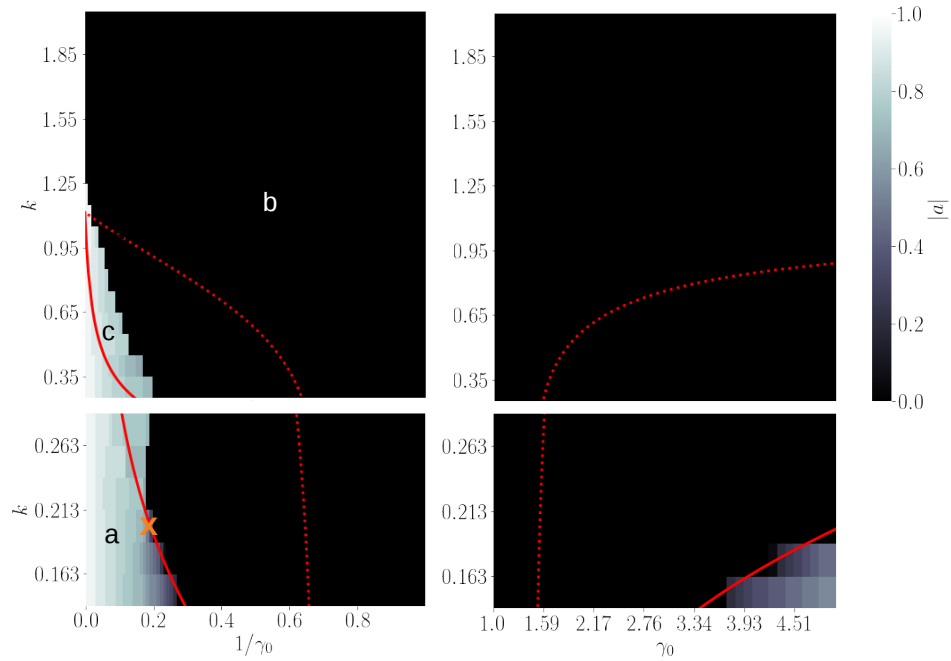
Figure 4.7: Shape amplitude predicted by simulation compared to linearly predicted critical wavenumber, (left) as a function of inverse surface tension; (right) as a function of surface tension. Bottom panels show the interesting region around $k = 0.2$ more closely at a finer grid spacing in k. There is a qualitative transition from type I field behavior at low wavenumber $k_c \lesssim 0.2$, inducing a continuous shape transition adhering to the linear prediction, to type II behavior at higher wavenumbers. In the latter case the transition is discontinuous and the linear limit of stability gives an incomplete description of the system. Above the linear limit of stability, there is a region of metastability (c), where a vortex state on a modulated surface ($|a| > 0$) is the global energetic minimum of a system with order and spontaneous curvature.
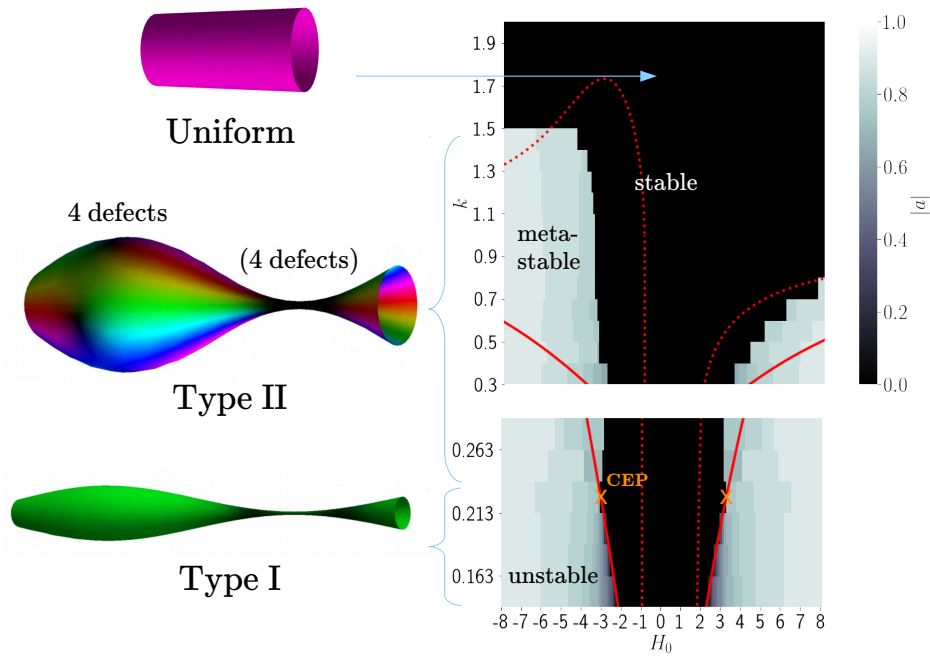
Figure 4.8: The effect of hexatic order with $c = 1$ and $\alpha = -1$ on critical wavenumber as a function of spontaneous curvature. The previously observed metastability in shape coincides with the vortex state, which amplifies the phenomenon. As before, the metastability region, where the vortex state on modulated cylinders dominates, is largest where the modulation is induced by negative spontaneous curvatures.

The energy recorded in simulation includes a contribution from thermal fluctuations. By the equipartition theorem, which would apply exactly if each complex value were subject to an independent harmonic potential only, the thermal energy may be estimated as $k_b T$ per lattice cell. At the given simulation temperature and lattice spacing, the value according to the equipartition estimate is a negligible $E_T = 0.4$ simulation energy units per unit length of cylinder. The value is visible as a small increase of simulation energies above reference energies in Figure 4.5. The value is an artifact of the lattice representation; it is not proportional to surface area but to number of lattice cells. This background thermal energy has no effect on field configurations sampled within a simulation or on comparative energetics of a set of simulations with the same wavenumber k.

4.3   Discussion and Conclusions

The numerical simulation presented here confirms theoretical predictions in Chapter 3 on configurations of order and allows these to be combined with interfacial mechanics from 2 for a comprehensive picture of the combined system. The prediction of a discrete spectrum of states, cylinders with certain shape modulations compatible with exactly $4m$ defects, is novel, as is the distinction between first and second order transition from modulated to unmodulated shapes. It may be particularly prominent in the regime $c \approx |\alpha|$ generically examined here.

Constructing simulations representing a soft ordered interface, with both flexible surface shape and particle orientational order, is an ongoing challenge. Here, a continuum field theory was represented in a lattice-based Monte Carlo simulation on the curved surface. A simple implementation of representing surface curvature on a non-adaptive square lattice was implemented and examined for correctness; the discussion may be of interest to others in choosing a method for adapting the simulation of statistical field theories to curved surfaces.

Alternative simulation designs include representing discrete particles, for example as by Smallenburg *et al.* [10]. Three-dimensional particle-based representations capture additional phenomena which are omitted in the two-dimensional

surface simulation, such as particle interactions through the bulk, giving the ordered material sensitivity to mean as well as Gaussian curvature. In addition to the emergence of orientationally ordered particle packings, simulations with explicit particles also allow for the emergence of different density regimes. In studies on positioning and and order of spherical particles on curved surfaces Law *et al.* [11], while only one 'fluid' is explicitly present, and is modelled as relatively large individual particles, phase separation into distinct gas, liquid, or crystalline regions results. The positioning of the phase boundary line on the curved surface is an additional factor determining the final configuration of the spheres on the surface. The authors study the thermodynamics of this system on a sphere and further curved surfaces, developing a corresponding theory for the size of critical liquid nucleus on a sphere [12].

Though conceptually distinct, the modulations in magnitude of order parameter observed here belong to the same Z_2 symmetry group as density variations, as does the fractionation of lipids on curved surfaces. Multiple numerical studies explore the relative concentration of two fluids as they phase separate, represented using either an order parameter field or discrete particles. Phase separation simulations to match their interesting experimental study on the demixing of lipid on fixed spherical and 'snowman' surfaces was performed by Fonda at al. [13]. Here a lattice-gas model was used to simulate the two fluids [14]. As in the corresponding experiments, phase separation is either inhibited or the emerging phases and the contact line show a preference for certain locations on the surface. Paillusson *et al.* [15] similarly investigate phase separation on triply periodic surfaces. As with orientationally ordered phases, there are strong effects of the interaction between geometry and the tension of the phase boundary.

Despite the distorted square lattice representation necessitating an application of the simulation protocol at low sampling temperatures only, the low-temperature simulation converges rapidly on energy-minimizing configurations and gives useful results which supplement theoretical predictions. Like the similar numerical minimization of Equation 3.51, the simulation allows the full Equation 3.2, without the assumption of uniform field magnitude, to be explored. In the type II as in the type I case, a banded pattern of locally decreased

order merges. The effect is reminiscent of the experimentally and theoretically observed behavior of other fields with Z_2 symmetry, such as lipid mixtures, on modulated surfaces.

The representation of the surface of revolution as a modified square lattice on a double periodic plane takes advantage of the particular topological genus. It is extendable to doubly periodic plain-, cylinder-, and torus-like systems, but not to spheres or to objects with evolving topological genus. While the lattice-based simulation accurately takes effects on curvature on order into account, the specific representation of the surface shape does not accurately reflect phenomena related to fluctuations at high temperatures. Simulation methods on which a mesh is adapted to the evolving surface shapes are more generalizable, for example as used by Ramakrishnan *et al.* [16, 17] and, in the context of active nematics, by Hoffmann *et al.* [18], to sample ordered materials on freely evolving surface shapes. On the other hand, there is additional computational cost and some inaccuracy associated with extracting geometric quantities, such as the local metric and curvatures, on an evolving and discretized triangulated surface.

In the implementation constructed here, theoretically, the shape amplitude a can be simultaneously sampled, so that the simulation converges on the joint configuration $[a, \Psi(\mathbf{x})]$ of surface shape and orientational order minimizing the system energy. To this end single steps of shape amplitude was alternated with sweeps of the field configuration. Sampling width σ_a of the shape amplitude was adapted in the same way. I found that achieving adequate sampling in a reasonable time was difficult. The field configuration adapted quickly to a shape a, then, given the optimized field configuration, the shape did not evolve due to hysteresis in the more complex energy landscape $E(a, \Psi_{ij})$. In addition, the shape amplitude sampling step is computationally costly, (re-)calculating external energy 2.30 by numerical integration over the sinusoidal shape as well as recalculating and summing the energy value of each lattice cell in Equation 4.6. While sampling problems might be improved by manual fine-tuning of the sequence and relative frequency of shape and field sampling steps and while theoretically, in the limit of infinite simulation time, even a poorly mixing simulation will yield correct statistics, in practice I found that the parameter space is

more efficiently covered by collecting a database of field energy on an array of fixed surface shapes (k, a). Thanks to the additive formulation $\mathcal{H} = \mathcal{H}_E + \mathcal{H}_I$, simulation data is then combined with the external energy $\mathcal{H}_E$, which can be quickly calculated, post hoc. Due to the low temperature, differences in configurational entropy across field configurations on different shape amplitudes are neglected and energy measured in simulation is taken as synonymous with free energy when constructing energy landscapes $\mathcal{H}(a)$.

A Fourier-space simulation, sampling the field as represented by coefficients $[\Psi_{\mathbf{q}}]$ and subject to Equation 3.12, was also considered and implemented. Integrating over the surface shape for matrix elements in 3.12 as well as recalculating the energetic effect via many quadratic and quartic terms of changing a single mode $\Psi_{\mathbf{q}}$ was found to be computationally inefficient. Only a truncation to the first few Fourier modes could be sampled in reasonable simulation time, which did not allow the visualization of axial modulations and vortex modes.

The interface as described by Equations 2.30 and 3.2 has additive effective surface tensions (energy per unit area) of $C_0^2/2$ as well as $-\alpha^2/(2u)$. Such effective surface tensions are to be interpreted relative to a reference system, such as similar molecules dissolved in the bulk phase. In the simulation protocol used here, the surface-tension-like effects can be easily subtracted or added post hoc as appropriate for the specific experimental system. I here chose to leave the negative effective surface tension contribution from the ordered material, as interesting experimental results [19] are seen in the regime where a hexatic interfacial material has a (transiently) near-zero or negative surface tension.

Unlike spherical droplets, the periodic cylinder model surface has no topologically mandated defects. All defects are excess defect pairs. The system could be used to study more exotic modes of deformation of facetted emulsion droplets, with additional defect pairs and stellated polyhedral morphologies [19], in isolation. Due to the constrained set of axisymmetric surface shapes, facetting is not seen. In general, in analogy to superconductors and in line with experimental observation on emulsion droplets, I expect defects to coincide with vertices in droplet shape, at which Gaussian curvature is concentrated. Simulations with extended shape flexibility would be an interesting extension.

While onset and number of vortices is predicted in the idealized case, subject

to local effects only, by Equation 3.46, with the additional effects of a larger field stiffness the problem becomes complex and simulation was needed to discover presence, number, and location of defects. Observations from simulations confirm and extend predictions made in Chapter 3, including the conditional accuracy of linear stability analysis and the existence of a vortex state.

Bibliography

[1] N. Metropolis, A. W. Rosenbluth, M. N. Rosenbluth, A. H. Teller, and E. Teller, J Chem Phys **21**, 1087 (1953).

[2] P. H. Garthwaite, Y. Fan, and S. A. Sisson, Commun Stat Theory Methods **45**, 5098 (2016), 1006.3690.

[3] H. Haario, E. Saksman, and J. Tamminen, Bernoulli **6**, 1035 (2015).

[4] G. O. Roberts and J. S. Rosenthal, Report No. 2, 2007 (unpublished).

[5] C. Andrieu and J. Thoms, Stat Comput **18**, 343 (2008).

[6] J. D. Chodera, J Chem Theory Comput **12**, 1799 (2016).

[7] J. D. Chodera, W. C. Swope, J. W. Pitera, C. Seok, and K. A. Dill, J Chem Theory Comput **3**, 26 (2007).

[8] M. R. Shirts and J. D. Chodera, J Chem Phys **129**, 124105 (2008).

[9] P. M. Chaikin and T. C. Lubensky, *Principles of condensed matter physics* (Cambridge university press Cambridge, 1995).

[10] F. Smallenburg and H. Löwen, J Chem Phys **144**, 164903 (2016).

[11] J. O. Law, A. G. Wong, H. Kusumaatmaja, and M. A. Miller, Mol Phys **116**, 3008 (2018).

[12] J. O. Law, J. M. Dean, M. A. Miller, and H. Kusumaatmaja, Soft Matter **16**, 8069 (2020).

[13] P. Fonda, M. Rinaldin, D. J. Kraft, and L. Giomi, Phys Rev E **98**, 032801 (2018), 1806.09596.

[14] M. Rinaldin, P. Fonda, L. Giomi, and D. J. Kraft, Nat Commun **11**, 4314 (2020), 1804.08596.

[15] F. Paillusson, M. R. Pennington, and H. Kusumaatmaja, Physical Review Letters **117**, 058101 (2016).

[16] N. Ramakrishnan, P. S. Kumar, and J. H. Ipsen, Phys Rev E **81**, 041922 (2010).

[17] A. G. Hansen, N. Ramakrishnan, P. B. Sunil Kumar, and J. H. Ipsen, The European Physical Journal E **40**, 32 (2017).

[18] L. A. Hoffmann, L. N. Carenza, J. Eckert, and L. Giomi, Sci Adv **8**, eabk2712 (2022).

[19] O. Marin, M. Tkachev, E. Sloutskin, and M. Deutsch, Curr Opin Colloid Interface Sci (2020).

CHAPTER 5

Solid-stabilized emulsions: Experimental systems

Abstract

Two experiments on solid-stabilized emulsions were carried out early in the project. Imaging of a microparticle-stabilized emulsion confirms the occurrence of hexatic order in this system. Experiments in forming more complex emulsion-like materials through specialized mixing protocols highlight the importance of wetting properties and formation dynamics. Along with the literature, the experiments contribute to understanding the system and motivate the choices made in the specific model examined in the Chapter 6.

5.1 Experiment: Model emulsion with close-packed particles

Several experiments have been performed on the geometric arrangement of colloidal particles on a sphere or other curved interfaces. As motivated in Chapter 1, while locally particles tend to form hexatic arrangements, a globally defect-free hexatic order is incompatible with a spherical topology. For hexatic order, twelve topologically mandated defect sites, particles with only five neighbors, must exist on a sphere. Theory and experiments further indicate that the twelve topological defect sites will be spaced at maximal distances in a icosahedral arrangement and that additional defects, in oppositely-charged pairs, occur. Usually, particles with long-range repulsive electrostatic interactions are used in experiments at interfaces, resulting in a widely-spaced lattice of isolated particles. Using this system, the ordering of particles on a spherical droplet was first examined by Bausch *et al.* [1] and the resulting arrangement was found to be largely a hexagonal crystal, with regularly placed 'grain-boundary scar' lines of defects. Irvine et al. used this system to study defects on spherical and catenoid surfaces [2, 3]. Corresponding simulations were carried out by Bendito et al [4], among others.

In previous experiments, the particles interactions are dominated by long-range electrostatic repulsion (presumably mediated through the oil phase [5]), resulting in a widely-spaced array of particles. The systems are clearly not jammed; a certain pattern of hexatic order arises in freely rearranging particles. However, it is doubtful whether the same widely-spaced array of electrostatically repulsive particles can stabilize an emulsion.

I here investigated whether more densely packed microparticles, which stabilize emulsion droplets, form similar hexatic order. My experimental model system is a simple Pickering emulsion consisting of decalin (decahydronaphthalene), index-matched water, and PMMA-PHSA microparticles. The chosen particles consist of a PMMA ((poly(methyl methacrylate)) polymer core, stabilized with a PHSA (poly(12-hydroxystearic acid)) polymer brush with the intention of replicating hard-sphere interactions. Einert et al [6] have similarly investigated grain boundary scars in a model Pickering emulsion, imaging ac-

cessible top and bottom sections of a spherical droplet. I here apply recent image analysis methods to extend analysis to the complete spherical surface.

5.1.1   Materials and methods

Flourescently labelled PMMA-PHSA microspheres were manufactured in-house by Andrew Schofield. For these micron-scale spherical particles, the core is the polymer polymethylmethacrylate (PMMA), while the surface is functionalized with a PHSA polymer brush, creating a short-distance barrier that prevents two particles from aggregating. The extent to which these particles approximate ideal hard spheres, or not, is discussed in [7] and, for particles in a liquid-liquid interface, in [8]. The particles are monodisperse with mean diameter $1.2\mu m$.

The PMMA microparticles were received in decalin, in which they form a sediment. Decalin was also chosen as the oil phase of the emulsion because its refractive index, 1.48, roughly matches that of PMMA (1.49).

To create the oil phase of the emulsions, $3g$ of decalin is first added to a vial. Then $0.2g$ of the PMMA microparticles, taken from the sedimented part of the microparticle-in-decalin stock, is transferred into the vial. The resulting suspension of microparticles in decalin mixture is sonicated using an ultrasound probe for one minute with the intention of removing any particle aggregation.

In another vial, sodium iodide ($.625g$) and water ($.375g$) are mixed. At this concentration, a solution of sodium iodide in water is just below saturation and has a refractive index of about 1.49 [9], close to that of decalin and PMMA.

Finally the decalin-particle mixture and the index-matched water are brought together to produce a water-in-oil emulsion. $1.5g$ of the decalin-particle mixture is placed in a vial, then $0.5g$ of the water-sodium iodide solution is added. The mixture is then sonicated for three to five 5-second pulses. Emulsion formation is visible as the precipitation of a floccular, yellow sediment of particle-coated water droplets. A drop of the resulting emulsion is transferred into a small vial of decalin, diluting the emulsion.

This final product, a diluted water-in-oil emulsion, can be stored under slow mixing on a roller bank for hours or days. In fact, this aging process may help reduce particle bridges [10]. The oldest sample imaged here was stored for two weeks, with no apparent detrimental changes.

As no surfactant was added, the model solid-stabilized emulsion is stable under the action of microparticles only.

Spherical droplets of varying sizes, from microparticle clusters of around $1\mu m$ to large droplets of about $300\mu m$, were observed. I scanned the smallest spherical droplets only due to time and space limitations of the confocal microscopy scan; the set of imaged droplets is not representative of the true size distribution in the emulsion.

5.1.2   Microscopy and image analysis

The sample is imaged with a laser scanning confocal fluorescence microscope (Zeiss LSM 700). A drop of the sample is placed on a glass cover slip. As the sample is not density-matched, particle-coated water droplets sit just above the glass surface. After about five minutes, deformation of the droplets becomes apparent, partially due to gravity but mostly due to diffusion and evaporation of the water phase into the air. Therefore a new drop of the sample must be used after a few minutes.

The emulsion contains droplets of varying sizes, dominated by large droplets, and a few coalescing, collapsed, or elliptical droplets. I here scanned only droplets that are small ($R = 1 - 15\mu m$), spherical, and not deformed by attachment to the glass surface or to other droplets. When a suitable droplet is found, a three-dimensional scan is taken using a 63x oil immersion objective.

Images are three dimensional image stacks with a voxel size of about $0.0625\mu m \times 0.0625\mu m \times 0.25\mu m$. The z-direction resolution is poor.

Images are analysed using PERI, an image reconstruction software based on Bayesian likelyhood estimation [11]. The software extracts the positions and radii of fluorescent spherical particles in the three-dimensional image by constructing an internal model - a list of particle positions and radii - that best explains the appearance of the image. The model is iteratively refined by comparing the image calculated from the optical effects of the model to the actual image. In a demonstrative experiment, the authors of [11] achieve nanometer-precision in the locations of colloidal microparticles, a substantial improvement over previous particle-tracking algorithms [12]. While the paradigm followed by the software is general, the existing implementation is conveniently optimized

for three-dimensional confocal micrographs of spherical colloidal particles.

When applied to solid-stabilized emulsion droplets, a major limitation is imperfect index matching. Lensing at oil-water, oil-PMMA, and water-PMMA interfaces distorts the image, although the problem has been significantly reduced by approximate index-matching. Therefore the ultra-high-precision particle locations obtained in the authors' demonstration are not achieved. While the software could theoretically be modified to take refraction at particle droplets and interfaces into account, I find that, after approximate index matching, all microparticles on the droplet surface are nevertheless identified and located with adequate precision.

After extracting all particle positions in a three-dimensional image, the list of particle coordinates is further filtered and modified: a spherical shell is fitted such that the area of sphere-microparticle intersections is maximized. This sphere is taken to represent the oil-water interface. The coordinates of particles not intersecting this sphere (i.e. freely suspended in the oil phase) are discarded. For particles intersecting the interface, the true position of the particle center, which may be slightly above or below the spherical shell, is adjusted by projecting radially onto the spherical surface. The projected particle positions all lie on the spherical shell of radius R (Figure 5.3). They can now also be represented as spherical polar coordinates $(\theta, \phi, \rho = R)$.

5.1.3 Quantifying order

From this list of particle coordinates on a sphere, I extracted two measures of the 'orderedness' of the particle arrangement: correlations in particle positions via the radial distribution function and defects identified via Voronoi tessellation.

Radial distribution function

The radial distribution function gives the average density of a substance as a function of distance from a point. Crystalline states can be distinguished from liquid phases by the strength and number of peaks in the radial distribution function, which indicate correlations in particle position.

My procedure for extracting the radial distribution function for points on a sphere is as follows:
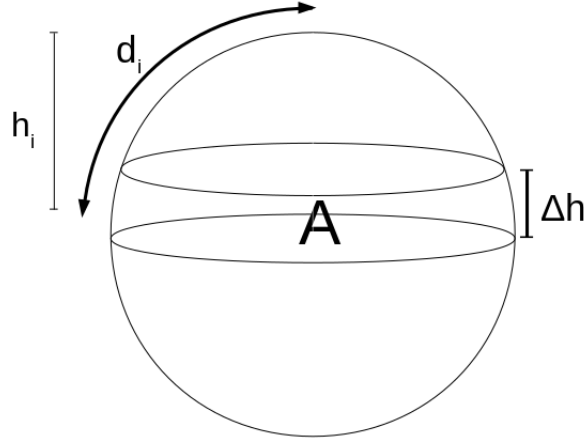
Figure 5.1: Height and surface area of an annulus on a spherical surface. The ith segment can be labelled by the z-direction distance h_i from the top of the sphere, but the distance from a reference particle at the top of the sphere to particles on each spherical segment is more appropriately given by the geodesic distance d_i.

A particle is selected as the reference particle. The system is rotated so that the chosen particle lies at the top of the sphere.

Conveniently, the surface area of a spherical segment (Figure 5.1) is proportional to the height Δh of the segment:

$$A = a\pi R\Delta h \tag{5.1}$$

Thus particles can simply be binned according to the value of their z-coordinate in the rotated system to form equal-area bins.

In addition to the height h_i of its center, each sphere segment is assigned a distance d_i, which measures the geodesic distance (along the surface) from the chosen particle to the bin center. Thus a list of particle counts at discrete distances d_i from the reference particle is generated.

Each particle is in turn chosen as the reference particle. For each particle, the system is rotated and the number of particles in each height interval Δh, located at height h_i, is counted.

Finally the counts obtained from different reference particles are averaged. They are also normalized according to the surface area of the chosen sphere segments and the average particle density on the droplet.

When the results are plotted (Figure 5.2), we see to what extent particle positions are correlated at larger particle separations.
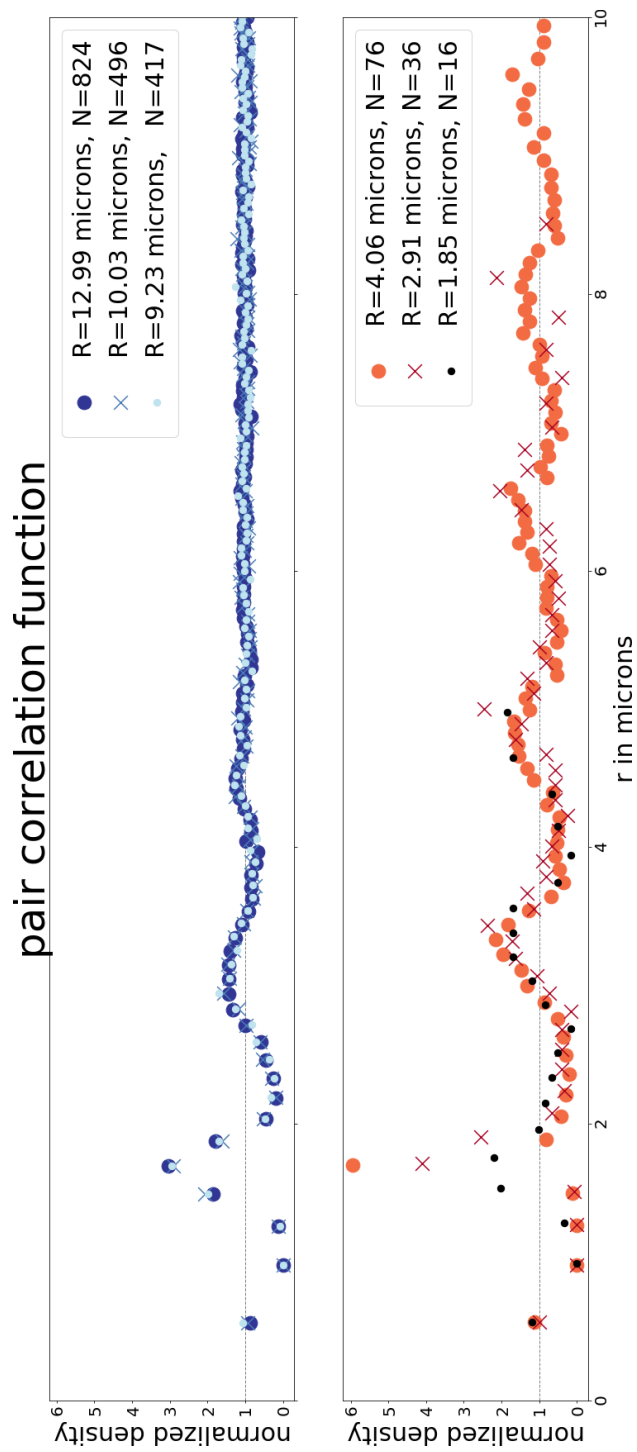
Figure 5.2: Selected radial distribution functions on droplets with radius R and N interfacial microparticles. Large droplets have liquid-like particle arrangements while on small droplets, peaks persist over the entire particle surface.

The scanned droplets seem to fall into one of the two distinct types: large droplets ($R \gtrsim 4.5\mu m$) with liquid-like pair correlation functions, and small droplets with peaks in the radial distribution function persisting until the end of the surface. However, only 14 droplet were analyzed in this exploratory experiment. For reference, the radial distribution of similar particles at a planar interface [8] is intermediate between the two types seen here. On large spherical droplets liquid-like positional order seems disrupted in comparison to order on a plane, while particles on small droplets seem counterintuitively more ordered. A small number of spherical particles ($N \leq 80$) seem to arrange into a spherical shell in a symmetric and structured way, with a clear cutoff between the two cases at a droplet radius of about $4.5\mu m$. The distinction has not been previously reported in the literature, as relatively larger droplets with a larger number of interfacial particles are usually studied. The apparently discontinuous transition from the regime of sphere packing in a small cluster or surface to the arrangement of a large number spheres on a spherical surface is an interesting topic for further study.

Voronoi tessellation

Voronoi tessellation divides an area into cells such that each point is categorized by its closest particle center. The Voronoi tessellation is here used to measure how many neighbours each particle has.

Voronoi tessalation was originally defined for distances on a plane. However, on a spherical surface, it has been shown that an equivalent tessalation is achieved by projecting patches of the surface onto a plane, then using the standard algorithms for Voronoi tessalation on a plane. I here used the scipy implementation of Voronoi tessalation on a sphere, based on an algorithm by Caroli et al. [13].

Examining the particles as categorized as hexagons or defects by Voronoi tessalation (Figure 5.4), I found that 5- and 7-fold defects are arranged in lines called grain-boundary scars, as is known in the experimental literature. While a variety of defect motifs are possible and emerge according to size and curvature of the system, including isolated defects (disclinations), defect pairs (dislocations), lines, and rosettes [14, 15], here, irregular lines of defects are
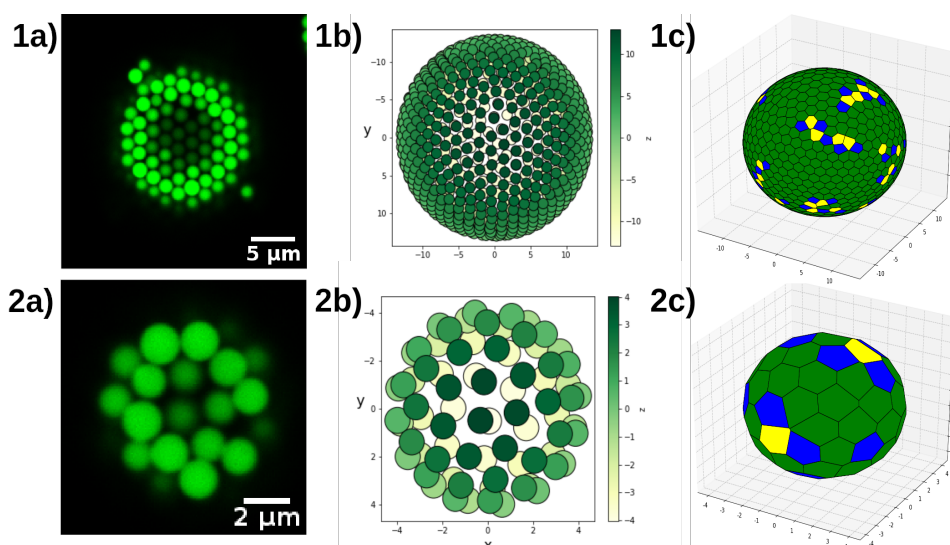
Figure 5.3: The process of image analysis, from confocal micrograph to Voronoi tessellation. (a) Example slice from the three-dimensional stack of confocal scans. (b) Particle positions, extracted from the confocal data using PERI and filtered for particles lying on a sphere (c) Voronoi tessellation of particle positions on a sphere, distinguishing particles with six, five, or seven neighbors.

predominantly seen. The defect lines are also not arranged on the sphere with perfect icosahedral symmetry, also indicating some degree of incomplete global minimization. The same phenomenon of slightly irregular defect scar lines, deviating from the result of a theoretical zero-temperature minimization of the same system, is seen elsewhere in the experimental literature [6]. The result indicates that a qualitatively similar hexatic packing occurs in the model solid-stabilized emulsion as in experiments with electrostatically repulsive particles, despite the denser packing of the microparticles. The microparticles in my model Pickering emulsion are not jammed locally, as evidenced by their arrangement into a locally hexatic rather than glass-like monolayer. At the same time, the microparticle monolayer effectively stabilizes the emulsion.
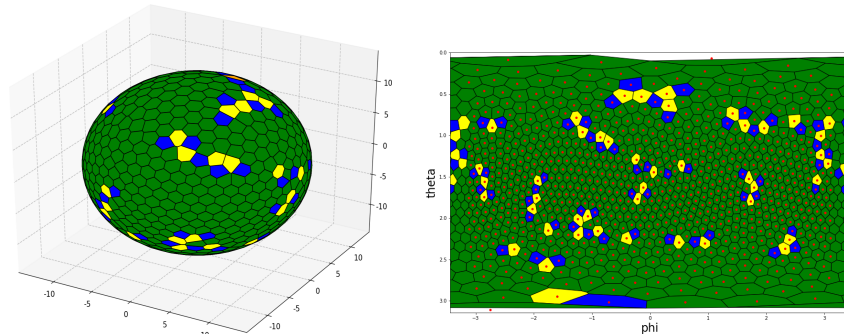
Figure 5.4: Voronoi tessellation of particles on the largest droplet, on a sphere and projected onto a plane. Hexagonal tiling (green) predominates. The arrangement of particles with five (blue) and seven (yellow) neighbors into defect lines replicates the existing literature.

5.1.4 Discussion

The model emulsion is designed to show that, at least in some cases, a stable emulsion with hexatic orientational ordering exists, albeit with the expected packing defects. On the other hand in other solid-stabilized emulsions, with rough, polydisperse, or interacting particles, jamming is a prominent effect and the arrangement of particles will be more irregular and glass-like. Pickering emulsions are commonly stabilized by force chains in a layer of jammed particles, among other mechanisms. The material is solid-like, with a surface stress in response to compression of the interface via an applied inner under-pressure in the droplet [16]. Furthermore, the interfacial material is hysteretic, with varying material properties after a history of compression and decompression [16]. Similarly, we can assume that in such cases the interfacial particle configuration is dependent on formation history. Jammed configurations and other nonequilibrium phenomena are not treated further in this thesis.

In this thesis I generally analyze order as a continuum field theory, rather than studying the packing of a small number of discrete spheres or circles on a curved space. In contrast, the experiment examined the positions of relatively few individual particles. As such, the results on larger droplets, bearing up to $N = 824$ microparticles, are more indicative of the behavior of interest. The somewhat large microscale particles were chosen due to their accessibility

to optical microscopy methods. We can assume that similar systems stabilized by smaller nanoparticles behave similarly, displaying predominantly hexatic arrangements with occasional grain boundaries scars.

5.2 Experiment: Bijels by mixing

Secondly, I performed an experiment on creating metastable complex bijel-like droplet shapes in nanoparticle-stabilized emulsion.

The bijel is a complex emulsion-like material with an amorphous bicontinuous morphology. It is of interest here because the particle-coated interface separating the oil and water phases has a complex shape with high topological genus and varying curvature. Bijels can be reliably produced by the symmetric demixing of two immiscible liquids under the addition of nano- or microparticles. As the liquids undergo spinodal decomposition, the particles are absorbed into the emergent interface and stabilize it, preventing further demixing. Thus the mutually interpenetrating structure of the two liquids which is usually transiently observed during spinodal decomposition is 'frozen in', held in place by the jammed layer of particles at the interface. These bijels can be stable in this nonequilibrium state for months.

Here I aimed to produce a similar result, a complex tortuous strucutre of mutually interpenetrating liquids, by simply mixing viscous liquids at room temperature, a procedure which would be more scalable and generalizable than the original method. Protocols for producing bijels in this way were first discovered simultaneously by Cai *et al.* [18] and Huang *et al.* [19]. I attempted to replicate the experiment by Cai *et al.*

The model bijel-like emulsion consists of silica particles; the water-like but more viscous glycerol as the aqueous phase; silicone oils of varying viscosity as the oil phase; and the additional surfactant CTAB, which modifies the wetting properties of the particles. The monodisperse spherical nanoparticles were manufactured via the Stöber process [20]. To enable confocal microscopy, the glycerol phase is labelled with Nile Red and the nanoparticles incorporate FITC (fluorescein isothiocyanate).

The protocol recommended by Cai *et al.* features a certain sequence and
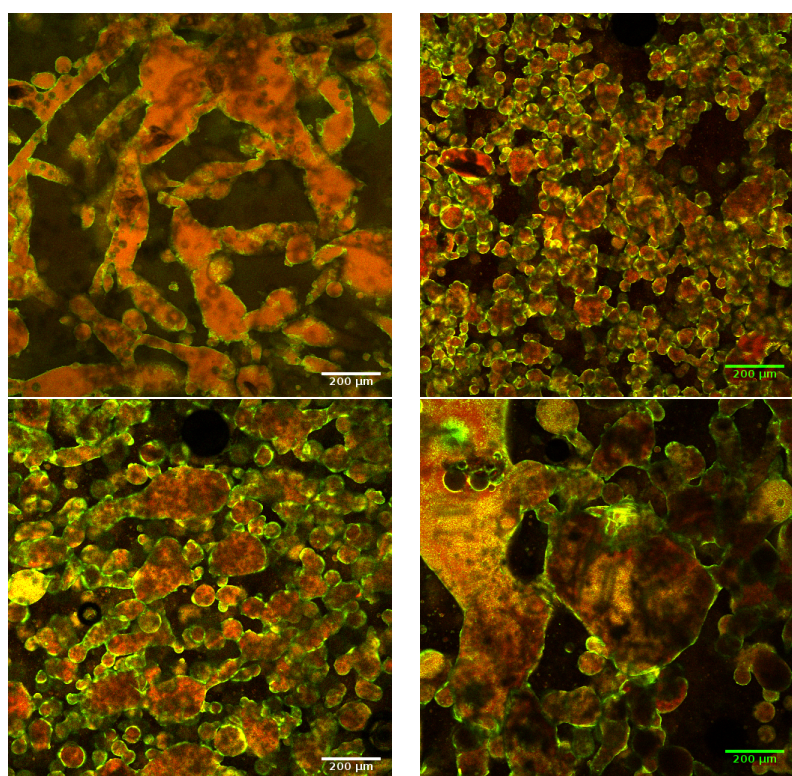
Figure 5.5: Partially inverted emulsion samples, method as in [17]. Glycerol is dyed red, oil is left dark, and silica nanoparticles are green. Elongated, branched, and interconnected droplets structures occur.

timing of mixing steps with a magnetic stirrer and pauses. Despite using the same equipment and material as the original authors, the experiment could not be replicated. I concluded that this is due to the degraded wetting properties of the silica nanoparticles used: wetting propoerties are crucial to determining whether an emulsion, bijel, or inverse emulsion is formed [20]. However, a variant protocol by Li at al. [17] [1], which takes advantage of off-neutral hydrophilic nanoparticles, could be replicated. I produced samples of elongated, branched, or interconnected emulsion droplets with this method (Figure 5.5).

The hypothesized mechanism is a conflict between the emulsion type favored by the relative fluid viscosities during formation, a water-in-oil emulsion, and the wetting angle of the nanoparticles, which favor an oil-in-water emulsion. In the proposed mechanism, the emulsion begins to invert during formation, but the partially inverted morphology is 'frozen in' by jamming of the interfacial nanoparticle layer and potentially by the high viscosity of the fluids [17].

5.2.1 Discussion

The sensitivity of different bijel formation methods, whether by spinodal decomposition or by mixing, to nanoparticle wetting angle [20] implies that interfacial spontaneous curvature effects are important. Additionally, the dynamics and relative timings during the formation process are crucial [21], as are rheological properties of the interfacial material thus formed [22]. For the several formation methods, several mechanism are proposed but not all are conclusively known. The interplay of dynamic qualities such as viscosity is beyond the scope of this thesis.

In classic bijels, most channel breakage and bijel failures seem to happen during the formation process. Once successfully formed, bijels are extremely stable. Based on macroscopic rheological measuements, particles in aged bijels appear to rearrange into a more compact [23] (and potentially more hexatic) configuration and develop interfacial attractions.

A fundamental limitation is that bijels produced with either method are not easily extended to larger particles such a microparticles. In addition to

---

[1]While I am an author on this publication, my contribution consists of the image analysis algorithm and does not overlap with material presented in this thesis.

dynamic formation effects [21], there is fundamentally an upper limit due to area-volume scaling of the particles. To cover the same amount of interfacial area with their cross sections, larger microparticles would need to be dissolved in the initial oil phase at a extremely high volume fraction, making the initial dispersion of particles in oil impossible or difficult to process. This presents us with an experimental problem in imaging interfacial order in bijels or at tube-like interfaces. Only nanoparticles stabilize bijels formed by mixing, while micron-scale particles are required to resolve individual particle locations by fluorescence confocal or other optical microscopy methods. A promising future experiment would be to examine the arrangement of small nanoparticles on the surfaces of a bijel formed by spinodal decomposition with cryo-SEM or other nanoscale imaging methods.

5.3   Nanorod-stabilized emulsions and bijels

Beyond spherical interfacial particles, emulsions can be stabilized by a range of other particle shapes. Indeed, in industrial contexts stabilizing particles are rarely monodisperse or perfectly spherical. Variants include irregular particles as well as the plate-like particles in clays. Returning to lab-based model emulsions, nanorods can be used to stabilize emulsions [24, 25]. While difficult, bijels have also been formed using rod-like nanoparticles [26]. Practical challenges in bijels include the difficulty in tuning wetting properties of the rod-shaped nanoparticles and challenges in imaging samples with iron-oxide-based nanorods. Formation dynamics may proceed according to the particles' longer dimension, as if the particles are larger. Surface curvature on a scale comparable to individual rod length may facilitate particle detachment. Lastly rods may be less conducive to jamming and force chains. Ellipsoidal particles are prone to arrange in triangle-like clusters due to capillary interactions.

Nevertheless, rod-like nanoparticles are an attractive object of study in the context of this thesis. Experiments on planar as well as spherical interfaces, show distinct isotropic and orientationally ordered (nematic) phases. Li *et al.* [27] studied interfacial monolayers of spherocylinders under compression in a Langmuir trough experimentally and computationally. In both cases the ordered

phase consists of several small ordered domains or rafts, each consisting of a small number of particles. The authors note single vertical 'flipper' particles as pressure is increased. However, rather than representing a dinstinct phase of the material, the phenomenon seems confined to individual particles located between nematic grains. Although observations on a planar interface may not be indicative of behavior in emulsions [28], the possibility of a 'flipper' phase of predominantly vertical particles will be neglected. Additionally, Li *et al*. note that double-layers occur under higher compression. This limit will not be considered. Lastly when the scale of individual rods becomes comparable to curvature, attachment energy is modified; rod orientation and mean curvature plays a role; and interparticle capillary forces may be modified. In this thesis I will model an idealized interfacial monolayer layer of nanorods as a two-dimensional material, assuming particles are small relative to surface curvature and lie parallel to the surface.

5.4 Conclusions

By analyzing microparticle-stabilized emulsion droplets, I investigated whether well-known experimental phenomena of hexatic packing and defect scars on spheres also occur in the more densely packed particle layers required to effectively stabilize an emulsion. I find that the phenomenon occurs in my model solid-stabilized emulsion, confirming findings by Einert *et al*. [6]. Previous studies capture sections of spherical droplets, inferring the full conformation via statistical analysis [6]. Using confocal microscopy and recent computational image analysis methods, I was able to directly determine the positions of all particles over the three-dimensional spherical surface of small droplets. An extension to larger three-dimensional objects is constrained by space and time constraints of scanning confocal microscopy on solid-stabilized emulsion droplets. Larger spherical systems subject to the same principles have been analyzed in other studies [29]. The emulsion can be expected to behave like these other systems at larger droplets sizes, that is developing 'seas' of hexatic order separated by defect scars, arranged in an icosahedral pattern.

The observation of local hexatic order implies that in this model emulsion,

the closely-packed particles are not jammed but free to rearrange locally. The observed long-term stability of emulsion droplets in a vial of decalin, opposed to the rapid collapse of droplets on a microscope slide, implies that these droplets are nevertheless stable against the Laplace pressures differences involved in usual Ostwald ripening between droplets, but not against the evaporation of water to the surrounding air.

Experiments on the dynamic formation of complex bijel-like emulsion droplets highlighted the importance of particle wetting angle or interfacial spontaneous curvature. The experiments, which rely on fluid viscosities and the timings of various effects during the formation process, also highlight the importance of dynamic phenomena and hysteresis in determining emulsion morphology. Dynamics and the mixing process are beyond the scope of this thesis; instead a certain metastable emulsion morphology is presupposed in the analysis of the shape and stability of individual channels.

The two experiments presented here and others in the literature give direction on how to modify the previous, generic model to best represent solid-stabilized emulsions:

Spontaneous curvature, based on wetting properties of the particles, is indeed a crucial effect and will be retained. While a surface tension based on the free interfacial area between particles is present, surface tension alone is an inadequate description of the system.

The constraints on particle number and surface area in solid-stabilized emulsion differ qualitatively from the molecular mono- and bilayers of molecules at interfaces discussed in previous chapters. An interfacial material of molecular surfactant is in chemical equilibrium with a reservoir of the same molecule dissolved in the bulk. While the total number of molecules on the interface is approximately constant, individual molecules are constantly exchanged between interface and solvent. On the other hand, larger nano- or microscale particles can be assumed to be to be irreversible adsorbed to the interface. After formation of a droplet, the total number of particles on the interfaces is constant. The particle-stabilized interface is subject to a surface tension from the bare interface between particles. Surface area decreases and particles are brought into closer contact until the particle density becomes sufficiently high. Then the op-

posite effect, a pressure of the particle layer which prevents further compression, comes into effect.

In the next chapter, the need to conserve total particle number motivates the adoption of a model which describes both local number density and orientational order. Focusing on a model interfacial material of two-dimensional nanorods, in the next chapter I derive the material properties of a nanorod monolayer to replace the previously generic description of the order parameter field.

Bibliography

[1] A. Bausch *et al.*, Science **299**, 1716 (2003).

[2] W. Irvine, V. Vitelli, and P. M. Chaikin, Nature **468**, 947 (2010).

[3] W. Irvine, M. J. Bowick, and P. M. Chaikin, Nat Mater **11**, 948 (2012).

[4] E. Bendito, M. J. Bowick, A. Medina, and Z. Yao, Phys Rev E **88**, 012405 (2013).

[5] T. S. Horozov, R. Aveyard, J. H. Clint, and B. P. Binks, Langmuir **19**, 2822 (2003).

[6] T. Einert, P. Lipowsky, J. Schilling, M. J. Bowick, and A. R. Bausch, Langmuir **21**, 12076 (2005).

[7] C. P. Royall, W. C. Poon, and E. R. Weeks, Soft Matter **9**, 17 (2013).

[8] I. Muntz *et al.*, Phys Rev Research **2**, 023388 (2020).

[9] K. Bai and J. Katz, Exp Fluids **55**, 1 (2014).

[10] D. J. French *et al.*, Sci Rep **6**, 1 (2016).

[11] M. Bierbaum, B. D. Leahy, A. A. Alemi, I. Cohen, and J. P. Sethna, Phys Rev X **7**, 041007 (2017).

[12] B. D. Leahy, N. Y. Lin, and I. Cohen, Curr Opin Colloid Interface Sci **34**, 32 (2018).

[13] M. Caroli *et al.*, Robust and efficient delaunay triangulations of points on or close to a sphere, in *International Symposium on Experimental Algorithms*, pp. 462–473, Springer, 2010.

[14] D. J. Wales, H. McKay, and E. L. Altschuler, Physical Review B **79**, 224115 (2009).

[15] H. Kusumaatmaja and D. J. Wales, Phys Rev Lett **110**, 165502 (2013).

[16] P. J. Beltramo *et al.*, Proc Natl Acad Sci USA **114**, 10373 (2017).

[17] T. Li, J. Klebes, J. Dobnikar, and P. S. Clegg, Chem Comm **55**, 5575 (2019).

[18] D. Cai, P. S. Clegg, T. Li, K. A. Rumble, and J. W. Tavacoli, Soft Matter **13**, 4824 (2017).

[19] C. Huang *et al.*, Nature Nanotechnol **12**, 1060 (2017).

[20] K. A. White *et al.*, J Colloid Interface Sci **359**, 126 (2011).

[21] M. Reeves, A. Brown, A. B. Schofield, M. Cates, and J. Thijssen, Phys Rev E **92**, 032308 (2015).

[22] J. H. Thijssen and J. Vermant, J Phys Condens Matter **30**, 023002 (2017).

[23] L. Bai, J. W. Fruehwirth, X. Cheng, and C. W. Macosko, Soft Matter **11**, 5282 (2015).

[24] K. R. Peddireddy, T. Nicolai, L. Benyahia, and I. Capron, ACS Macro Letters **5**, 283 (2016).

[25] X. Yue, X. Liu, N. Yan, and W. Jiang, J Phys Chem C **124**, 20458 (2020).

[26] N. Hijnen, D. Cai, and P. S. Clegg, Soft Matter **11**, 4351 (2015).

[27] T. Li, G. Brandani, D. Marenduzzo, and P. Clegg, Phys Rev Lett **119**, 018001 (2017).

[28] K. A. Macmillan and P. S. Clegg, J Phys Chem Lett **12**, 5241 (2021).

[29] R. E. Guerra, C. P. Kelleher, A. D. Hollingsworth, and P. M. Chaikin, Nature **554**, 346 (2018).

CHAPTER 6

Hard-rod fluid on a modulated cylindrical interface

Abstract

In this chapter I adapt the previously generic model to a specific interfacial material, a two-dimensional hard rod fluid. Analytic results from Fundamental mixed measure theory, a density functional theory, are taken from the literature or derived where applicable to form a local description of the material. To this end I obtain Frank constants K_ϵ as well as the additional coefficients J_ϵ, moduli of density variation. In the proposed gas-like model material, curvature-coupled gradient energies are small; the dominant effect is homogeneity of the fluid due to entropic effects. Tubule shape and stability is primarily determined by surface tension-bending rigidity effects; orientational order adapts to the resulting surface shape. Finally the simulation is adapted to confirm configurations of the order parameter field on the curved surface.

Table 6.1: Table of symbols, Chapter 6

symbol	meaning
D	width (diameter) of particles
L	length of particles
l	aspect ratio of particles
A	particle area
$\mathbf{n} = (n_x, n_z)$	unit normal vector to particle boundary
ρ	particle number density
η	area fraction covered by particles
R	total number of particles in the system
$\hat{n}$	unit director
$\hat{m}$	complex director
ϑ	angle of complex director
ϕ	orientation of an individual particle
$g(\alpha^2, \phi)$	distribution of particle orientations ϕ around $\hat{n}$
α^2	sharpness of angle distribution, an indicator of order
S	a derived scalar order parameter
$\mathbf{r} = (x, z)$	position in general (flat space) theory
$\mathbf{x} = (z, \theta)$	position on the cylinder-like interface
n_ν, N	weighted density functions
$\omega^{(\nu)}, \Omega^{(\mu\nu)}$	weight functions
$\bar{\omega}$	certain single-body integrals over weight functions
K_ϵ	Frank constants, elasticity w.r.t. gradients in director
J_ϵ	elasticity w.r.t gradients in density

6.1 Orientational order in a hard-rod fluid

6.1.1 Density functional theory

With density functional theory (DFT), otherwise intractable properties of N-body fluids can be calculated computationally. Fundamental measure theory (FMT), first developed by Rosenfeld [1, 2], extend DFT to interactions between multiple species of hard spheres via a geometrical interpretation of the Mayer f-function. Further extentions of FMT include Fundamental mixed measure theory (FMMT) [3], which handles convex hard bodies of arbitrary shape. Among other applications, Wittmann *et al.*[4] have used fundamental mixed measure theory to reveal density distributions and phase behaviour in a two-dimensional fluid of hard discorectangles. While the framework primarily provides computational results, in certain special cases analytic solutions are possible. In this chapter I will make extensive use of analytical formulae relating order parameter, number density, and energy retrieved by Wittmann *et al.* [4] in the special case of isotropic and nematic phases of a the two-dimensional hard rod fluid. Additionally, I re-work Wittmann and colleagues' work on the elasticity of nematics in three dimensions [5] for the two-dimensional case and calculate an additional elasticity coefficient to retrieve bending rigidities of the two-dimensional nematic material. The results from FMMT at the microscopic scale will be taken as material properties of the interfacial material and incorporated into the investigation of order on a curved surface.

As in [4], I examine use a fluid of hard discorectangles (Figure 6.1), the two-dimensional version of a spherocylinder. The discorectangle is characterized by diameter D and length L. In units of the radius r_0 of the larger cylindrical surface on which the particles are embedded, these lengths will be small. The particle has unitless aspect ratio $l = L/D$ and area $A = LD + \pi D^2/4$.

As is conventional in DFT, energy of the material has ideal gas ('id') and excess ('ex') contributions.

The total energy is

$$F = \int d\vec{r} \left(f_{id} + f_{ex} + f_{grad} \right);$$ (6.1)

The excess energy density $f_{ex}(\mathbf{x})$ gives the energy of a configuration due to two-body interactions, in this case excluded volume interactions.

Figure 6.1: The two-dimensional discorectangle particle shape, a rectangle with half-disc end caps, and its dimensions L, D.

The excess free energy is approximated by

$$f_{ex}(\rho(\mathbf{r})) = -n_0 \ln(1 - n_2) + \frac{N}{2(1 - n_2)}, \tag{6.2}$$

an extension of Onsager theory to higher area fraction [4], derived by dimensaional analysis and by matching to thermodynamic equations of state [2].

The energy density is a function of weighted densities

$$n_\nu(\mathbf{r}) = \int d\mathbf{r}' d\phi \rho(\mathbf{r}', \phi) \omega^\nu(\mathbf{r} - \mathbf{r}', \phi), \tag{6.3}$$

in turn based on the weight functions $\omega^{(\nu)}$:

$$\omega^{(2)}(\mathbf{r}, \phi) = \Theta(|\mathbf{R}(\hat{\mathbf{r}}, \phi)| - |\mathbf{r}|)$$
$$\omega^{(1)}(\mathbf{r}, \phi) = \frac{\delta(|\mathbf{R}(\hat{\mathbf{r}}, \phi)| - |\mathbf{r}|)}{\mathbf{n}(\hat{\mathbf{r}}, \phi) \cdot \hat{\mathbf{r}}} \tag{6.4}$$
$$\omega^{(0)}(\mathbf{r}, \phi) = \frac{K(\hat{\mathbf{r}}, \phi)}{2\pi} \omega^{(1)}(\mathbf{r}, \phi)$$

where ϕ is the orientation of the particle; $\hat{\mathbf{r}}$ is the unit direction vector of $\mathbf{r}$; $\mathbf{R}(\hat{\mathbf{r}}, \phi)$ is the vector from the origin to the particle boundary in a given direction $\hat{\mathbf{r}}$; and $\mathbf{n}(\hat{\mathbf{r}})$ is the (outwards-pointing) unit normal vector to the particle boundary at the location indicated by $\mathbf{R}(\hat{\mathbf{r}}, \phi)$. The weight functions are kernels of integration related to particle area, particle perimeter, and total curvature along the particle boundary respectively. The integral is over all possible orientations ϕ of the central particle as well as over space $\mathbf{r}$.

Furthermore there are vector and tensor versions of $\omega^{(\nu)}$ and of derived number densities n_ν, formed by including factors of the unit normal $\hat{n}$ in Equations 6.4 6.3. I will use vector $\underline{\omega}^{(1)} = \mathbf{n}\omega^{(1)}$ and tensor $\underline{\underline{\omega}}^{(1)} = \mathbf{n}\mathbf{n}^T \omega^{(1)}$, objects with two and 2×2 components respectively.

Additionally N is the two-body weighted density

$$N(\mathbf{r}) = \int \int d\mathbf{r}_1 d\phi d\mathbf{r}_2 d\phi_2 \rho(\mathbf{r}_1, \phi) \rho(\mathbf{r}_2, \phi_2) \Omega^{(11)}(\mathbf{r} - \mathbf{r}_1, \phi_2, \mathbf{r} - \mathbf{r}_2, \phi_2) \quad (6.5)$$

related to the two-body weight functions

$$\Omega^{(11)}(\mathbf{r}) = \frac{\arccos(\mathbf{n}_1 \cdot \mathbf{n}_2)}{2\pi} |\mathbf{n}_1 \times \mathbf{n}_2| \omega^{(1)}(\mathbf{r}_1, \phi) \omega^{(1)}(\mathbf{r}_2, \phi_2) \quad (6.6)$$

with $\mathbf{n}_i$ the normal vector $\mathbf{n}(\hat{r}_i, \phi_i)$ at each particle's boundary. By expanding $\arccos(\mathbf{n}_1 \cdot \mathbf{n}_2)|\mathbf{n}_1 \times \mathbf{n}_2|$, N is approximated as a series expansion [4]

$$N = \frac{2+b}{6\pi} n_1 n_1 + \frac{b-4}{6\pi} \underline{n}_1 \cdot \underline{n}_1 + \frac{2-2b}{6\pi} Tr[\underline{\underline{n}}_1 \underline{\underline{n}}_1] + ... \quad (6.7)$$

The series does not formally converge in even numbers of dimensions [4, 6]; here the series is truncated at rank-2 tensors, rendering it inaccurate. Therefore, the algebraic values of the coefficients in the series expansion are replaced with the above heuristic values including free parameter b [7]. The relationship between coefficients comes from the virial coefficients, reducing 3 coefficients to one free parameter. The remaining free parameter b is chosen reproduce some criterion. For example, Roth *et al.*[7] find that a value of $b = 11/4$ yields the best fit to the Mayer function of hard discs, while $b = 3$ best reproduces the bulk pressure of the hard-disc crystal. Wittman *et al.* [4] find $b = 3$ also reproduces excluded area well, while $b = 4$ is a good choice in the high aspect ratio limit. Wittmann *et al.*, and this work, will proceed with the choice $b = 3$.

While the task is in general to find the distribution $\rho(\mathbf{r}, \phi)$ in both location and orientation minimizing Equation 6.1, the form of the distribution of particles' orientations is posited throughout to be

$$g(\phi) = \frac{1}{I_0(\alpha^2)} e^{\alpha^2(2\cos^2\phi - 1)}, \quad (6.8)$$

a double-headed distribution with free parameter α^2 indicating sharpness of the distribution (Figure 6.2). The factor $I_0(\alpha^2)$, a modified Bessel function of the first kind, normalized the distribution to $\int_0^{2\pi} d\phi g(\phi) = 2\pi$. This form of the orientation distribution has been found to minimize the potential[8].

While α^2 indicates sharpness of the distribution or amount of order, the amount of order is more conventionally reported as the order parameter $S \in [0, 1]$, derived from α^2 as

$$S(\alpha^2) = \frac{1}{2\pi} \int_0^{2\pi} d\phi (2\cos^2\phi - 1)g(\phi)$$
$$= \frac{I_1(\alpha^2)}{I_0(\alpha^2)}. \tag{6.9}$$

With the energy formula in Equation 6.1 and the assumption in Equation 6.8 in hand, FMMT enables Wittmann *et al.* to computationally retrieve a spatially varying density distribution $\rho(\mathbf{r}, \phi)$ minimizing potential $\Omega = F - \mu N$. At a given area fraction and aspect ratio, isotropic, nematic, smectic, or crystalline density and order parameter distributions result. In two dimensions the authors report a phase diagram in aspect ratio $l = L/D$ and area fraction η encompassing isotropic, nematic, smectic, and crystalline phases. In the latter two phases, the particles have translational order, as evidenced by periodic variation in $\rho(\mathbf{r})$, while the former two phases are isotropic with respect to the positions of particle centers.

In the cases of the microscopically uniform-density phases, the isotropic and nematic phases, Equations 6.3 and 6.1 are particularly simple. Wittmann *et al.* additionally obtain analytical formulae for (a) orientational order and (b) energy density as a function of area fraction in the special cases of the isotropic and nematic phases. I here additionally derive expressions for (c) elasticity as a function of area fraction in two dimensions.

After positing a density distribution $\rho(\mathbf{r}, \phi) = \rho_0 g(\cos\phi)$ characterized by spatially uniform number density and spatially varying orientation, Equations 6.3 integrate to [4]

$$
\begin{aligned}
n_0 &= \rho_0, \\
n_1 &= \rho_0(2L + \pi D), \\
n_2 &= \rho_0(LD + \frac{\pi}{4}D^2) = \rho_0 A = \eta, \\
\underline{n}_1 &= \underline{0}, \\
\underline{\underline{n}} &= \rho_0 \begin{pmatrix} L(1+S) + \frac{\pi}{2}D & 0 \\ 0 & L(1-S) + \frac{\pi}{2}D \end{pmatrix}.
\end{aligned} \tag{6.10}
$$

The scalar number densities are proportional to total boundary curvature, perimeter, and area of a discorectangular particle respectively. The tensor components are additionally related to order parameter S.

Furthermore, by equating α^2 as defined as a derivative of the excess free energy density,

$$\alpha^2 := -\frac{\partial f_{ex}(\eta, S, l)}{\rho \partial S}. \tag{6.11}$$

with α^2 as defined by Equation 6.9,

$$S(\alpha) = \frac{I_1(\alpha^2)}{I_0(\alpha^2)} \approx \frac{1}{2}\alpha^2 - \frac{1}{16}\alpha^6. \tag{6.12}$$

Wittmann *et al.* [4] obtain a relationship between order and area fraction η:

$$\eta(\alpha^2) = \left(1 + \frac{8l^2(b-1)S(\alpha^2)}{3\pi(4l+\pi)\alpha^2}\right)^{-1}. \tag{6.13}$$

The formula directly indicates the isotropic-nematic phase transition, the area fraction $\eta_{IN}(l)$ at which the order parameter S vanishes,

$$\eta_{IN} = \lim_{\alpha \to 0} \eta(\alpha^2) = \left(1 + \frac{4l^2(b-1)}{3\pi(4l+\pi)}\right)^{-1}, \tag{6.14}$$

with b again a parameter which I set to $b = 3$. They find that (unlike in three dimensions) the transition is second order and there is no nematic-isotropic coexistence region.

Note that the series expansion in Equation 6.12, which is not accurate beyond $\alpha^2 \approx 1$ (Figure 6.4), has been used to derive these relations.

The ideal energy contribution reads

$$f_{id}(\mathbf{x}) = \frac{1}{2\pi} \int_0^{2\pi} d\phi \rho(\mathbf{r}, \phi)(\ln(\rho(\mathbf{r}, \phi)\Lambda^2) - 1), \tag{6.15}$$

with Λ the thermal wavelength of the particles, the value of which is however irrelevant. Since the number of particles in the system will be fixed, chemical-potential-like terms linear in ρ_0 can be ignored as they have no effect on system behavior. Substituting $\rho = \rho_0 g(\cos\phi)$ in the isotropic and nematic phases, the relevant parts of the ideal contribution are

$$f_{id}(\mathbf{x}) = \frac{1}{2\pi} \int_0^{2\pi} d\phi \rho(\mathbf{r}, \phi)(\ln(\rho_0) + \alpha^2(2\cos^2\phi - 1) - \ln(I_0(\alpha^2)))$$
$$= \rho_0(\ln(\rho_0) + \alpha^2 S + \ln(I_0(\alpha^2))). \tag{6.16}$$

Local energy density $f_{loc} = f_{ex} + f_{id}$ is a convex function of number density or area fraction (Figure 6.6). At constant system volume and area fraction,
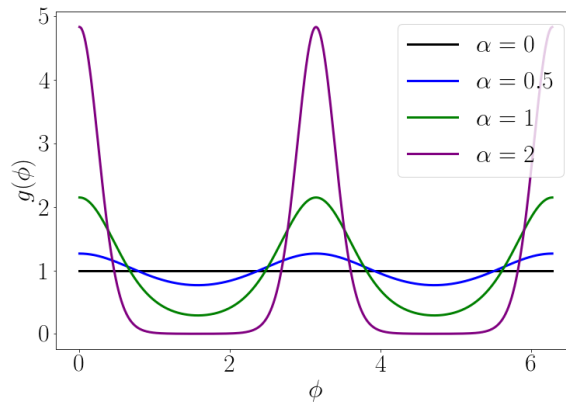
Figure 6.2: Angle distribution $g(\alpha^2, \phi)$. The distribution in Equation 6.8 is a double-headed distribution over possible particle orientations $\phi \in [0, 2\pi)$, with 'sharpness' determined by parameter α^2

(a) Functions S, $\bar{P}_4$ (see box 6.2.3).

(b) Series approximations of S.
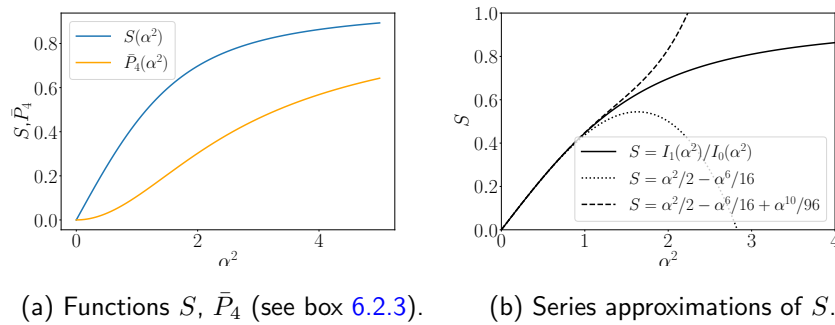
Figure 6.3: The order parameter $S(\alpha^2)$, a ratio of two Bessel functions $S = I_1(\alpha^2)/I_0(\alpha^2)$, compared to the similar function $\bar{P}_4 = I_2(\alpha^2)/I_0(\alpha^2)$ and compared to polynomial approximations.

(a) $\alpha^2(\eta)$ (b) $S(\eta)$
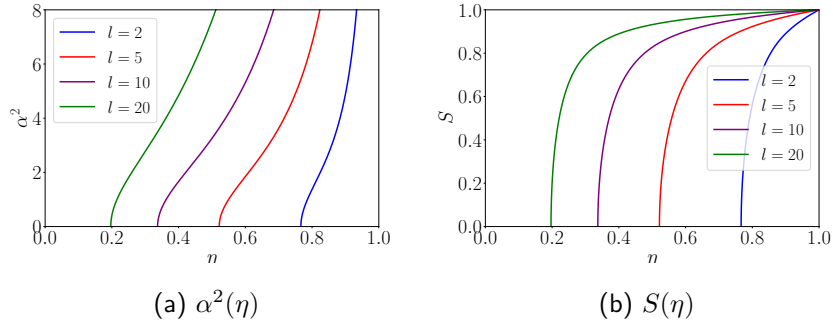
Figure 6.4: Relationship between particle area fraction η and two indicators of orientational order, 'sharpness' α^2 and order parameter S, shown for four particle aspect ratios l. The order parameters become nonzero at the critical area fraction $\eta_{IN}(l)$, where the isotropic-nematic transition takes place; subsequently orientational order increases with area fraction. Derived order parameter S is often a more useful quantity in calculations, as it is finite and bounded to $S = 1$ at high orientational order.
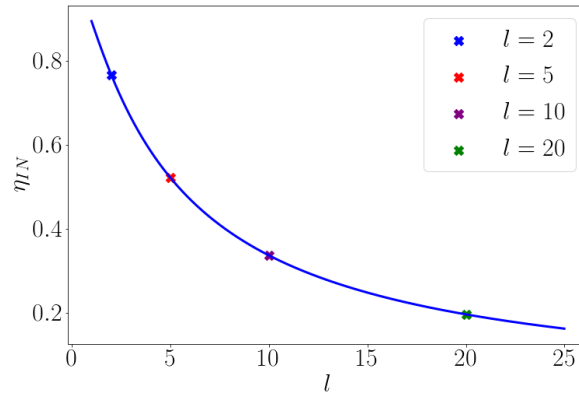
Figure 6.5: Critical area fraction of isotropic-nematic phase transition $\eta_{IN}(l)$ as a function of particle aspect ratio (Equation 6.14). For a given particle aspect ratio, nematic order parameters α^2 and S become nonzero at this area fraction or number density.

(a) f_{ex} (b) f_{id}
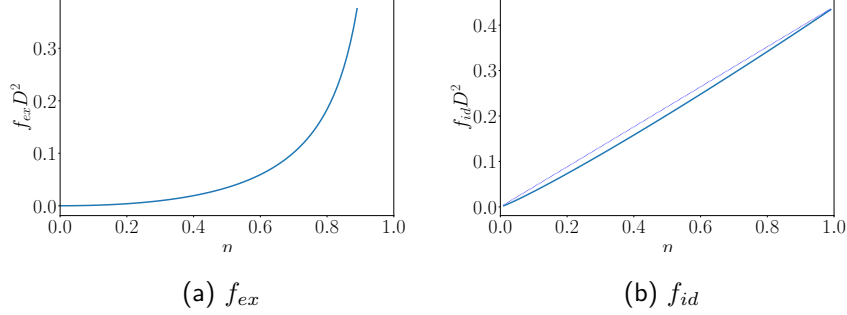
Figure 6.6: Local energy density terms as a function of area fraction η. A linear function is plotted for comparison. Note factor of D^2: where particle lengthscale D is small energy densities can be high.

the local energy density of a hard rod fluid depends on the relative size of the particles, with smaller particles having a greater number density and greater entropic energy contribution. For reasonably microscopic particles, number density, and therefore entropic energy density, can be high.

In this work I will neglect the possibility of smectic and crystalline phases and use the analytic formulae describing isotropic and nematic phases extensively to build the final model and simulation. The translationally ordered smectic and crystalline phases have been found computationally to occur at high area fractions $\eta \gtrsim .75$ for a wide range of relevant aspect ratios, for more details see results in [4].

The density functional theory is used to uncover microscopic density distributions, where density modulations on the scale of individual particles indicate translationally ordered phases. Taking the results as equations of state, I apply the formulae on a larger scale. Long-range variations in density, which may be induced by an external potential such as curvature or simply by thermal fluctuations in director, are treated by elasticity theory below. I assume Wittmann's formulae relating density, order, energy, and elasticity describe the material locally and use the analytic formulae 6.2, 6.13, and 6.16 extensively to build a simulation of a nematic or isotropic hard rod material on our curved surface. The model used here, where the energy functions apply locally and there are gradient terms in a continuum field theory, assumes that the individual particles

are microscopic relative to the scale considered.

6.2 Elasticity of a hard rod fluid

In the continuum model outlined above, the other energy contribution is a nonlocal contribution from gradient terms. Following Wittmann *et al.* [5], where the authors derive Frank constants K_ϵ (coefficients of gradients in director) for a three-dimensional material of hard spherocylinders, I here analogously derive Frank constants of a two-dimensional material of hard discorectangles. I also derive additional coefficents J_ϵ, relating to gradients in area fraction.

For three-dimensional liquid crystalline materials with a vector order parameter, elasticity is commonly described by the Frank free energy density, in three dimensions

$$F_{grad}^{3D} = \frac{1}{2}\left[K_1(\nabla \cdot \hat{n})^2 + K_2(\hat{n} \cdot \nabla \times \hat{n})^2 + K_3(\hat{n} \times \nabla \times \hat{n})^2 \right.$$
$$\left. + \; K_{24}\nabla \cdot ((\nabla \cdot \hat{n})\hat{n} - \hat{n}(\nabla \cdot \hat{n})) \right], \tag{6.17}$$

with K_1, K_2, K_3, K_{24} constants giving resistance to splay, bend, and twist respectively. The last (K_{24}) term is a saddle-splay or surface term often omitted as negligible or not relevant. In two dimensions there is no twist term K_2. In two dimensions with no boundary term we have

$$F_{grad}^{2D} = \frac{1}{2}\left[K_1(\nabla \cdot \hat{n})^2 + K_3(\hat{n} \times \nabla \times \hat{n})^2 \right], \tag{6.18}$$

or, in the one-Frank-constant approximtion, simply

$$F_{grad} = \frac{1}{2}K(\partial_i \hat{n}_j)^2. \tag{6.19}$$

In the one-Frank-constant approximation, it is relatively simple to replace the two-headed vector director $\hat{n}$ with an equivalent unit complex 2-atic order parameter and the derivative operator with the covariant derivative operator D_i, coupling orientational order to curvature in the usual way.

6.2.1 Taylor expansion and Poniewierski-Stecki formula

Gradient terms are derived via the principle of Taylor expansion, as carried out by Poniewierski and Stecki [9] in a general formulation, which finds that Frank

constants may be obtained as integrals over the material's two-point correlation function. From their DFT theory, which entails a specific expression for the correlation function, Wittmann *et al.* are then able to carry out the integrals.

Following Poniewierski and Stecki, we start with an arbitrary local energy function, move to Fourier space, express energy density as a series expansion in functional derivatives around the local value, and integrate by parts to obtain the gradient energy contribution

$$
\int_V d\mathbf{r} f_{grad} = \int_V \int_0^{2\pi} d\mathbf{r} d\phi \, a_i \frac{\partial \rho(\mathbf{r}, \phi)}{\partial r_i}
$$
$$
+ \frac{1}{2} \int_V \int_0^{2\pi} \int_0^{2\pi} d\mathbf{r} d\phi d\phi' (m_{ij} + h_{ij}) \frac{\partial \rho(\mathbf{r}, \phi)}{\partial r_i} \frac{\partial \rho(\mathbf{r}, \phi')}{\partial r_j} \quad (6.20)
$$
$$
+ \frac{1}{2} \int_{\partial S} \int_0^{2\pi} dl_j d\phi \, b_{ij} \frac{\partial \rho(\mathbf{r}, \phi)}{\partial r_i}
$$

in an area or volume V with boundary ∂S.

The coefficient of square derivative terms is divided into the symmetric tensor m_{ij} and the antisymmetric tensor h_{ij}. Terms a_i and h_{ij} will vanish for symmetry reason - a_i relates to first derivatives while h_{ij} is an antisymmetric tensor - and the b_{ij} term is a surface term, leaving an elasticity energy density

$$
f_{grad} = \frac{1}{2} \int_0^{2\pi} \int_0^{2\pi} d\phi d\phi' m_{ij} \frac{\partial \rho(\mathbf{r}, \phi)}{\partial r_i} \frac{\partial \rho(\mathbf{r}, \phi')}{\partial r_j} \quad (6.21)
$$

Ponierwiesrki and Stecki find that the remaining coefficients m_{ij} are related to the direct two-body correlations functions $c^{(2)}(\mathbf{r}, \phi, \phi')$ as

$$
m_{ij}(\phi, \phi') = \frac{1}{2} \int_0^\infty d\mathbf{r} \, r_i r_j c^{(2)}(\mathbf{r}, \phi, \phi'), \quad (6.22)
$$

with the spatial integral now centered on a particle and extending over all of space. To derive the Frank constants of the nematic phase, Poniewierski and Stecki as well as Wittmann *et al.* proceed by setting $\rho(\mathbf{r}, \phi) = \rho_0 g(\phi)$, a fixed number density ρ_0 and a pre-determined orientational distribution $g(\alpha^2, \cos\phi)$ around director $\hat{n}$. Only the mean direction of orientational order, $\hat{n}$, on which the distribution g is centered, is allowed to vary spatially. Then the derivative term reads

$$
\frac{\partial \rho(\mathbf{r}, \phi)}{\partial r_i} = \rho_0 \frac{\partial \hat{n}}{\partial r_i} \frac{\partial g}{\partial \hat{n}}. \quad (6.23)
$$

Factor of $\rho_0 \frac{\partial g}{\partial n_i} = \frac{\eta}{A} \frac{\partial g}{\partial \cos \phi} \hat{\phi}_j$ resulting from the above chain rule are incorporated into the integral m_{ij} and integrated over all possible particle orientations ϕ to form the coeffients

$$M_{iijj}^{nn} = \frac{\eta^2}{2A^2} \int d\phi d\phi' d\mathbf{r} r_i r_i c^{(2)}(\mathbf{r}, \phi, \phi') \frac{\partial g(\phi)}{\partial \cos \phi} \frac{\partial g(\phi')}{\partial \cos \phi'} \phi_j \phi'_j \tag{6.24}$$

of spatial variations in the unit director, $\frac{\partial n_i}{\partial r_j} \frac{\partial n_i}{\partial r_j}$. Comparing with equation 6.19, the coefficients of squared derivatives of the unit director can be directly identified with the Frank constants, $K_\epsilon = M_{\epsilon\epsilon 11}^{nn}$

Letting both local number density ρ_0 and local director $\hat{n}$ vary spatially, the density distribution takes the form

$$\rho(\mathbf{r}, \phi) = \frac{\eta}{A}(\mathbf{r}) g(\alpha^2(\eta(\mathbf{r})), \cos \phi) \tag{6.25}$$

With this more general form, the spatial derivative term $\frac{\partial \rho}{\partial r_i}$ can be decomposed to

$$\begin{aligned}
\frac{\partial \rho}{\partial r_i} &= \frac{\partial \rho_0}{\partial r} \cdot g(r_0) + \rho_0(r_0) \cdot \left(\frac{\partial \hat{n}}{\partial r_i} \frac{\partial g}{\partial \hat{n}} + \frac{\partial g}{\partial \alpha^2} \frac{\partial \alpha^2}{\partial r_i} \right) \\
&= \left(g + \rho_0 \frac{\partial \alpha^2}{\partial \rho_0} \frac{\partial g}{\partial \alpha^2} \right) \frac{\partial \rho_0}{\partial r} + \rho_0 \frac{\partial g}{\partial n} \frac{\partial n}{\partial r}.
\end{aligned} \tag{6.26}$$

We recognize the previous gradient term in $\hat{n}_i$ as well as the additional factor

$$g + \rho_0 \frac{\partial \alpha^2}{\partial \rho_0} \frac{\partial g}{\partial \alpha^2} \tag{6.27}$$

of gradients in η. The factor is absorbed into a cofficient $M_{ii}^{\eta\eta}$

$$\begin{aligned}
M_{ii}^{\eta\eta} = \frac{1}{2A^2} \int d\phi d\phi' d\mathbf{r} r_i r_i c^{(2)}(\mathbf{r}, \phi, \phi') &\left(g(\phi) + \eta \frac{\partial \alpha^2}{\partial \eta} \frac{\partial g(\phi)}{\partial \alpha^2} \right) \\
&\left(g(\phi') + \eta \frac{\partial \alpha^2}{\partial \eta} \frac{\partial g(\phi')}{\partial \alpha^2} \right).
\end{aligned} \tag{6.28}$$

In analogy to Frank elasticity constants, I additionally label gradient elasticity coefficients

$$\begin{aligned}
J_1 &:= M_{11}^{\eta\eta} \\
J_3 &:= M_{33}^{\eta\eta}.
\end{aligned} \tag{6.29}$$

6.2.2   Elasticity coefficients

Following Wittmann *et al.* I integrate the Poniewierski-Stecki formula

$$\beta K_\epsilon = \frac{\eta^2}{2a^2} \int d\mathbf{r} d\phi d\phi' r_\epsilon^2 c^{(2)}(\vec{r}, \phi, \phi') \frac{\partial \rho(\alpha^2, \cos\phi)}{\partial \cos\phi} \frac{\partial \rho(\alpha^2, \cos\phi)}{\partial \cos\phi} \hat{\phi}_x \hat{\phi}_x' \quad (6.30)$$

as well as, additionally, the formula for βJ_ϵ

$$\beta J_\epsilon = \frac{1}{2a^2} \int d\mathbf{r} d\phi d\phi' r_\epsilon^2 c^{(2)}(\vec{r}, \phi, \phi') \left(g(\phi) + \eta \frac{\partial \alpha^2}{\partial \eta} \frac{\partial g(\phi)}{\partial \alpha^2} \right)$$
$$\left(g(\phi) + \eta \frac{\partial \alpha^2}{\partial \eta} \frac{\partial g(\phi)}{\partial \alpha^2} \right). \quad (6.31)$$

An analytic evaluation of the integrals in Equations 6.30 and 6.35 is possible because FMMT supplies an analytic expression for f_{ex} and thus for the two-point correlation function $c^{(2)}(\mathbf{r}, \phi, \phi')$. The derivation presented here follows Wittmann and colleagues' work in deriving the Frank elasticity coefficients K_ϵ for a three-dimensional fluid of hard spherocylinders [5, 10], reworked for the two-dimensional case.

In Equation 6.31, after evaluating the derivative,

$$g(\phi) + \eta \frac{\partial \alpha^2}{\partial \eta} \frac{\partial g(\phi)}{\partial \alpha^2} = \left(1 - \eta \frac{\partial \alpha^2}{\partial \eta} S \right) g + \eta \frac{\partial \alpha^2}{\partial \eta} \left(2\cos^2\phi - 1 \right) g, \quad (6.32)$$

the integral over two factors in Equation 6.31 will later be deconvolved so that they can be evaluated as a combination of separate one-body integrals. There will be two terms in each of the one-body integrals: angular integrals over $g(\phi)$ and those over $(2\cos^2\phi - 1)g(\phi)$. The latter set of integrals is significantly more complicated. I therefore make an substitution

$$(2\cos^2\phi - 1)g \rightarrow Sg \quad (6.33)$$

so that

$$\left(1 - \rho_0 \frac{\partial \alpha^2}{\partial \rho_0} S \right) g + \rho_0 \frac{\partial \alpha^2}{\partial \rho_0} (2\cos^2\phi - 1)g \rightarrow g. \quad (6.34)$$

The substitution in the integrand is motivated because lower order one-body integrals $\int d\phi (2\cos^2\phi - 1)g(\phi)$ yield $2\pi S$, identical to integrals $\int d\phi Sg(\phi)$. However, it is not accurate for higher-order integrals $\int d\phi (2\cos^2\phi - 1)\sin^n\phi \cos^m\phi g(\phi)$; here the inclusion of a factor of $(2\cos^2\phi - 1)$ is not equivalent to an additional factor of S in the result. For example, integrals which yield a factor of $1 + S$

are replaced by a factor of $S + (1 - \bar{P}_4)/2$ when $\cos(2\phi)g$ is included in the integrand; instead I replace $1 + S \to (1 + S)S$. The error introduced by the substitution is not negligible, as it is multiplied by the factor $\eta \frac{\partial \alpha^2}{\partial \eta}$, which can take values around 200 around the isotropic-nematic transition and not less than 15 in the isotropic phase. The error introduced by the substitution exists only in the ordered phase and especially around the phase transition. The approximated part is the indirect effect of gradients in angle distribution sharpness that follow from gradients in area fraction. Thus our final result J_ϵ will be an approximation outside of the isotropic regime, which nevertheless represents the main features of the coefficient.

The formula for $\beta J\epsilon$ is then replaced with the simpler approximate formula

$$\beta J_\epsilon \approx \frac{1}{2A^2} \int d\mathbf{r} d\phi d\phi' r_\epsilon^2 c^{(2)}(\vec{r}, \phi, \phi') g(\phi) g(\phi) \tag{6.35}$$

To evaluate Equations 6.30 and 6.35, from an expression for free energy density, the direct two-body correlation function can be retrieved as

$$c^{(2)} = -\frac{\delta^2 \beta F}{\delta \rho \delta \rho}. \tag{6.36}$$

By chain rule the functional derivative consists of trivial derivatives of free energy density with respect to n_i, N and derivatives of n_i, N with respect to ρ. In the latter case the functional derivative by ρ simply drops factors of ρ in the integrands and the derivatives are the (convolutions of) weight functions ω. From the formula 6.2, the direct correlation function is

$$\begin{aligned}
-c^{(2)} = &\frac{\partial^2 f_{ex}}{\partial n_1 \partial n_2} (\omega^{(0)} \otimes \omega^{(2)} + \omega^{(2)} \otimes \omega^{(0)}) \\
&+ \frac{\partial^2 f_{ex}}{\partial n_2 \partial N} \left(\omega^{(2)} \otimes \frac{\delta N}{\delta \rho} + \frac{\delta N}{\delta \rho} \otimes \omega^{(2)} \right) \\
&+ 2\frac{\partial f_{ex}}{\partial N} (\Omega^{1 \otimes 1}).
\end{aligned} \tag{6.37}$$

with weight functions defined in equations 6.4 and the convolution [(1)]

$$
\begin{aligned}
\frac{\partial^2 N}{\partial \rho^2} = \Omega^{1 \otimes 1} &= \int \int dR_1 dR_2 \Omega^{(11)}(r - R_1, r - R_2) \\
&= \frac{5}{6\pi} \omega^{(1)} \otimes \omega^{(1)} \\
&\quad - \frac{1}{6\pi} (\underline{\omega}_1^{(1)} \otimes \underline{\omega}_1^{(1)} + \underline{\omega}_3^{(1)} \otimes \underline{\omega}_3^{(1)}) \\
&\quad - \frac{4}{6\pi} (\underline{\underline{\omega}}_{11}^{(1)} \otimes \underline{\underline{\omega}}_{11}^{(1)} + 2\underline{\underline{\omega}}_{13}^{(1)} \otimes \underline{\underline{\omega}}_{31}^{(1)} + \underline{\underline{\omega}}_{33}^{(1)} \otimes \underline{\underline{\omega}}_{33}^{(1)}) \\
&\quad + \dots
\end{aligned}
\tag{6.38}
$$

written as a series expansion analogous to equation 6.7.

After inserting Equation 6.37 into 6.30 and 6.35, we will have several terms of the form

$$
\mathcal{T}^n[\omega^\mu \otimes \omega^\nu] := \int \int \int d\phi d\phi' d\mathbf{r} r_\epsilon^2 (\omega^\mu \otimes \omega^\nu) \frac{\partial g}{\partial \cos \phi} \frac{\partial g}{\partial \cos \phi} \hat{\phi}_x \hat{\phi}_x
\tag{6.39}
$$

$$
\mathcal{T}^\eta[\omega^\mu \otimes \omega^\nu] := \int \int \int d\phi d\phi' d\mathbf{r} r_\epsilon^2 (\omega^\mu \otimes \omega^\nu) g g.
\tag{6.40}
$$

The two-body integrals can be deconvolved to products

$$
\mathcal{T}_\epsilon^x[\omega^{(\nu)} \otimes \omega^{(\mu)}] = \bar{\omega}_{\epsilon 0}^{x(\nu)} \bar{\omega}_{\epsilon 2}^{x(\mu)} - 2\bar{\omega}_{\epsilon 1}^{x(\nu)} \bar{\omega}_{\epsilon 1}^{x(\mu)} + \bar{\omega}_{\epsilon 2}^{x(\nu)} \bar{\omega}_{\epsilon 0}^{x(\mu)}
\tag{6.41}
$$

of the single-body integrals

$$
\bar{\omega}_{\epsilon,q}^{(\nu)n} := \frac{\eta}{A} \int d\mathbf{r} d\phi r_\epsilon^q \omega^{(\nu)}(\mathbf{r}, \phi) \frac{\partial g}{\partial \cos \phi} \hat{\phi}_x
\tag{6.42}
$$

$$
\bar{\omega}_{\epsilon,q}^{(\nu)\eta} := \frac{1}{A} \int d\mathbf{r} d\phi r_\epsilon^q \omega^{(\nu)}(\mathbf{r}, \phi) g(\alpha, \cos \phi).
\tag{6.43}
$$

All necessary integrals $\bar{\omega}_{\epsilon,q}^{(\nu)\eta}$ are evaluated in Section 6.2.3, below.

For the Frank constants K_ϵ, nonvanishing terms in Equation 6.30 are

$$
\beta K_\epsilon = \frac{\eta^2}{A^2} \frac{\partial f_{ex}}{\partial N} \left(-\frac{1}{3\pi} (\mathcal{T}[(\bar{\omega})_1 \otimes (\bar{\omega})_1] + \mathcal{T}[(\bar{\omega})_3 \otimes (\bar{\omega})_3]) - \frac{8}{3\pi} \mathcal{T}[(\bar{\omega})_{13} \otimes (\bar{\omega})_{13}] \right).
\tag{6.44}
$$

After inserting values of $\bar{\omega}^n$, the Frank constants are

---

[(1)]Convolution and the $\otimes$ symbol are defined by: $f \otimes g = \int d\mathbf{r} f(\mathbf{r} - \mathbf{r}_1) g(\mathbf{r} - \mathbf{r}_2)$

$$\beta K_1 = \frac{2\pi^2 \eta^2 D^4}{9(1-\eta)A^2} \left(l \left(8l^4 - 40l^2 - 3l\pi \right) \bar{P}_4 S + l^2 \left(20 + 8l^2 \right) S^2 \right) \tag{6.45}$$

and

$$\beta K_3 = \frac{2\pi^2 \eta^2 D^4}{9(1-\eta)A^2} \left(-l \left(8l^4 - 40l^2 - 3l\pi \right) \bar{P}_4 S + l^2 \left(20 + 8l^2 \right) S^2 \right). \tag{6.46}$$

with $\bar{P}_4$ the next-higher moment of the angle distribution, see Box 6.2.3. In two dimensions, the coefficients K_ϵ are unitless: their value does not depend on relative lengthscale of the particles. The coefficients (Figure 6.7) become nonzero at the isotropic-nematic transition, where S becomes nonzero. They then increase quadratically in area fraction, as density, and thereby order, increases. The coefficients are undefined for aspect ratios less than $\sqrt{2}$. Comparing K_1 and K_3, only the sign of the term linear in S differs. The K_3 (bend) coefficient is larger than K_1 (splay). In the one-Frank-constant approximation, I take the mean

$$\beta K = \frac{2\eta^2 \pi^2 l^2 D^4 S^2}{9(1-\eta)A^2} (20 + 8l^2) \tag{6.47}$$

as the value of both Frank constants.

Inserting 6.40 and 6.37 into the approximation 6.35 and retaining nonvanishing terms, I derive the density coefficients J_ϵ:

$$\beta J_\epsilon = \frac{\partial^2 f_{ex}}{\partial n_0 \partial n_2} \left(\mathcal{T}[\omega^{(0)} \otimes \omega^{(2)}] \right)$$
$$\frac{\partial^2 f_{ex}}{\partial n_2 \partial N} \left(\frac{\partial N}{\partial n_1} \mathcal{T}[\omega^{(1)} \otimes \omega^{(2)}] + \frac{\partial N}{\partial \underline{n}_1} \cdot \mathcal{T}[\underline{\omega}^{(1)} \otimes \omega^{(2)}] + \frac{\partial N}{\partial \underline{\underline{n}}_1} \cdot \mathcal{T}[\underline{\underline{\omega}}^{(1)} \otimes \omega^{(2)}] \right)$$
$$\frac{\partial f_{ex}}{\partial N} \left(\frac{\partial^2 N}{\partial n_1 n_1} \mathcal{T}[\omega^{(1)} \otimes \omega^{(1)}] + \frac{\partial^2 N}{\partial \underline{n}_1 \underline{n}_1} \mathcal{T}[\underline{\omega}^{(1)} \otimes \underline{\omega}^{(1)}] + \frac{\partial^2 N}{\partial \underline{\underline{n}}_1 \underline{\underline{n}}_1} \mathcal{T}[\underline{\underline{\omega}}^{(1)} \otimes \underline{\underline{\omega}}^{(1)}] \right). \tag{6.48}$$

Coefficients are of the form

$$\beta J_1 = J^{(0)} - J^{(1)} S - J^{(2)'} S^2 + J^{(2)} S^2$$
$$\beta J_3 = J^{(0)} + J^{(1)} S + J^{(2)'} S^2 + J^{(2)} S^2 \tag{6.49}$$
$$\beta J = J^{(0)} + J^{(2)} S^2.$$
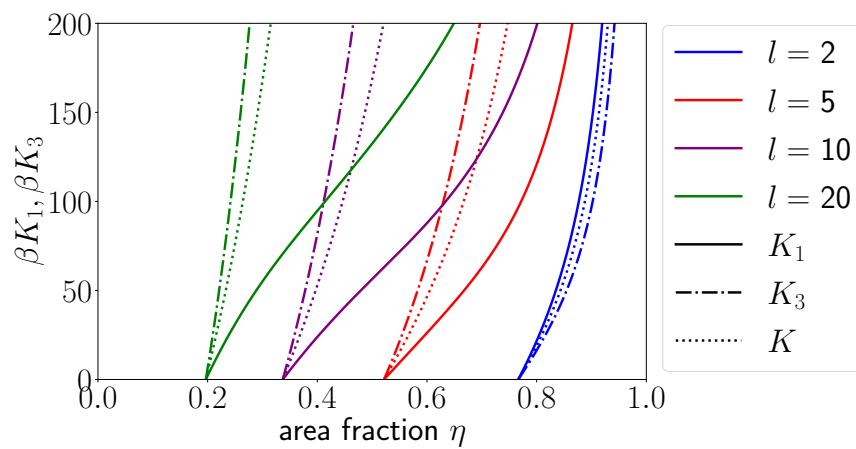
Figure 6.7: Frank constants K_1, K_3, and K as functions of area fraction η, as found in Equations 6.45, 6.46, and 6.47, for four example particle aspect ratios. All Frank constants become nonzero at the critical area fraction $\eta_{IN}(l)$ for each aspect ratio, and increase rapidly for higher particle densities. In two dimensions, Frank constants are scale-independent; βK_ϵ is unitless. 'Bend' coefficient K_3 is larger than 'splay' coefficient K_1. The mean K, substituted for both in the one-Frank-constant approximation, is shown as the central dotted line. I here use aspect ratio $l = 5$ (red).
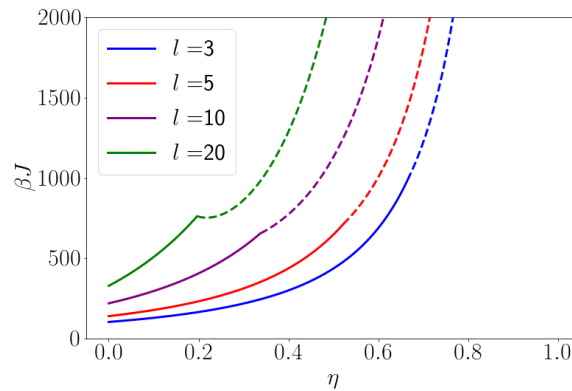
Figure 6.8: Additional elasticity coefficients J_ϵ, which indicate resistance to spatial variation in particle area fraction. Only the mean J is shown, as I continue with the one-Frank-constant approximation and an analogous isotropic approximation for J. Unlike the Frank constants $K_{epsilon}$, this quantity is nonzero in the isotropic phase (solid lines). There is a discontinuity as the material transitions from the isotropic to the nematic phase (dashed line). However, the decrease around the isotropic-nematic transitions at high aspect ratios retrieved here is a consequence of the non-negligible omission described in Equation 6.34. For the aspect ratio $l = 5$ used here, the problem is less severe. Like βK, βJ is unitless and does not depend on the relative scale of the particles.

In line with the one-Frank-constant approximation, in the isotropic-coefficient approximation $J_1 = J_3 = J$, we require

$$
\begin{aligned}
J^{(0)} &= \frac{\pi D^4}{(1-\eta)A^2}\left(\frac{17l\pi}{2} + \frac{19l^3\pi}{9} + \frac{4\pi^2}{3} + \frac{14l^2}{3} + l^2\pi^2 - \frac{l^4}{9}\right) \\
&+ \frac{\pi\eta(2l+\pi)D^4}{36(1-\eta)^2(4l+\pi)A^2}\left(40l^4 + 330l\pi + 166l^3\pi + 45\pi^2 + 3l^2(232 + 15\pi^2)\right) \\
&- \frac{\pi D^4}{36(1-\eta)A^2}\left(12l^4 + 72l\pi + 24l^3\pi + 9\pi^2 + 9l^2(12+\pi^2)\right)\bar{P}_4
\end{aligned}
\tag{6.50}
$$

and

$$
J^{(2)} = \frac{8l^2\pi D^4}{3(1+\eta)A^2}S^2.
\tag{6.51}
$$

For example, at aspect ratio $l = 5$, the isotropic elasticity coefficient J is

$$
\beta J(l=5) = \frac{140.288 - 60.137\bar{P}_4}{1-\eta} + \frac{184.066\eta}{(1-\eta)^2} + \frac{6.257}{1-\eta}S^2.
\tag{6.52}
$$

Like K, J is unitless. Unlike K, J is nonzero in the isotropic phase. The value depicted in Figure 6.8 is accurate in the isotropic phase. In the nematic phase, the value is approximate. In particular, a positive contribution at the onset of the nematic phase is missing due to approximation 6.35, falsely leading to the initially decreased value in the nematic phase. However, at the aspect ratio used here, $l = 5$, the inaccuracy is small. Another inconsistency is that the value does not go to zero in the dilute limit. Possibly, this is because the theory, incorporating some free parameters which are chosen heuristically, was not optimized to accurately reproduce density gradients in the choice of parameter b.

The Taylor expansion approach presented here results in two independent terms pertaining to gradients in direction $\mathbf{n}$ and in area fraction η respectively. It is strictly accurate within the Taylor expansion formalism of Equation 6.26. To account for correlation functions between particles with varying order parameter at the particle level, another route is presented in [10], which generalizes the integration over particle pairs to spatially varying distribution functions, necessitating more complicated integrals over angled particle.
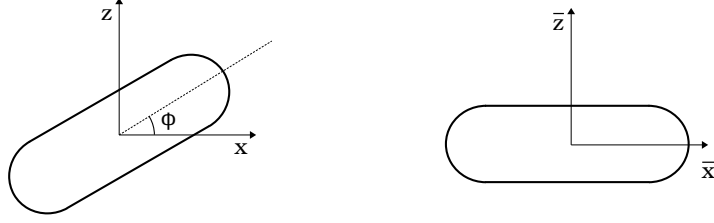
Figure 6.9: Space-centered frame (x, z) and body-centered frame $(\bar{x}, \bar{z})$

6.2.3 Evaluation of single-body integrals $\bar{\omega}$

Evaluation of the integrals $\bar{\omega}_{\epsilon r}^{x(\nu)}$, as defined in Equations 6.42 and 6.43 and used in Equations 6.44 and 6.48 via Equation 6.41, is presented in this section. Indices $x = n, \eta$ label two different forms of integral used in K and J respectively; ν labels which weight functions, including vector and tensor forms, appears in the integrand; $\epsilon = x, z$ distinguishes the two spatial directions and $q = 0, 1, 2$ is the exponent of r_ϵ.

In the weight function (Equation 6.4) term of the integrands, the Heaviside Θ function in $\omega^{(2)}$ is interpreted to restricting the domain of integration to the area of a particle, while the Dirac delta in $\omega^{(1)}$ and $\omega^{(0)}$ indicates integration along the particle boundary. The factor $\frac{1}{\mathbf{n}(\hat{\mathbf{r}}, \phi) \cdot \hat{\mathbf{r}}}$ simply gives the correct measure for the line integral along the particle boundary. It is easier to evaluate the spatial integrals over the weight functions in Equations 6.42 and 6.43 in the particle-centered frame $(\bar{x}, \bar{z})$ (Figure 6.9).

The quantities r_ϵ, and $\hat{\phi}_x$ in the integrands of Equations 6.42 and 6.43 can also be expressed as functions of $(\bar{x}, \bar{z})$ coordinates and of ϕ. The space centered position vector r is expressed in the body-centered frame as

$$r(\phi, \bar{r}) = \begin{pmatrix} \cos\phi\bar{x} + \sin\phi\bar{z} \\ -\sin\phi\bar{x} + \cos\phi\bar{z} \end{pmatrix}. \tag{6.53}$$

On the other hand indices $\epsilon = 1, 3$ continue to refer to decomposition on the-space centered (x, z) basis. The unit director $\hat{\phi}$ off a particle is decomposed in the (x, z) basis so that $\hat{\phi}_x = \sin\phi$.

Similarly, vector and tensor indices on $\underline{\omega}^{(1)}$ and $\underline{\underline{\omega}}^{(1)}$ refer to a decomposition in terms of directions (x, z) of the space-centered frame. By applying the rotation matrix

$$\mathcal{R}(\phi) = \begin{pmatrix} \cos \phi & \sin \phi \\ -\sin \phi & \cos \phi \end{pmatrix} \tag{6.54}$$

to all normal vectors $\hat{n}(\bar{r})$ occurring in $\underline{\omega}^{(1)}$ and $\underline{\underline{\omega}}^{(1)}$, expressions for the components in the space-centered basis are

$$\hat{n}(\bar{x}, \bar{z}, \phi) = \begin{pmatrix} \cos \phi \, n_{\bar{x}} + \sin \phi \, n_{\bar{z}} \\ -\sin \phi \, n_{\bar{x}} + \cos \phi \, n_{\bar{z}} \end{pmatrix}. \tag{6.55}$$

Additionally the 2×2 outer product of two normal vectors $(n_{\bar{x}}, n_{\bar{z}})$, occurring in tensorquatitites $\underline{\underline{\omega}}^{(\nu)}$, is

$$\hat{n}\hat{n}^T =$$

$$\begin{pmatrix} \begin{array}{c} n_{\bar{x}}^2 \cos^2 \phi + n_{\bar{z}}^2 \sin^2 \phi \\ +2n_{\bar{x}}n_{\bar{z}} \cos \phi \sin \phi \end{array} & \begin{array}{c} (-n_{\bar{x}}^2 + n_{\bar{z}}^2) \cos \phi \sin \phi \\ +n_{\bar{x}}n_{\bar{z}}(\cos^2 \phi - \sin^2 \phi) \end{array} \\ \\ \begin{array}{c} (-n_{\bar{x}}^2 + n_{\bar{z}}^2) \cos \phi \sin \phi \\ +n_{\bar{x}}n_{\bar{z}}(\cos^2 \phi - \sin^2 \phi) \end{array} & \begin{array}{c} n_{\bar{x}}^2 \sin \phi + n_{\bar{z}}^2 \cos^2 \phi \\ -2n_{\bar{x}}n_{\bar{z}} \cos \phi \sin \phi \end{array} \end{pmatrix} \tag{6.56}$$

in the space-centered basis.

Vector and tensor weight functions $\underline{\omega}$, $\underline{\underline{\omega}}$ thus contain information on the orientation ϕ of a particle relative to the space-centered frame and will contribute dependence of elasticity coefficients K_ϵ and J_ϵ on order parameter S.

After substituting expressions in the space-centered frame, integrals 6.42 and 6.43 are sums of terms of the form

$$\frac{4\alpha^2}{I_0(\alpha^2)} \int d\phi \, g(\alpha^2, \cos \phi) \cos \phi \sin \phi \cos^n \phi \sin^m \phi \cdot \int d\bar{r} \, \bar{x}^a \bar{z}^b \hat{n}_x^c \hat{n}_z^d \tag{6.57}$$

and

$$\frac{1}{I_0(\alpha^2)} \int d\phi \, g(\alpha^2, \cos \phi) \cos^n \phi \sin^m \phi \cdot \int d\bar{r} \, \bar{x}^a \bar{z}^b \hat{n}_x^c \hat{n}_z^d \tag{6.58}$$

respectively.

The integrals $\bar{\omega}_{\epsilon q}^{(\nu)x}$ are evaluated in the tables 6.2, 6.3, 6.4, 6.5, and Equations 6.59. Not listed in Equations 6.59 are integrals $\mathcal{C}, \mathcal{F}, \mathcal{R}, \mathcal{S}, \mathcal{T}, \mathcal{U}$, which

vanish due to spatial antisymmetry of the integrands $\bar{x}\bar{z}$, $n_x n_z$, $n_x^2 \bar{x}\bar{z}$, $n_z \bar{x}\bar{z}$, $n_{\bar{x}} n_{\bar{z}} \bar{x}^2$, and $n_{\bar{x}} n_{\bar{z}} \bar{z}^2$ respectively.

Table 6.2: Integrals $\bar{\omega}_{1q}^{(\nu)n}$ for K_1. See Equation 6.59 for values of the spatial integrals denoted by calligraphic capital letters. Values which are irrelevant due to multiplication with a vanishing term are omitted with - .

| | $\epsilon = 1$ | | |
	$q = 0$	1	2
$\omega^{(\nu)}$	0	0	-
$(\underline{\omega}^{(1)})_1$	0	$2\pi(\mathcal{J} + \mathcal{L})S$	0
$(\underline{\omega}^{(1)})_3$	0	$2\pi(\mathcal{H} - \mathcal{G})S$	0
$(\underline{\underline{\omega}}^{(1)})_{11}$	$\mathcal{F}2\pi S$	0	-
$(\underline{\underline{\omega}}^{(1)})_{13}$	$(-\mathcal{D} + \mathcal{E})2\pi S$	0	$\pi((\mathcal{O} - \mathcal{P} - \mathcal{M} + \mathcal{N})S$ $+(\mathcal{O} - \mathcal{M} + \mathcal{P} - \mathcal{N} + 2\mathcal{Q})\bar{P}_4))$
$(\underline{\underline{\omega}}^{(1)})_{33}$	$-\mathcal{F}2\pi S$	0	-

Table 6.3: Integrals $\bar{\omega}_{3q}^{(\nu)n}$ for K_3.

| | $\epsilon = 3$ | | |
	$q = 0$	1	2
$\omega^{(\nu)}$	0	0	-
$(\underline{\omega}^{(1)})_1$	0	$2\pi S(\mathcal{J} + \mathcal{L})$	0
$(\underline{\omega}^{(1)})_3$	0	$2\pi S(\mathcal{G} - \mathcal{H})$	0
$(\underline{\underline{\omega}}^{(1)})_{11}$	$\mathcal{F}2\pi S$	0	-
$(\underline{\underline{\omega}}^{(1)})_{13}$	$(-\mathcal{D} + \mathcal{E})2\pi S$	0	$\pi((\mathcal{O} - \mathcal{P} - \mathcal{M} + \mathcal{N})S$ $-(\mathcal{O} - \mathcal{M} + \mathcal{P} - \mathcal{N} + 2\mathcal{Q})\bar{P}_4))$
$(\underline{\underline{\omega}}^{(1)})_{33}$	$-\mathcal{F}2\pi S$	0	-

Table 6.4: Integrals $\bar{\omega}_{1q}^{(\nu)\eta}$ for J_1.

	$\epsilon = 1$		
	$q = 0$	1	2
$\omega^{(\nu)}$	$2\pi\mathcal{X}_\nu$	0	$\pi(\mathcal{A}_\nu(1+S) + \mathcal{B}_\nu(1-S))$
$(\underline{\omega}^{(1)})_1$	0	$\pi((1+S)\mathcal{G} + (1-S)\mathcal{H})$	0
$(\underline{\omega}^{(1)})_3$	0	$\pi((1+S)\mathcal{J} + (-1+S)\mathcal{L})$	0
$(\underline{\underline{\omega}}^{(1)})_{11}$	$\pi(\mathcal{D}(1+S)$ $+\mathcal{E}(1-S))$	0	$\pi((\mathcal{M}+\mathcal{N})\bar{P}_4 + (\mathcal{M}-\mathcal{N})S$ $+(1-\bar{P}_4)/4(2\mathcal{Q}+\mathcal{O}+\mathcal{P}))$
$(\underline{\underline{\omega}}^{(1)})_{13}$	$\pi S\mathcal{F}$	0	$-$
$(\underline{\underline{\omega}}^{(1)})_{33}$	$\pi(\mathcal{D}(1-S)$ $+\mathcal{E}(1+S))$	0	$\pi((\mathcal{O}+\mathcal{P})\bar{P}_4 + (\mathcal{O}-\mathcal{P})S$ $+(1-\bar{P}_4)/4(-2\mathcal{Q}+\mathcal{M}+\mathcal{N}))$

Table 6.5: Integrals $\bar{\omega}_{3q}^{(\nu)\eta}$ for J_3.

	$\epsilon = 3$		
	$q = 0$	1	2
$\omega^{(\nu)}$	$2\pi\mathcal{X}_\nu$	0	$\pi(\mathcal{A}_\nu(1-S) + \mathcal{B}_\nu(1+S))$
$(\underline{\omega}^{(1)})_1$	0	$\pi((1+S)\mathcal{L} + (-1+S)\mathcal{J})$	0
$(\underline{\omega}^{(1)})_3$	0	$\pi((1+S)\mathcal{H} + (1-S)\mathcal{G})$	0
$(\underline{\underline{\omega}}^{(1)})_{11}$	$\pi(\mathcal{D}(1+S)$ $+\mathcal{E}(1-S))$	0	$\pi((\mathcal{O}+\mathcal{P})\bar{P}_4 + (-\mathcal{O}+\mathcal{P})S$ $+(1-\bar{P}_4)/4(-2Q+O+P))$
$(\underline{\underline{\omega}}^{(1)})_{13}$	$\pi S\mathcal{F}$	0	$-$
$(\underline{\underline{\omega}}^{(1)})_{33}$	$\pi(\mathcal{D}(1-S)$ $+\mathcal{E}(1+S))$	0	$\pi((\mathcal{M}+\mathcal{N})\bar{P}_4 + (-\mathcal{M}+\mathcal{N})S$ $+(1-\bar{P}_4)/4(2\mathcal{Q}+\mathcal{O}+\mathcal{P}))$

$$\mathcal{X}_\nu := \int d\bar{r}\,\omega^{(\nu)} = n_\nu/\rho_0$$

$$\mathcal{A}_\nu := \int d\bar{r}\,\bar{x}^2\omega^{(\nu)}$$

$$\mathcal{A}_0 := \int_{\partial A} d\bar{r}\,\bar{x}^2 K/(2\pi) = DL/\pi + D^2/8 + L^2/4$$

$$\mathcal{A}_1 := \int_{\partial A} d\bar{r}\,\bar{x}^2 = D^2L + D^3\pi/8 + DL^2\pi/4$$

$$\mathcal{A}_2 := \int_A d\bar{r}\,\bar{x}^2 = DL^3/12 + \frac{D^2\pi}{32}(D^2 + 2L^2)$$

$$\mathcal{B}_\nu := \int d\bar{r}\,\bar{z}^2\omega^{(\nu)}$$

$$\mathcal{B}_0 := \int_{\partial A} d\bar{r}\,\bar{z}^2 K/(2\pi) = D^2/8$$

$$\mathcal{B}_1 := \int_{\partial A} d\bar{r}\,\bar{z}^2 = D^3\pi/8 + LD^2/2$$

$$\mathcal{B}_2 := \int_A d\bar{r}\,\bar{z}^2 = D^3L/12 + D^4\pi/32$$

$$\mathcal{D} := \int_{\partial A} d\bar{r}\,n_{\bar{x}}^2 = \frac{D\pi}{2}$$

$$\mathcal{E} := \int_{\partial A} d\bar{r}\,n_{\bar{z}}^2 = 2L + D\pi/2 \tag{6.59}$$

$$\mathcal{G} := \int_{\partial A} d\bar{r}\,\bar{x}n_{\bar{x}} = \frac{D^2\pi}{4}$$

$$\mathcal{H} := \int_{\partial A} d\bar{r}\,\bar{z}n_{\bar{z}} = DL + \frac{D^2\pi}{4}$$

$$\mathcal{I} := \int_{\partial A} d\bar{r}\,\bar{x}n_{\bar{z}} = DL$$

$$\mathcal{L} := \int_{\partial A} d\bar{r}\,\bar{z}n_{\bar{x}} = 0$$

$$\mathcal{M} := \int_{\partial A} d\bar{r}\,\bar{x}^2 n_{\bar{x}}^2 = \frac{D}{96}\left(64DL + 9D^2\pi + 12L^2\pi\right)$$

$$\mathcal{N} := \int_{\partial A} d\bar{r}\,\bar{z}^2 n_{\bar{z}}^2 = \frac{D^2L}{2} + \frac{3\pi D^3}{32}$$

$$\mathcal{O} := \int_{\partial A} d\bar{r}\,\bar{x}^2 n_{\bar{z}}^2 = \frac{D}{96}\left(32DL + 3D^2\pi + 12L^2\pi\right) + \frac{L^3}{6}$$

$$\mathcal{P} := \int_{\partial A} d\bar{r}\,\bar{z}^2 n_{\bar{x}}^2 = \frac{\pi D^3}{32}$$

$$\mathcal{Q} := 2\int_{\partial A} d\bar{r}\,\bar{x}\bar{z}n_{\bar{x}}n_{\bar{z}} = \frac{\pi D^3}{16}.$$

Higher moments of angle distributions

The angular integrals are useful in deriving Table 6.2 and Table 6.3:

$$\frac{4\alpha^2}{I_0(\alpha^2)} \int_0^{2\pi} d\phi \cos^2\phi \sin^2\phi g(\cos\phi, \alpha^2) = 2\pi S, \qquad (6.60)$$

$$\frac{4\alpha^2}{I_0(\alpha^2)} \int_0^{2\pi} d\phi \cos^4\phi \sin^2\phi g(\cos\phi, \alpha^2) = \pi(S + \bar{P}_4), \qquad (6.61)$$

and

$$\frac{4\alpha^2}{I_0(\alpha^2)} \int_0^{2\pi} d\phi \cos^2\phi \sin^4\phi g(\cos\phi, \alpha^2) = \pi(S - \bar{P}_4). \qquad (6.62)$$

Just as the base order parameter S is given by integrating over the polynomial $\cos(2\phi) = (2\cos^2\phi - 1)$ with the orientation distribution $g(\cos\phi, \alpha^2)$,

$$S := \frac{1}{I_0(\alpha^2)} \int_0^{2\pi} d\phi (2\cos^2\phi - 1) g(\cos\phi, \alpha^2), \qquad (6.63)$$

further moments of the angle distributions are generated from the next polynomials series.

Analogous to S, we can define

$$\bar{P}_m = d\phi \int_0^{2\pi} \cos(m\phi) g(\cos\phi, \alpha^2), \qquad (6.64)$$

related to the Bessel functions $I_n(\alpha^2)$ as

$$S = \bar{P}_2 = \frac{I_1(\alpha^2)}{I_0(\alpha^2)}$$
$$\bar{P}_3 = 0 \qquad (6.65)$$
$$\bar{P}_4 = \frac{I_2(\alpha^2)}{I_0(\alpha^2)}.$$

A recurrence relation for modified Bessel functions of the first kind is

$$I_{n-1}(x) - I_{n+1}(x) = \frac{2n}{x} I_n(x); \qquad (6.66)$$

it follows that

$$\bar{P}_4 = 1 - \frac{2}{\alpha^2} S. \qquad (6.67)$$

6.3   Effect on channel shape

Returning to the question of the stability and shape of an cylindrical channel hosting an orientationally ordered material, with the description of the interfacial material used above, we now have an internal Hamiltonian of the form

$$\mathcal{H}_I = \int_S dS[f_{loc}(\eta) + f_{grad}(\eta, \hat{n})]$$

$$f_{loc}(\eta) = f_{id}(\eta) + f_{ex}(\eta) \tag{6.68}$$

$$f_{grad}(\eta, \hat{n}) = K(\eta)/2(\tilde{D}_i \hat{n}_j)^2 + J(\eta)/2(\partial_i \eta)^2$$

describing a two-dimensional hard-rod fluid; replacing the generic Landau-Ginzburg theory (Equation 3.2) of orientational order used in Chapters 2 to 4. Here $\tilde{D}$ is symbolic of a covariant derivative operator, which however cannot be implemented with the same formulation (Equation 3.4) used earlier, as $\hat{n}$ is a double-headed vector rather than a 2-atic complex order parameter.

The new theory, taking into account local number density or area fraction, allows me to add the additional constraint

$$R = \int_S \rho \, dS = const, \tag{6.69}$$

representing a fixed number of adsorbed nanoparticles, to the model. The constraint plays an equivalent role to a chemical potential, but fixes particle number more strictly and is straightforward to enforce in simulation with material-exchanging sampling steps. Unlike in a computational DFT minimization for determining phase based on a smaller volume in an homogeneous and open system, a canonical ensemble rather than a grand canonical ensemble is sampled here. In this more coarse-grained simulation, the whole system is simulated and a goal of the simulation is to represent the fact that a constant number of particles remain irreversibly adsorbed.

The gradient term differs in form from that in our previous model Landau-Ginzburg theory, Equation 3.2. Dependence of magnitude of gradient energy on amount of order is shifted from the oriented field Ψ or $\hat{n}$ to the Frank constants as

$$c|D_i \Psi|^2 \rightarrow K(\eta)/2(\tilde{D}_i \hat{n})^2 + J(\eta)/2(\partial_i \eta)^2 \tag{6.70}$$

The consequence that materials with more order have higher gradient energy contributions remains qualitatively the same.

While gradient energy is scale-invariant, local energy density is not. The function $f_{loc}(\eta)$ is convex, meaning that total system energy is minimized by a spatially homogeneous density distribution. At any reasonable particle scale, the homogenizing effect is overwhelming compared to the curvature-coupled gradient energy term, which was initially hypothesized to induce density modulations. The commonly used assumption of spatially homogeneous particle density as well as homogeneous order parameter is accurate.

As an example, assume the channel lengthscale $r_0 = 1$ is a micron while particle diameter, $D = 0.001$ in units of r_0, is a nanometer. Then gradient energy densities are of order $10k_BT/(\mu m)^2$, while differences in local entropic energy densities f_{loc} are of order $10^5 \ k_BT/(\mu m)^2$. Surface tension (of the bare interface between particles), at 10^7 or $10^8 \ k_BT/(\mu m)^2$ (Table 2.3), is bigger than all of these effects, holding the interface together despite the entropic pressure of the embedded particles. The relative size of particles and channel is limited to the values assumed above by the choice of model, the continuum description being accurate only for sufficiently small and numerous particles. On the other hand the relationship between channel and particle size and units, and thereby the relationship between 'internal' effects and surface tension, is informed by realistic experimental parameters.

Due to vastly differing orders of magnitude in the relevant energy densities, there is a distinct hierarchy of effects:

- Channel shape and stability is completely determined by surface area and bending rigidity effects, as explored in Chapter 2.

- An interfacial fluid of hard rods is homogeneous with respect to number density. The order parameter is also spatially homogeneous, either everywhere ordered for $\eta > \eta_{NI}$ or everywhere isotropic.

- Lastly, where applicable, the director of the nematic phase is free to vary on the curved surface and will adapt to curvature via a vortex pattern.

The interaction between the nematic, constant-magnitude order parameter field and surface shape follows the same principles as the previous generic rep-

resentation. As in Section 3.4 and onwards, the pattern of vortices or defects is induced in an orientational order parameter field by the surface's Gaussian curvature. A rotation in the orientation of the order parameter minimizes energy in the presence of a nonzero spin connection, resulting in point defects in the global configuration of the field on the surface.

The vastly smaller energy scale of bending elasticity and the determination of shape and stability by interfacial mechanics only is specific to the material examined here, a hard-rod gas in which the only interactions are weak entropic effects.

6.4 Simulation method

With the analytic relationships from FMMT in hand, I adapt the previous lattice simulation to represent the specific material properties of an interfacial hard rod gas and with the additional constraint of conserving total particle. Since shape is fully determined by the 'external' mechanics described in Chapter 2, it is sufficient to explore field configurations on fixed surface shapes.

As before (Chapter 4), the surface of a modulated cylinder is representing by a periodic two-dimensional surface of dimensions $2\pi/k \times 2\pi$, divided into $N = \lfloor 50/k \rfloor \times 50$ lattice cells of dimensions $\ell_z \times \ell_\theta$.

Quantities sampled are a lattice of values $\eta(\mathbf{x}) \in (0, 1)$ representing area fraction, and a lattice of values $\vartheta(\vec{x}) \in [0, 2\pi)$ representing orientation of the vector (2-atic) unit director. While it will emerge in simulation that $\eta(\mathbf{x})$ takes near-uniform values, the implementation is general and allows for the initially hypothesized density variations. The angle ϑ is the angle of a unit complex order parameter $\hat{m} = e^{i\vartheta x} = \langle e^{i2\phi(x)} \rangle$. It relates to the double-headed vector in the tangent plane, $\hat{n} = \langle e^{i\phi(x)} \rangle$, in that a change of angle $\Delta\varpi$ in $\hat{n}$ corresponds to a change of $\Delta\vartheta = 2\Delta\varpi \pmod{2\pi}$ in $\hat{m}$. The complex 2-atic director $\hat{m}$ is compatible with the previously used expression for curvature coupling, Equation 3.4. Coefficients $K_\epsilon/2$ are the coefficients of squared gradients in $\hat{n}$; appropriate coefficients for squared gradients in $\hat{m}$, which reports twice the angular difference, are then $K_\epsilon/(2 \times 2^2)$.

The calculation of gradients takes a simple form analogous to that used in

previous sections only in the one-Frank-constant approximation. I employ the one-Frank-constant approximation and the analogous approximation for density gradients because the full isotropic form of Equation 6.18, when implemented, was found to be conceptually and computationally complex. Artifact-free calculation of isotropic gradient terms on a numerical grid required a symmetric eight-point stencil; furthermore on the curved surface curl must be calculated on a skew coordinate basis. Although initially implemented, the computational cost of an exact anisotropic representation was judged excessive given the overall small impact of elasticity on the system.

On initializing, the arrays are filled with uniform values of $\eta(z_i, \theta_j)$ and random values $\vartheta(z_i, \theta_j)$. Arrays of f_{id}, f_{ex}, $K(\eta)$, and $J(\eta)$ are calculated based on the initial values.

Steps in area fraction η and director θ are alternated sequentially. A measuring step now consists of 100 Monte Carlo steps of $N = \lfloor 50/k \rfloor \times 50$ random updates to director angle followed by 100 Monte Carlo steps in area fraction.

For a proposed change in a cell's director angle, a location is selected randomly and the value $\vartheta_{ij} = \vartheta(z_i, \theta_j)$ is updated by a step drawn from a Gaussian distribution with width σ_ϑ. The new value may be outside of the range $[0, 2\pi)$, as components $\hat{m}_z$ and $\hat{m}_\theta$ of the director are retrieved by taking real and imaginary parts of $\hat{m} = e^{i\vartheta}$. The new gradient energy is calculated according to

$$
\begin{aligned}
\Delta E^\eta = {}& E^{mgrad}(\eta^i, \hat{m}_{i,j}^p, \hat{m}_{i-1,j}^i, \hat{m}_{i,j-1}^i) \\
& - E^{mgrad}(\eta^i, \hat{m}_{i,j}^i, \hat{m}_{i-1,j}^i, \hat{m}_{i,j-1}^i) \\
& + E^{mgrad}(\eta_{i+1,j}^i, \hat{m}_{i+1,j}^i, \hat{m}_{i,j}^p, \hat{m}_{i+1,j-1}^i) \\
& - E^{mgrad}(\eta_{i+1,j}^i, \hat{m}_{i+1,j}^i, \hat{m}_{i,j}^i, \hat{m}_{i+1,j-1}^i) \\
& + E^{mgrad}(\eta_{i,j+1}^i, \hat{m}_{i,j+1}^i, \hat{m}_{i-1,j+1}^i, \hat{m}_{i,j}^p) \\
& - E^{mgrad}(\eta_{i,j+1}^i, \hat{m}_{i,j+1}^i, \hat{m}_{i-1,j+1}^i, \hat{m}_{i,j}^i)
\end{aligned}
\tag{6.71}
$$

with

$$
\begin{aligned}
\frac{E^{mgrad}}{\ell_z \ell_\theta} &= \frac{K(\eta)}{8} \left| \frac{\hat{m}_{i,j} - \hat{m}_{i-1,j}}{\ell_z} \right|^2 + \frac{K(\eta)}{8r(a,z)} \left(\left| \frac{\hat{m}_{i,j} - \hat{m}_{i,j-1}}{\ell_\theta} \right|^2 \right. \\
&\quad \left. + 2n\mathfrak{Im} \left[A_\theta \hat{m}^* \left(\frac{\hat{m}_{i,j} - \hat{m}_{i,j-1}}{\ell_\theta} \right) \right] + n^2 A_\theta^2 \right).
\end{aligned}
\tag{6.72}
$$

as in Chapter 4, but drawing on local density-dependent Frank constants $K(\eta)$. As before, numerical first derivatives are implemented using the simple two-point backwards difference, with first-order error compared to the true gradient at Ψ_{ij} but second-order error if interpreted as a representation of the gradient at interstitial locations. Because gradient is numerically implemented by taking the difference between the value and the value at a neighboring locations, the gradient energy at two neighboring sites is also affected by the proposed change and is included in equation 6.71. If the change is accepted, the new unit director angle is recorded modulo 2π. Director gradient at the three relevant locations is also updated in memory.

For a step in area fraction, two locations (z_{i_1}, θ_{j_1}) and (z_{i_2}, θ_{j_2}) are randomly selected. A change in number density at the first location is proposed based on a Gaussian distribution centered on η_{i_1,j_1} and with width σ_η. A corresponding change in area fraction $\Delta\eta_2 = -\frac{\sqrt{g_1}}{\sqrt{g_2}}\Delta\eta_1$ at the second location is also considered for a conserved total particle number. At each location, the energy difference resulting from a proposed density step is

$$
\begin{aligned}
\Delta E^\eta &= E^{loc}(\eta^p) - E^{loc}(\eta^i) \\
&\quad + E^{mgrad}(\eta^p, \hat{m}^i_{i,j}, \hat{m}^i_{i-1,j}, \hat{m}^i_{i,j-1}) - E^{mgrad}(\eta^i, \hat{m}^i_{i,j}, \hat{m}^i_{i-1,j}, \hat{m}^i_{i,j-1}) \\
&\quad + E^{\eta grad}(\eta^p_{i,j}, \eta^i_{i-1,j}, \eta^i_{i,j-1}) - E^{\eta grad}(\eta^i_{i,j}, \eta^i_{i-1,j}, \eta^i_{i,j-1}) \\
&\quad + E^{\eta grad}(\eta^i_{i+1,j}, \eta^p_{i,j}, \eta^i_{i+1,j-1}) - E^{\eta grad}(\eta^i_{i+1,j}, \eta^i_{i,j}, \eta^i_{i+1,j-1}) \\
&\quad + E^{\eta grad}(\eta^i_{i,j+1}, \eta^i_{i-1,j+1}, \eta^p_{i,j}) - E^{\eta grad}(\eta^i_{i,j+1}, \eta^i_{i-1,j+1}, \eta^i_{i,j})
\end{aligned}
\tag{6.73}
$$

with energy terms

$$
\frac{E^{loc}}{\ell_z \ell_\theta} = f_{id}(\eta) + f_{ex}(\eta)
\tag{6.74}
$$

as in Equations 6.2 and 6.16 and density gradient energy

$$\frac{E^{\eta grad}}{\ell_z \ell_\theta} = \frac{J(\eta)}{2} \left(\left| \frac{\eta_{i,j} - \eta_{i-1,j}}{\ell_z} \right|^2 + \left| \frac{\eta_{i,j} - \eta_{i,j-1}}{\ell_\theta} \right|^2 \right). \tag{6.75}$$

If the step is accepted, stored values of η, K, J at the two target locations as well as of $E^{\eta grad}$ at all six affected sites are updated.

Equation 6.13 gives an analytic function $\eta(\alpha^2)$; however it cannot be easily inverted to provide a similarly analytic map $\alpha^2(\eta)$. For a given value of η in simulation, where needed for f_{id}, f_{ex}, K, and J, the corresponding value α^2 is therefore retrieved from a lookup table which has been previously filled with pairs $(\alpha^2, \eta(\alpha^2))$ in increments of 0.001.

Again due to a simple scaling of energy by area, which does not consider rescaling of a field theory under the effect of thermal fluctuations, the simulation is strictly accurate only at $T \to 0$. In this theory the relationship $S(\eta)$ should differ from the function used when larger areas of the thermally fluctuating director are averaged over.

6.5 Configurations in simulation

For realistically small particle lengthscales, I observe nearly homogeneous density distributions in simulation. An exception is slightly lowered density at defect cores. Concurrently the 2-atic director field adapts to curvature via a pattern of rotations and defects. The principle is the same as that behind the patterns observed in Chapter 4. An example of the nematic field, represented by director angle ϑ, and number density field η on curved surfaces is shown in Figures 6.10 and 6.11. Areas where the field configurations conforms to expectations as seen in Chapter 4 are seen, i.e. ordered on flatter regions and with its phase rotating azimuthally, as well as excess defect pairs and defect lines which are a result of poor equilibration of this simulation.

The hard-rod material is 2-atic, so less strongly curvature-coupled than the hexatic. At most eight curvature-induced defects, four on the widest part of the cylinder and four on the narrow neck, are expected.

Without freedom in the magnitude of the order parameter, simulations do not converge on an equilibrium state well: there are many excess defect pairs in

addition to any curvature-induced defects. An annealing protocol (incrementally lowering simulation temperature) as well as sequences of director and density simulation did not improve the apparent lack of equilibration. The energy landscape of configurations in the simulation is apparently glassy. The result is that point defects, grain boundary lines, and coordinated defect-low density regions which formed by chance early in the simulation are not resolved to the expected more uniform field configuration. While observations from the Monte Carlo simulation do not formally correspond to non-equilibrium kinetics of the system, we can speculate that the experimental system is similarly susceptible to jamming in metastable non-equilibrium states characterized by excess defect pairs, boundary lines, and non-optimally-placed defects.

6.5.1 Larger particles

Choosing unrealistically large particle scale $D = 0.1$, particles comparable in length to the radius of the cylindrical channel, entropic effects are artificially tuned down. Such large particles are not compatible with basic assumptions of the model or with experimental observations. I nevertheless examine the larger particle size to artificially reduce the magnitude of entropy-related local energy terms. With the strong homogenizing effect lifted, we see curvature-induced density modulations (Figure 6.12). A high number density of particles is located on the widest part of the cylinder, which is in a relevant sense less curved. On the highly curved narrow neck, the material adopts the low-density isotropic phase, avoiding distortion of nematic order in this region. The high-density ordered regions show curvature-induced azimuthal rotation and additionally form several high-density grains of nematic order, with lower-density grain boundaries. The hypothesized system morphology of axial modulations in number density and order occurs in this hypothetical regime, but is overshadowed by other effects in more realistic description of a hard-rod fluid.

6.6 Discussion and conclusions

Inserting a description of an interfacial hard-rod fluid, I found that there are few spatial variations in density and order due to the high entropic cost of high-
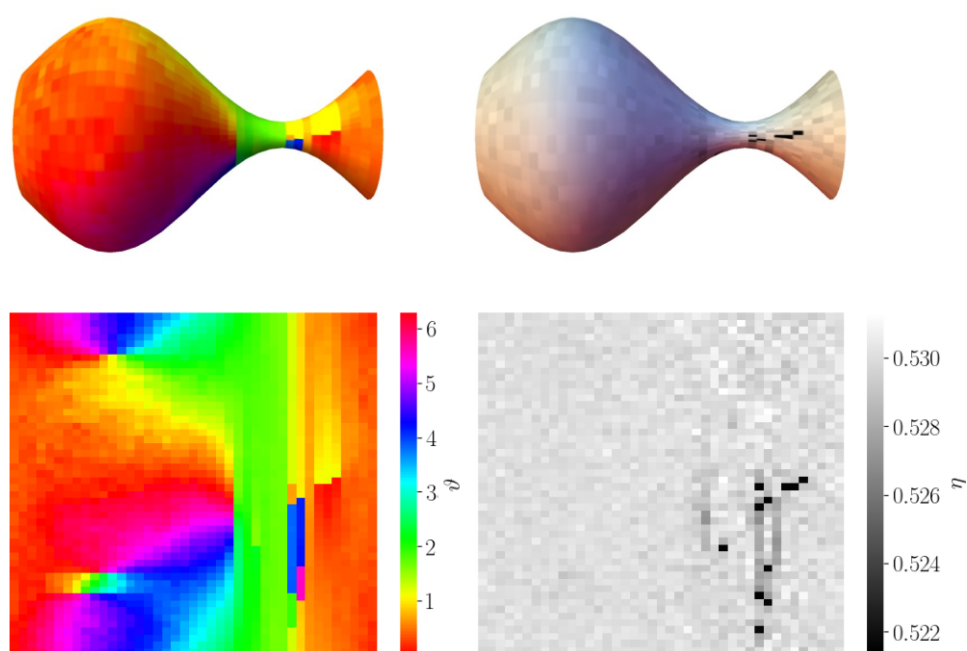
Figure 6.10: Configurations in simulation, with average area fraction fixed to $\eta = 0.53$, just above the isotropic-nematic transition at $\eta_{IN} = 0.525$. Director angle field ϑ (left) and area fraction field η (right), which are sampled simultaneously in simulation, are shown. The area fraction field is relatively uniform. A low number of rotations and defects is induced in the $n = 2$ order, in line with observations in Chapter 4. However, an excess defect pair and a displaced defect occur; the simulation has not reached equilibrium.
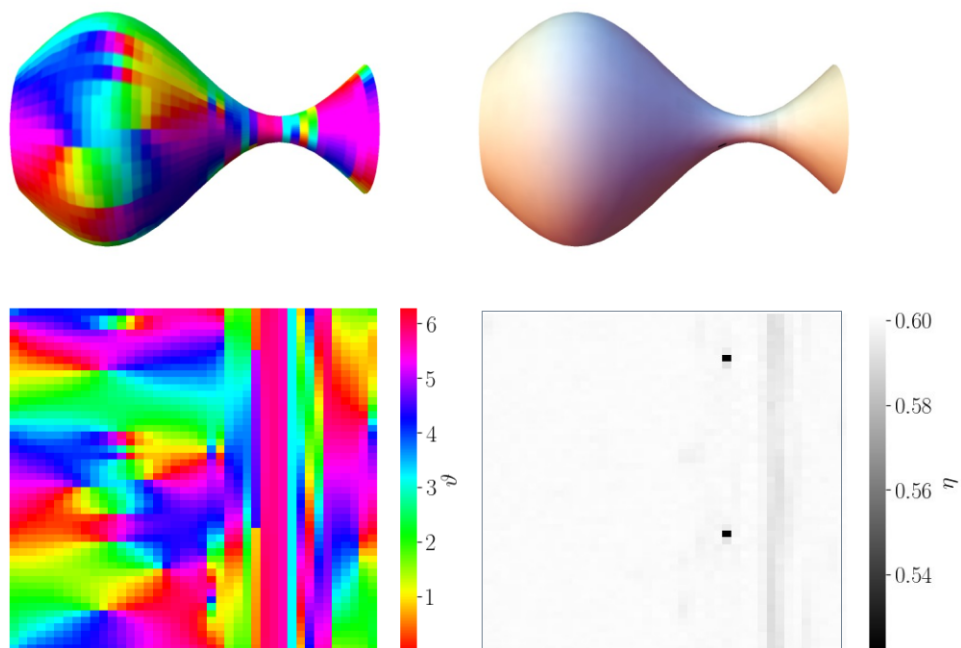
Figure 6.11: Configurations in simulation, average area fraction fixed to $\eta = 0.6$. Local area fraction field is strongly uniform (right). The angle of the director field (left) is characterized by many unresolved grain boundaries and defects.
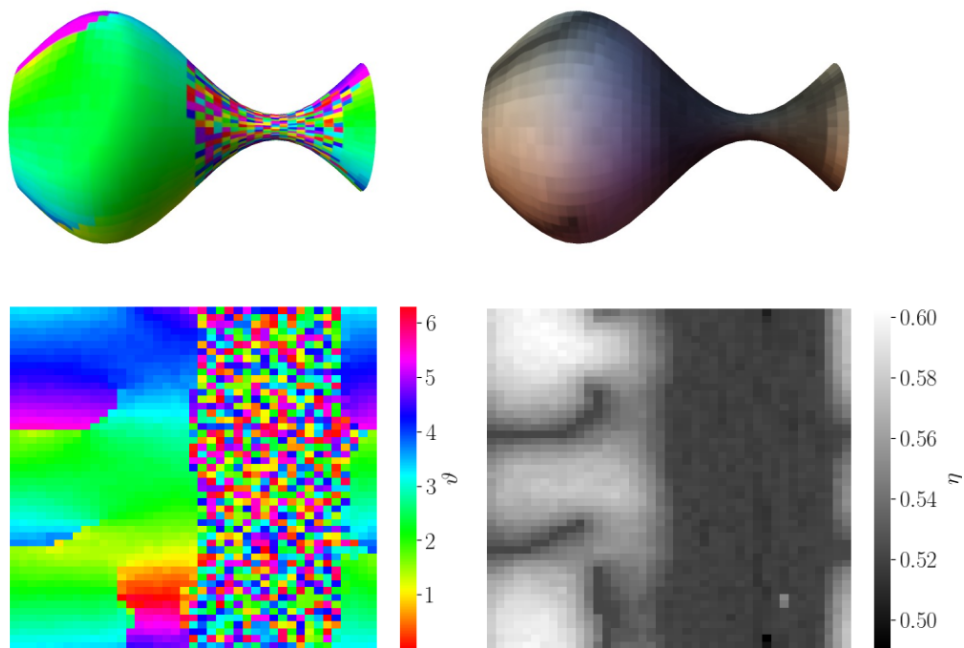
Figure 6.12: Configurations in simulation with the hypothetical large particle scale $D = 0.1$, incompatible with basic assumptions of the model, and average area fraction $\eta = 0.55$. In the regime of relatively low entropic energies, the initially hypothesized modulations in orientation (left) and area fraction (right) do occur. The region around the narrow neck is in the isotropic phase according to the low area fraction, so the director angle is meaningless and appears as random values. Order occurs on the widest part of the cylinder in high-density grains separated by low-density grain boundaries.

density regions. The curvature-induced splay in the nematic material has only negligible effects on system energy; there is no influence of order on either density distribution of surface shape. The relationship is one-sided: The direction of and patterns in orientational order adapt to surface shape.

The one-Frank-constant approximation and a parallel isotropic approximation of moduli J was made to significantly simplify numerical evaluation of spatial derivatives. The approximation retains the correct order of magnitude estimate for distortion free energies, which turns out to be small. However, it would be interesting to examine the effect of anisotropic Frank constants on the curved surface. Since $K_3 < K_1$, fundamentally the 'splay' type of curvature-induced distortions is preferred over bend and the particles should be biased towards axial alignment along the cylinder. A simulation of the anisotropic material could further reveal to what extent the field configuration around a defects breaks rotational symmetry, with an intermediate state between a symmetric vortex and completely parallel particle alignment expected.

The material parameters derived here are specific to discorectangles; they do not describe hexatically ordered hard-rod materials. The bending rigidity of a two-dimensioanl hexatic is equal to $72/\pi k_B T$ in theory and experiment [11], similarly negligible compared to homogenizing entropic contributions in a hard-disc fluid. As we have seen in Chapter 4, the stronger curvature-coupling of a hexatic material makes curvature-induced defects more likely.

In the model used here, the order parameter was assumed to strictly follow from area fraction according to Equation 6.13. The simulation could have been given an additional degree of freedom at this point, as deviations of order parameter S from that ideal value are probably less energetically prohibitive than the predicted density modulations.

The model is a hard-rod fluid with only excluded volume interactions: all effects, including derived quantities such as Frank constants, are purely entropy-based. Therefore, effects related to the entropy-based emergent bending rigidity are very weak in this hypothetical system. In contrast, in a realistic interfacial material, even using polymer-stabilized colloidal particles, there are a range of repulsive and attractive interactions at every scale, from capillary interaction to electrostatic repulsion. These interactions may increase the magnitude of Frank

constants significantly over that in the model used here and place distortion energies in the same order of magnitude as surface tension for some systems and interfacial materials. While not seen in the case represented here, orientational order in more strongly interacting nano- to microscale particles may still have an effect on emulsion morphology.

The model assumes relatively microscopic local particle size: if particle scale is similar to system scale and to variations in curvature (an external potential), a full computational minimization of the density functional theory on the object would be a more appropriate treatment. As in [12], it would reveal a pattern in individual rod locations on a confined and curved object.

Furthermore, an idealized two-dimensional material in a two-dimensional interface is assumed. Rod-like particles are assumed to have a discorectangular cross section embedded in the interface, excluding vertical or angled alignments. In experiments on rod-like particles as interfaces, horizontally oriented 'flippers' are routinely observed. Whether rare individual particles or larger domains are flipped depends on particle shape and interface type [13, 14] in unknown ways. Furthermore, such effects are sensitive to the exact particle shape - spherocylinder or ellipsoid [13] - possibly due to effects such as capillary attraction.

Larger particles, whose length is similar to the scale of surface curvature, in addition to being beyond the scope of the theoretical approach, can only partially be embedded in the surface due to its curvature. Explicit particle-based simulation of three-dimensional spherocylinders interacting with a curved model surface is a more appropriate approach for the study of larger particles, as carried out in several studies [15].

As with the previous model, orientational order is coupled to Gaussian curvature only. Additional mean curvature coupling, whether as a premise of a continuum field theory or emerging in a particle-based three-dimensional simulation, could be studied in interaction with the existing Gaussian curvature effects.

Bibliography

[1] Y. Rosenfeld, Phys Rev Lett **63**, 980 (1989).

[2] R. Roth, J Phys Condens Matter **22**, 063102 (2010).

[3] R. Wittmann, M. Marechal, and K. Mecke, EPL **109**, 26003 (2015).

[4] R. Wittmann, C. E. Sitta, F. Smallenburg, and H. Löwen, J Chem Phys **147**, 134908 (2017).

[5] R. Wittmann, M. Marechal, and K. Mecke, Phys Rev E **91**, 052501 (2015).

[6] Y. Rosenfeld, Phys Rev A **42**, 5978 (1990).

[7] R. Roth, K. Mecke, and M. Oettel, J Chem Phys **136**, 081101 (2012).

[8] H. Hansen-Goos and K. Mecke, Phys Rev Lett **102**, 018302 (2009).

[9] A. Poniewierski and J. Stecki, Mol Phys **38**, 1931 (1979).

[10] R. Wittmann, *Density functional theory for liquid Crystals: Refining fundamental measure theory for anisotropic bodies* (FAU University Press, 2015).

[11] P. Keim, G. Maret, and H. H. von Grünberg, Phys Rev E **75**, 031402 (2007), 0610332.

[12] R. Wittmann, L. B. Cortes, H. Löwen, and D. G. Aarts, Nat Commun **12**, 1 (2021).

[13] T. Li, G. Brandani, D. Marenduzzo, and P. Clegg, Phys Rev Lett **119**, 018001 (2017).

[14] K. A. Macmillan and P. S. Clegg, J Phys Chem Lett **12**, 5241 (2021).

[15] F. Smallenburg and H. Löwen, J Chem Phys **144**, 164903 (2016).

CHAPTER 7

Conclusions

Abstract

I review findings, methods, and limitations of the work presented in this thesis. In this thesis I utilized a range of analytical and computational methods for assessing the affect of orientational order on modulated cylindrical channels and retrieve general principles. I found a need to modify the existing theoretical model to describe particle-stabilized interfaces. The core research question of whether orientational order affects emulsion morphology in solid-stabilized emulsions is answered in the negative for the specific interfacial material modeled in Chapter 6. I speculate on future experimental and further theoretical explorations or orientational order in solid-stabilized emulsions.

7.1 Results

This thesis explores orientational order in interfacial monolayers of nano- or microparticles in solid-stabilized emulsions, in particular in view of shape and stability of non-spherical droplets and connections in emulsions. To this end, core research questions include: How does interface shape affect orientational order? How does orientational order affect shape and stability of elongated emulsion droplets and related fluid-fluid structures? Can principles from continuum field theory and from models of molecular surfactant phases be applied to solid-stabilized emulsions? Which outcomes and principles are general across systems?

To this end, a variety of approaches are developed. The common Landau-Ginzburg theory of orientational order [1] is first adapted to cylinder-like surface geometry in Chapters 2 to 4. In Chapters 2 and 3 I apply and examine a wide range of analytic methods to probe aspects of system behavior on the novel surface shape, including linear stability analysis, numerics, Fourier space field theory, and local solutions. In Chapter 4 I develop and examine a stochastic simulation protocol which, while incomplete regarding a full representation of high-temperature fluctuations, gives good qualitative results at low computational cost. Methods developed in Chapters 2 to 4 were largely found to be transferable to the altered description of orientational order adopted in Chapter 6. In Chapter 5 I replicate and extend two experiments [2, 3] and discuss the experimental literature in order to identify crucial aspects and omissions in the model as applied to solid-stabilized systems. Finally, the generic Landau-Ginzburg model and the surface tension model appropriate to conventional emulsions is replaced with a more specific model of a hard-rod interfacial material, which was developed further from the theoretical literature [4] for this purpose, in Chapter 6.

On the modulated cylindrical surface shape, I find patterns of emergent defects, whose number and placement follows known principles from theoretical laws at the defect level. While the periodic cylindrical surface is topologically compatible with a defect-free configuration of orientational order, I observe that increasingly curved surface shapes are associated with a discrete spectrum of $m = 0, 1, 2, ...n$ order parameter configurations bearing $4m$ excess defects

169

in charge-neutral pairs. I suggest that an analogous discrete spectrum of additional exotic droplet shapes with additional defect pairs occurs in spherical systems. For the initially suggested regime of parameters, $c \approx |\alpha|$, I also observe a curvature-induced modulation in the magnitude of order, with a banded pattern of alternatingly isotropic and orientationally ordered regions on the modulated cylindrical shape. The phenomenon is reminiscent of curvature-induced phase separation in other materials. However, the later model suggests that the phenomenon, while theoretically present, will be negligible in the regime of the weaker order-curvature coupling.

In Chapter 6, generality of the initial findings is tested by applying the framework to a different system, that of a hard-rod fluid. The specific material model replacing the generic theory provided estimates of the relative order of magnitude of unknown parameters in the theory, revealing certain effects as dominant, but did not reveal fundamentally different phenomena. Unsurprisingly, topological and geometrical principles provide robust predictions on outcomes across a range of physically distinct systems. Additional phenomena are predicted due to the anisotropic material properties of the hard rod gas, but could not be fully explored in simulation. By contrast with Chapter 6, the theory explored in Chapters 3-4 also turned out to be particularly conducive to stochastic simulation. However, the difficulty reaching equilibrium in the latter Monte Carlo simulation hints at similar phenomena in jammed experimental systems.

The final theoretical result is that while orientational order exists in interfacial monolayers of nano- or microparticles in solid-stabilized emulsion systems and while it does interact with surface curvature by adopting defect-bearing configurations, the effect of orienational order on droplet shape and stability is negligible in the hard-rod model considered here. Other effects, such as surface tension, spontaneous curvature, and particle jamming are the main determinants of emulsion morphology and stability in the solid-stabilized systems observed here. The potentially complex two-way relationship between order and curvature is resolved into a one-way relationship when transferring the model to the larger-scale systems that are the subject of this thesis.

7.2   Relevance to the Broader Literature

Building on literature related to Plateau-Rayleigh instabilities and pearled lipid vesicles, I first explore the limitations of perturbative stability analysis and suggest how analysis of orientational order can be incorporated into an energetic stability analysis.

Compared to other theoretical work on orientational order on curved or even cylindrical interfaces [5], I take advantage of computational methods to lift common simplifying assumptions, namely the restriction of the orientational order parameter to a constant magnitude, and investigate the models in a more general regime. The additional degrees of freedom were indeed found to have negligible effects; this work provides evidence that the ubiquitous simplifying assumptions are justified. In this work I demonstrate several complementary analytic methods and suggest a low-cost simulation scheme on curved surfaces as a useful and accessible complement to theoretical investigations into orientational order as a field theory.

A question arising from the approaches used over the course of this study is whether a statistical physics approaches is appropriate for bijels, which are said to be jammed. During the formation of bijels the particles jam; this is believed to be the main effect arresting coarsening [6, 7]. In particular, successful bijel formation depends on the timescale of forming densely occupied interfaces being shorter than the timescale of fluid-dynamic evolution to the true equilibrium, which would be a droplet phase [6]. However, Bai *et al.* have found that rheological evidence suggests that particles rearrange within the interface over longer timescales [7], apparently towards a less compressible (likely denser) packing. The first stage, bijel or emulsion formation, where complex (hydro-)dynamic instabilities are crucial, is beyond the scope of this project. The statistical physics of particles on a constrained set of interface shapes is suited to describe the later evolution of the substance, during aging. In general, jammed states are not amenable to statistical physics treatment. While technically evolving ergodically in the limit of infinite time, a statistical sampling is not seen on experimental timescales. However, in bijels, we can separate the behavior on different time- and length scales. Certain aspects of the system - the structure of fluids and interfaces - are jammed, while within the particle layer, Bai et al. suggest local

rearrangements take place. The system is approximated by fields - representing the particle layer - sampled statistically at equilibrium, while the overall surface shape is heuristically constrained to a shape or small family of shapes.

While experimentatal literature on rod-stabilized emulsions [8] and bijels [9] motivated the examination of a hard-rod material in Chapter 6, a model is drawn from the theoretical literature [4, 10, 11]. Building on the literature, I derive additional material parameters in the FMMT model of hard discorectangular fluids in two dimensions for cases not yet explicitly covered in the literature and incorporate the results into my existing model of the cylindrical interface system. The additional material parameters derived for hard rods in two dimensions may be of interest in modeling nematic colloidal materials in a variety of other contexts.

7.3   Outlook

As with most soft matter problems, in emulsions and bijels there is a hierarchy of structures across multiple length- and time scales, from the interactions between individual interfacial particles or molecules to the arrangement of droplets and channels. I here focus on the mesoscale phenomenon of the stability and morphology of individual droplets or channels. Interactions between molecules or particles at smaller scales are included as interfacial mechanical properties and as a continuum field theory properties, a relatively familiar procedure in physics. On the other hand many assumptions about the larger structure, the existence of a channel, is assumed to be fixed as metastable or evolving on a slower timescale. While it is suggested that the stability of channels is a key indicator of bijel stability [6], future experimental and theoretical studies could explore to what extent different local structures in a complex emulsion can in fact be viewed as isolated systems. For example, by fluorescently labelling nanoparticles, exchange of material between different droplet regions over time could be quantified, as in [12]. The theoretical framework suggests that defects in idealized materials remain localized to the associated Gaussian curvature, however more consideration is required in potentially jammed systems.

For the specific interfacial material modelled here in Chapter 6, the ques-

tion of whether surface shape adapts to accommodate orientational order or vice versa was unambiguously resolved, with orientational order adapting to droplet shape. In this system the effects of curvature-coupled orientational order were too weak to have any impact on droplet shape. On the other hand, in the case of surfactant-stabilized systems, order-driven droplet shapes have been experimentally observed [13]. It would be interesting to develop a model experimental system where order in a solid-stabilized emulsion impacts droplet shape, in contrast to the prediction in Chapter 6. While the theory derived from first principles was limited to a gas-like system, colloidal particles with strong attractive interactions can be investigated in experiments. Such an interfacial material may have bending moduli exceeding the $72/\pi k_B T$ range in a hard-sphere fluid by several orders of magnitude. However, aggregation between strongly attractive colloids is a challenge, preventing the formation of ordered interfacial monolayers. Tunable systems, where interparticle attractions are changed by factors such as temperature, pH, or magnetic fields, may be an avenue to observing an ordered interfacial layer with significant effects on emulsion morphology.

Due to difficulties with both Fourier transform and lattice representations of the curved surface, statistical analysis is limited to retrieving the low-temperature ground state of the system. With a different simulation scheme, information on the full statistical ensemble of the system, for example relative probabilities of vortex states with defects, could be retrieved in simulations.

An initial motivation for research into particle behavior in solid-stabilized emulsions was that an understanding of the effects of particle properties (shape, size, wetting properties) on emulsion stability can inform the formulation of emulsion products. Furthermore, the ability of solid-stabilized emulsions to attain morphologies with non-spherical droplets opens up avenues in engineering unique functional soft materials, for example taking advantage of polyhedral droplet shapes or of regularly placed defects. In surfactant-stabilized emulsion systems facetted droplets that could be the basis of nanoengineered materials have already been experimentally tested [13]. An understanding of the same phenomenon in solid-stabilized systems may similarly open up opportunities in novel material design. As evidenced by the existence of the bijels, jammed interfacial nanoparticle layers make additional macroscopically complex shapes

possible. However, it is not straightforward to transfer existing theoretical methods from surfactant-stabilized to particle-stabilized emulsions, precisely because of the unique additional properties of irreversible adsorption and jamming. This thesis represents a start into exploring the role of orientational order, in conjunction with other effects, in the rich but complex theory of solid-stabilized emulsion system. Its methods and outcomes enable estimates about which effects are dominant on a case-by-case basis.

Bibliography

[1] J.-M. Park, T. C. Lubensky, and F. C. MacKintosh, EPL **20**, 279 (1992), 9606105.

[2] T. Einert, P. Lipowsky, J. Schilling, M. J. Bowick, and A. R. Bausch, Langmuir **21**, 12076 (2005).

[3] T. Li, J. Klebes, J. Dobnikar, and P. S. Clegg, Chem Comm **55**, 5575 (2019).

[4] R. Wittmann, C. E. Sitta, F. Smallenburg, and H. Löwen, J Chem Phys **147**, 134908 (2017).

[5] P. Lenz and D. R. Nelson, Phys Rev E **67**, 19 (2003).

[6] K. Stratford, R. Adhikari, I. Pagonabarraga, J.-C. Desplat, and M. E. Cates, Science **309**, 2198 (2005).

[7] L. Bai, J. W. Fruehwirth, X. Cheng, and C. W. Macosko, Soft Matter **11**, 5282 (2015).

[8] T. Li, G. Brandani, D. Marenduzzo, and P. Clegg, Phys Rev Lett **119**, 018001 (2017).

[9] N. Hijnen, D. Cai, and P. S. Clegg, Soft Matter **11**, 4351 (2015).

[10] A. Poniewierski and J. Stecki, Mol Phys **38**, 1931 (1979).

[11] R. Wittmann, M. Marechal, and K. Mecke, Phys Rev E **91**, 052501 (2015).

[12] D. J. French *et al.*, Sci Rep **6**, 1 (2016).

[13] O. Marin, M. Tkachev, E. Sloutskin, and M. Deutsch, Curr Opin Colloid Interface Sci (2020).